DESIGN AND DEVELOPMENT OF NITINOL DEVICE FOR ACTUATION AND BIOMEDICAL APPLICATIONS

Seyedeh Farzaneh Hoseini

Supervisor: Prof. Andrea Spaggiari

Submitted in fulfilment of the requirements for the degree of

Doctorate School in Industrial Innovation Engineering

Curriculum: Mechatronics and Energetic Engineering

Ph.D. cycle XXXVII

Doctorate Coordinator: Prof. Franco Zambonelli

Department of Engineering Sciences and Methods
University of Modena and Reggio Emilia
December 2024

UNIONE EUROPEA
Fondo Sociale Europeo
Ministero dell'Università
e della Ricerca
PON
RICERCA
E INNOVAZIONE
2014 - 2020
REACT EU

Tesi di dottorato di ricerca co-finanziata nell'ambito del Programma Operativo Nazionale Ricerca e Innovazione 2014-2020 (CCI 2014IT16M2OP005), risorse FSE REACT-EU, Azione IV.4 “Dottorati e contratti di ricerca su tematiche dell’innovazione” e Azione IV.5 “Dottorati su tematiche Green”.

Keywords

Additive Manufacturing
FEM
Nitinol
SMA actuator
Stent

PS: For clarity, the terms are listed alphabetically.

Abstract

Nitinol (NiTi) is a type of smart material renowned for its unique characteristics, such as the shape memory effect (SME) and superelasticity (SE). This thesis investigates the applications of NiTi in both engineering and biomedical fields, focusing specifically on innovative actuators and the development and optimization of self-expanding stents. In the engineering domain, a novel Shape Memory Alloy (SMA)-metamaterial actuator is proposed, capable of exhibiting reversible, multi-directional elongation induced by the unidirectional contraction of a single SMA component upon heating. A theoretical model to predict the actuation stroke based on the material properties and geometry was developed and validated, demonstrating the potential of SMA-metamaterial actuators for applications requiring multi-axial motion. In the biomedical field, the work examines the evolution of self-expanding stents, with a focus on optimizing NiTi braided stents, laser-cut stents, and additive manufacturing (AM)-based stents. The design and optimization of an SX NiTi braided stent were explored using analytical and numerical models, along with Multi-Objective Particle Swarm Optimization (MOPSO), improving key parameters such as radial force, stiffness, and deployment precision. The thesis also investigates the superelastic behavior of the laser-cut SX NiTi Scitech-Solaris stent through finite element modelling and experimental validation. Furthermore, the potential of AM for producing patient-specific stents with complex geometries is discussed, emphasizing the advantages and challenges associated with surface quality and porosity control. Overall, this work contributes to advancing the understanding and practical application of NiTi in both engineering and biomedical domains, offering new insights into actuator design, stent optimization, and its advanced manufacturing techniques.

Dedication

This thesis is dedicated to the love of my life, Reza, who has always been my source of comfort through all difficulties, and to my dear baby girl, Rira, on the way, who has patiently endured my sleepless nights with understanding.

To my mom, Golnar, who has always stood by me through the storms of life.

To my two lovely and beautiful sisters, Fatemeh and Maryam, whose love and support, even from a distance, have inspired me to keep going.

Acknowledgements

First and foremost, I would like to extend my sincere gratitude to my supervisor and mentor, Prof. Andrea Spaggiari, who has supported me at every step of my research with his knowledge and understood me during the most difficult obstacles that I have faced on this journey. I am honored to have pursued my Ph.D. studies under his supervision.

I would also like to thank my colleagues and friends, especially Dr. Luke Mizzi, whose contributions were crucial to the development and evolution of this project.

I am deeply grateful to my loving family: my wonderful parents, amazing brother, and kind sisters, whose unconditional love and support have inspired me to keep moving forward. I am also proud and grateful to have a wonderful husband, Reza, who has always encouraged me to reach my goals and taught me that, above all, health, peace, and enjoying the journey—no matter how difficult it can get—are the most important things in life.

Last but not least, I'd also like to thank myself for pursuing my dreams and never giving up, even when there seemed to be no end in the dark tunnel.

Statement of Original Authorship

The work contained in this thesis has not been previously submitted to meet requirements for an award at this or any other higher education institution. To the best of my knowledge and belief, the thesis contains no material previously published or written by another person except where due reference is made.

Signature: Farzaneh. Hoseini

Date: 31/12/2024

Table of Contents

List of Figures

List of Tables

List of Abbreviations

AM	Additive Manufacturing
BDS	Biodegradable Stent
BMS	Bare Metal Stent
BRS	Bioresorbable Stent
BX	Balloon-Expandable
COF	Chronic Outward Force
CR	Crush Resistance
DES	Drug-Eluting Stent
EB-PBF	Electron Beam Powder Bed Fusion
FDM	Fused-Deposition Method
FE	Finite Element
FEA	Finite Element Analysis
FEM	Finite Element Method
FPA	Femora-Popliteal district Arteries
ISR	In-Stent Restenosis
LB-PBF	Laser-Based Powder Bed Fusion
OS	Oversizing
PAD	Peripheral Artery Disease
PTA	Percutaneous Transluminal Angioplasty
PVI	Percutaneous Vascular Intervention
RRF	Radial Resistive Force
SFA	Superficial Femoral Artery
SE	Superelasticity
SMAs	Shape Memory Alloys
SME	Shape Memory Effect
ST	Stent Thrombosis
SX	Self-Expanding
WSS	Wall Shear Stress

Aim of Thesis

The aim of this thesis is to explore the application of Nitinol (Nitti) in both engineering and medical fields, specifically focusing on actuators and biomedical devices like stents, through a comprehensive approach that combines theoretical modelling optimization, experimental validation, and advanced manufacturing techniques.

1.1.1 Application of NiTi in engineering: actuators

The aim of this phase is to design, develop, and validate a novel shape memory alloy (SMA)-metamaterial actuator capable of multi-directional elongation driven by unidirectional contraction upon heating.

To achieve this aim, the following steps were undertaken:

- Creating a theoretical model to predict the actuation stroke based on material properties and the metamaterial geometry, providing insights for future optimization.
- Designing the actuator with three core components: an SMA element for activation, a bias component for reversibility, and a metamaterial geometry for amplifying and redirecting actuation forces globally.
- Testing the actuator's functionality involved conducting multiple activation and deactivation cycles under various configurations to evaluate its performance and reusability.
- Validating the actuator's performance confirmed the alignment of the theoretical model predictions with the observed actuation behavior.

1.1.2 Application of NiTi in medical devices: stents

The second phase explores the design, optimization, and manufacturing of Nitti-based stents for biomedical applications, with a focus on achieving high performance, and customization and classifying stents based on quantitative figures of merit. The objectives are:

- classify stents based on quantitative figures of merit, providing a valuable tool to assist designers in selecting the most appropriate stent for specific applications.
- Investigating the evolution of stent designs and classifying manufacturing techniques, including braided, laser-cut, and additively manufactured stents

Braided stents:

- Designing a SX NiTi braided stent
- Analyzing the stent behavior using analytical and numerical models.
- Enhancing the performance of the stent in terms of increasing radial stiffness, radial force, and deployment precision (reducing foreshortening) by applying Multi-Objective Particle Swarm Optimization (MOPSO)

Laser-cut stents:

- Using the SX NiTi Scitech-Solaris stent as a case study to demonstrate design and superelastic behavior.
- Identifying and validating the material model that best represents the unique properties of the NiTi alloy used in the Scitech-Solaris stent.
- Simulating Crush-Resistance (CR) tests with high accuracy through a combined experimental and FEM approach.

Additive Manufacturing (AM) of Stents:

- Introducing Additive Manufacturing (AM), specifically laser-based powder bed fusion (LB-PBF), as a transformative technique for fabricating NiTi stents with intricate, patient-specific geometries.
- Highlighting the advantages of AM, such as design flexibility and waste minimization, alongside its challenges, including surface quality, porosity control, and process complexity.
- Providing insights into variability among printing machines and proposing some stent designs tailored to meet the specific requirements and limitations of these machines.

Thesis outline

This thesis is organized into six chapters, each addressing a specific aspect of the application of Nitinol (NiTi) in engineering and medical fields, with a particular focus on actuators and biomedical devices like stents. The chapters are structured to build a cohesive narrative, beginning with an introduction to NiTi and progressing through design, optimization, and advanced manufacturing techniques. The content of each chapter is summarized as follows:

Chapter 1: This chapter provides an overview of NiTi's unique properties, including the shape memory effect (SME) and superelasticity (SE). It discusses the state of the art in NiTi applications, focusing on its use as an actuator and in biomedical devices such as stents.

Chapter 2: This chapter focuses on the design, development, and validation of a novel SMA-metamaterial actuator. It includes theoretical modelling, design process, and experimental testing of the actuator. The chapter discusses the actuator's components, functionality, and potential applications, supported by experimental results and implications for future optimization.

Chapter 3: This chapter explores the design, optimization, and manufacturing of NiTi stents. It is divided into three main sections:

- Braided Stents: Design and optimization of a self-expanding (SX) NiTi braided stent using analytical and numerical models, supported by Multi-Objective Particle Swarm Optimization (MOPSO).
- Laser-Cut Stents: A case study on the SX NiTi Scitech-Solaris stent, focusing on dimensional measurements, material modelling, and Crush-Resistance (CR) simulations validated against experimental data.
- Additive Manufacturing (AM) of Stents: An introduction to AM techniques, highlighting their advantages, challenges, and design considerations for stent fabrication. This section also addresses the variability among AM machines and proposes stent designs tailored to specific machine requirements.

Chapter 4: This chapter summarizes the key findings of the research, emphasizing the contributions to the fields of engineering and biomedical applications. It also discusses the implications of the findings and suggests potential directions for future work.

Chapter 5: This chapter includes a comprehensive list of all references cited throughout the thesis, providing a solid foundation for the research conducted.

Chapter 1: Introduction

This chapter outlines the state of the art on Nitinol (NiTi) (section 1.1), providing a comprehensive overview of its discovery, underlying mechanisms, and distinctive characteristics, such as the shape memory effect (SME) and superelasticity (SE). The microstructural and mechanical behavior of NiTi are explored, emphasizing its phase transformations and the factors influencing its unique functionality.

1.1 STATE OF THE ART ON NITINOL

In the early 1960s, a fascinating discovery was made by metallurgist William Buehler and his colleagues at the U.S. Naval Ordnance Laboratory (NOL). They were investigating an equiatomic alloy made of nickel and titanium (NiTi). During their investigations, Buehler and physicist Frederick Wang made an extraordinary discovery: They observed that when the alloy was formed at high temperatures and subsequently cooled, it could undergo deformation while retaining its ability to recover its original shape. The remarkable part occurred upon reheating the material, as it "remembered" its initial configuration and reverted to its original form[1]. This phenomenon, later termed the shape memory effect (SME), marked a significant breakthrough in materials science. This discovery was significant at the time, and to this day, NiTi alloys are frequently referred to as Nitinol (NiTi). Among the many types of shape memory alloys (SMAs) that can recall and return to their original shape when subjected to thermal or mechanical stress, NiTi is by far the most popular and extensively employed because of its superior properties.

In light of NiTi's groundbreaking discovery and its extraordinary properties, it is essential to understand the underlying structural characteristics that contribute to its desired functional and mechanical attributes. The unique behavior of this alloy is closely linked to its phase diagram, which illustrates the relationship between temperature and composition as shown in Figure 1 . The diagram reveals how variations in the alloy's composition can lead to the development of secondary phases, which significantly impact its functional and mechanical attributes[2]. The highlighted central region of the diagram indicates the NiTi intermetallic compound, where optimal properties are achieved. Careful control over the alloy's composition during manufacturing is crucial to ensure that the desired characteristics are maintained for various applications, including medical devices and actuators.

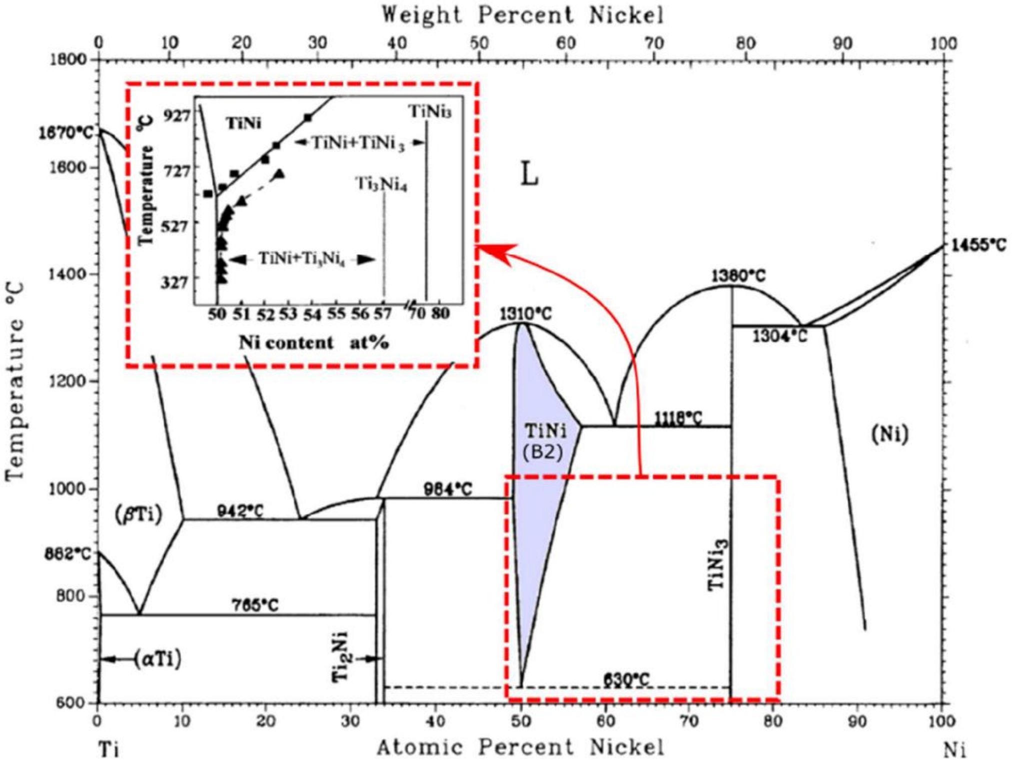

Figure 1. Binary phase diagram of NiTi alloys [3].

From a microstructural point of view, NiTi has two main solid phases with distinct features and characteristics; the austenitic phase, also called the parent phase, a simple cubic B2 structure (Figure 2(a)), which is stable under low stress and high temperature, and the martensitic phase, also called daughter phase, a monoclinic B19’ structure (Figure 2(b)), which is stable under high stress and low temperature [4].

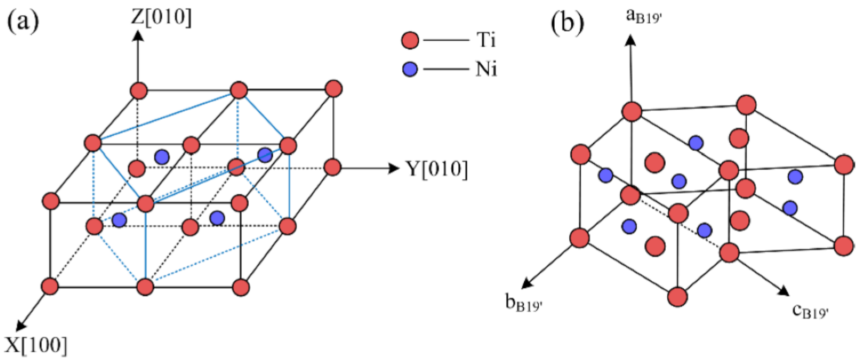

Figure 2. Crystal structures of nickel–titanium shape-memory alloy (NiTi SMA): (a) B2 cubic (austenite); (b) B19′ monoclinic (martensite) [5].

During cooling, the austenite gradually transforms into martensite at specific temperatures known as M_s (the start of martensite formation) and M_f (the finish of martensite formation). Conversely, when heated, martensite reverts to austenite at A_s (the start of austenite formation) and A_f (the finish of austenite formation). This transformation is characterized by thermal hysteresis, meaning that the transformation temperatures differ for heating and cooling cycles.

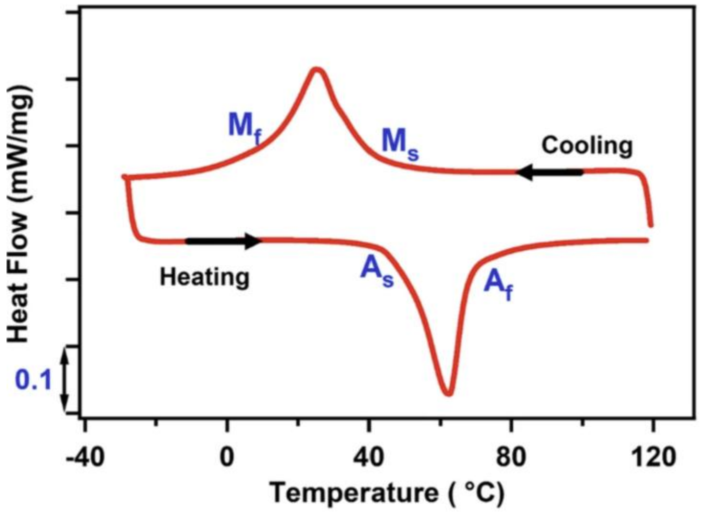

Figure 3. typical DSC curve of an equiatomic NiTi alloy [6].

Mechanical deformation is indeed another mechanism that can trigger the martensitic phase transformation in NiTi alloys. This transformation occurs when the material is subjected to external stress, leading to changes in its microstructure.

In addition, the martensitic phase is divided into two forms: twinned and detwinned. Detwinned martensite is a state in which the martensite crystals have undergone a process that removes the twin boundaries, resulting in a more stable microstructure. Twinned martensite, on the other hand, has twin boundaries making the material less stable. The detwinned martensite is stable at high-stress state regardless of temperature, while twinned martensite is stable at both low-stress and low temperatures[7]. The solid-state transformation from austenite to martensite occurs almost instantly by rapid cooling or by inducing stress (Figure 4).

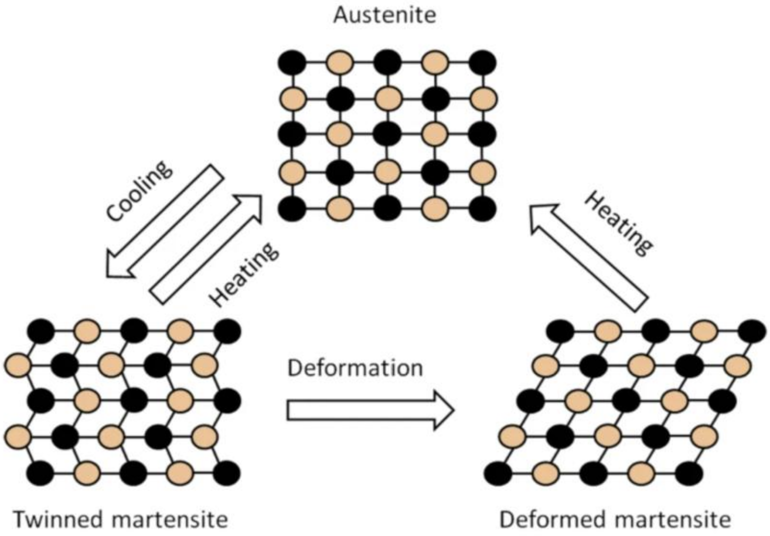

Figure 4. Martensite-austenite phase transition [8].

NiTi also exhibits remarkable properties such as shape memory effect (SME) and superelasticity (SE) attributed to its peculiar crystal structure and phase transformation between austenite and martensite [9]. To better clarify the underlying mechanisms, additional information will be provided in the next two sections.

1.1.1 Shape memory effect (SME)

Figure 6 demonstrates the stress-strain-temperature curve of a NiTi alloy, which represents the SME and SE. Starting at point A on the curve, when the alloy is stored at temperatures above the austenite finish temperature (A_f), it predominantly exists in the austenitic phase. Upon cooling to lower temperatures (point B), the alloy transforms into twinned martensite. When external stress is applied to this martensitic structure, it leads to reorientation and detwinning of the martensite variants, resulting in a macroscopic shape change. This detwinning process is characterized by a stress plateau in the stress-strain curve (point C), where one martensite variant grows preferentially in a specific direction at the expense of eliminating other variants. After unloading, this new configuration is retained (point D). However, when the material is heated back to temperatures above A_f (point E), a reverse phase transformation occurs, transitioning from detwinned martensite back to austenite, allowing the material to recover its original shape (returning to point A). This remarkable behavior exemplifies the SME and enables various applications, including orthodontic wires and actuators [10–13].

SME can be categorized into three main types: one-way shape memory effect, two-way shape memory effect, and full-course shape memory effect, which is demonstrated in Figure 5.

One-way SME

This phenomenon occurs when the alloy deforms at lower temperatures and can recover its original shape only during the heating process. Upon heating, the material transitions from the martensitic phase to the austenitic phase, restoring its predefined shape.

Two-way SME

In this case, some alloys can remember and recover both the high-temperature phase when heated and the low-temperature phase when cooled. This means that the material can return to a specific shape at both ends of the temperature spectrum.

Full-Course SME

This advanced form of shape memory effect allows the material to restore its high-temperature phase shape upon heating while simultaneously changing the low-temperature phase into a different shape with an opposite orientation when cooled.

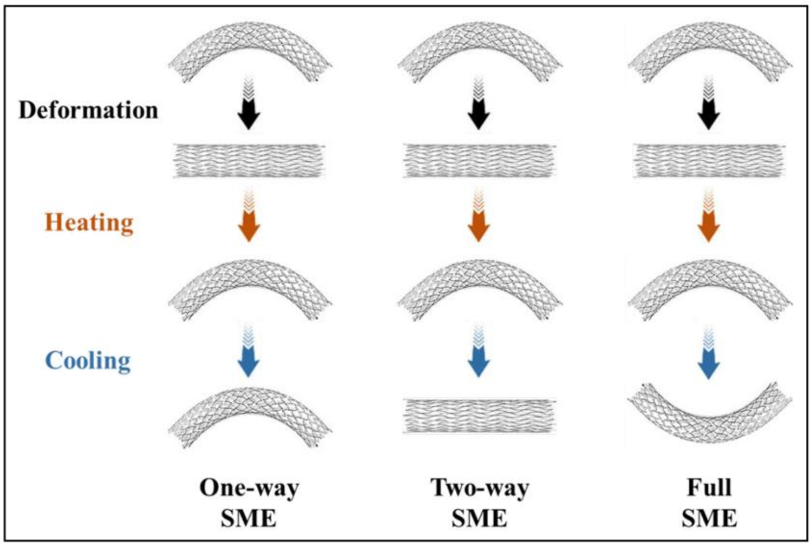

Figure 5. Schematic diagram showing the distinct types of SME in NiTi: One-Way, Two-Way, and Full-Course [14].

1.1.2 Superelasticity (SE)

Through superelasticity (SE), a significant portion of strain can be recovered simply by unloading the deformed part of a NiTi alloy in its austenitic phase [15–19]. This remarkable phenomenon arises from the stress-induced martensitic (SIM) transformation that occurs during the loading of the austenitic phase. When a sufficiently large mechanical stress is applied to the NiTi in its austenite phase, as shown in point A in Figure 6, it undergoes a phase transformation to the detwinned martensite phase. In this phase, NiTi can tolerate much higher levels of strain than other materials without experiencing permanent deformation. When the stress is released, point X in Figure 6, NiTi spontaneously reverts to its original austenite phase and shape. This ability to undergo large recoverable deformations is what grants NiTi its SE. Unlike typical metal alloys that have recoverable deformability below 1%, elastic recovery of NiTi can reach up to 8% strain [20–22]. It is important to note that the superelastic mechanical properties of NiTi are only evident within the temperature range between the austenite finish and detwinned martensite deformation temperatures ($A_f < T < M_d$) [23]. The remarkable elasticity of superelastic NiTi is particularly advantageous for biomedical devices, such as stents.

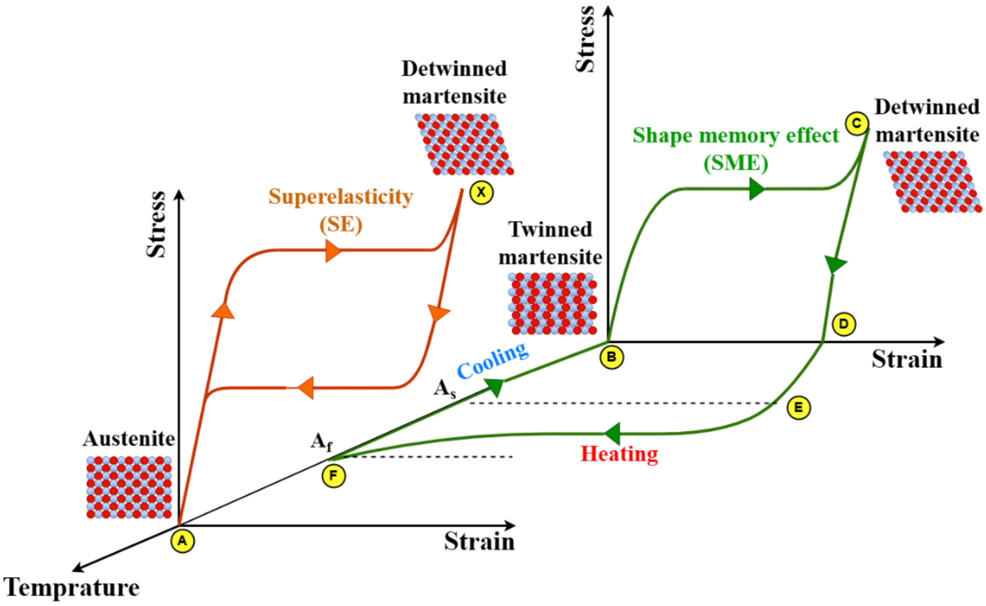

Figure 6. Shape memory effect and SE of NiTi, adapted from [9].

1.1.3 Biomedical applications of NiTi

NiTi has revolutionized the field of biomedical devices due to its exceptional properties, such as SE, which allow it to mimic bone-like behavior in implants. Its distinctive characteristics, including the SME and high damping capacity, make NiTi highly suitable for various medical applications.

Generally, NiTi-based medical devices can be classified into two main categories: implantable devices and non-implantable devices.

Implantable devices

NiTi biocompatibility and resistance to corrosion make it suitable for long-term implantation within the human body. Moreover, NiTi's superelastic properties allow it to withstand significant mechanical stress without permanent deformation, which is particularly advantageous in dynamic environments like the cardiovascular system. Examples of implantable devices include vascular and cardiovascular applications like peripheral stents, aneurysm coils, cardiovascular luminal shields, heart valves, and septal occluders. Other examples, as shown in Figure 7, include bone plates, screws, dental arch wires, Simon IVC filters, stents, and devices for internal bone fixation [24,25].

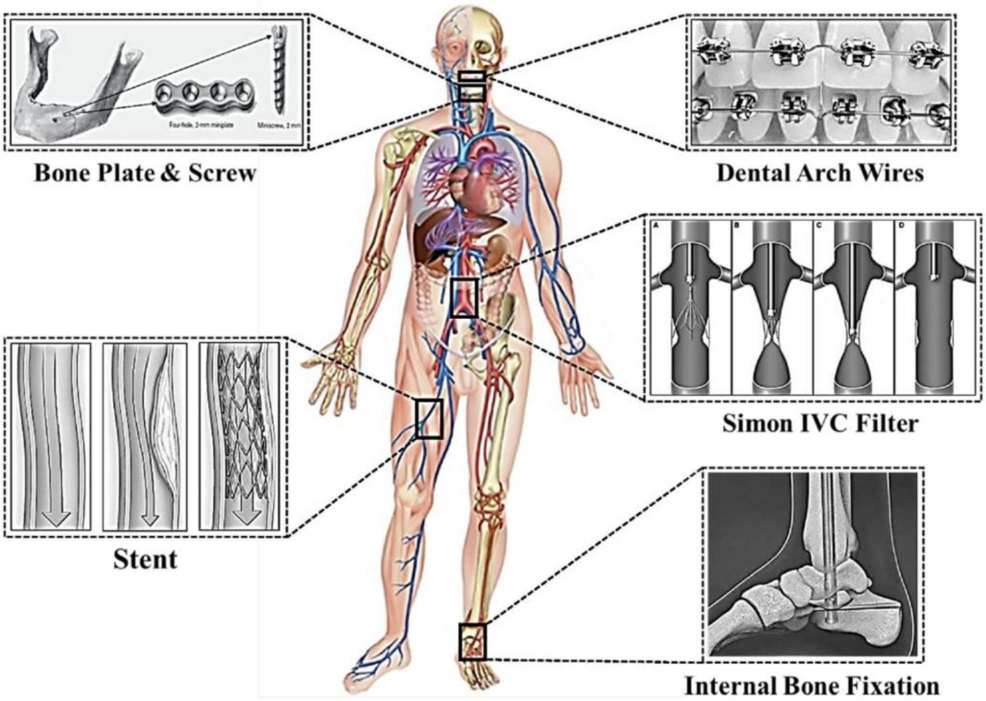

Figure 7. Examples of NiTi's medical implants in the human body [14].

Non-Implantable Devices

NiTi’s superelasticity at body temperature has made it an essential material for minimally invasive therapeutic devices. This category encompasses surgical instruments and tools used during medical procedures, such as stone and blood clot retrieval devices, endoscopes, and vena cava filters. It also includes dental instruments like endodontic rotary files and orthodontic arch wires [14].

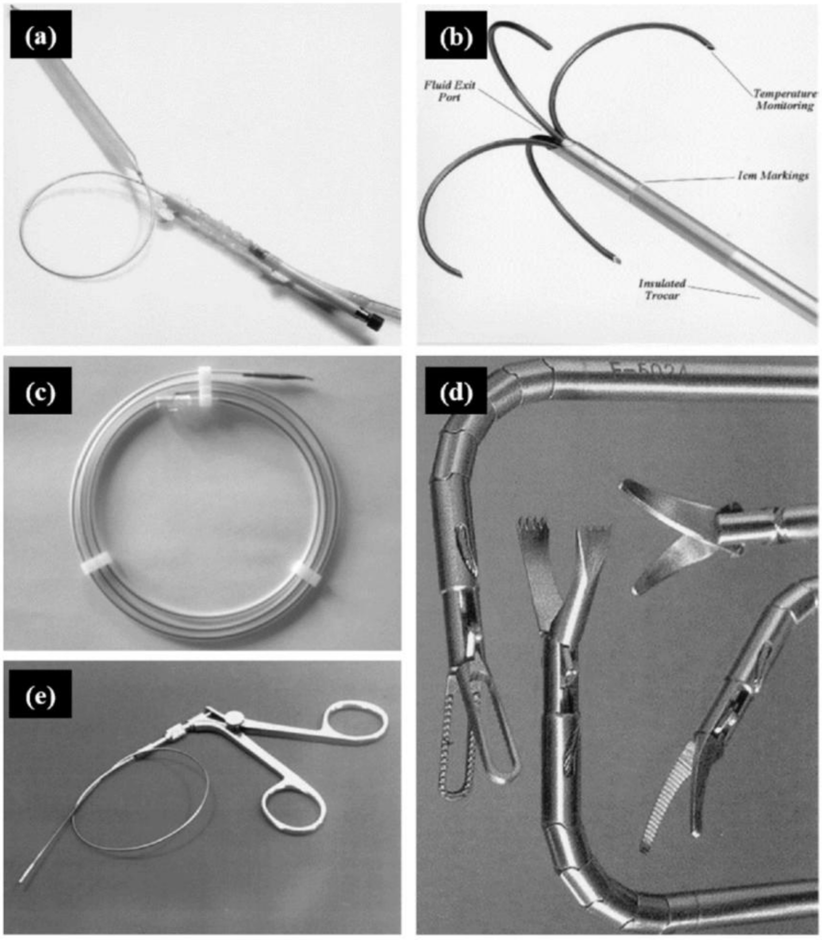

Figure 8. Examples of NiTi in non-implantable medical devices: (a) Arrow interaortic balloon pump, (b) RITA tissue ablation device, (c) guide wire, (d) grasper with NiTi tubing and internal actuation wire for knot operation, and (e) Surgical Innovations endoscopic instruments with NiTi rods for actuating scissors and graspers. Examples of NiTi in non-implantable medical devices: (a) Arrow interaortic balloon pump, (b) RITA tissue ablation device, (c) guide wire, (d) grasper with NiTi tubing and internal actuation wire for knot operation, and (e) Surgical Innovations endoscopic instruments with NiTi rods for actuating scissors and graspers[14].

1.1.4 NiTi as an actuator

Shape memory alloys (SMAs) are materials that have the ability to recover their original shape after loading through a thermally-induced crystallographic phase transition from martensitic to austenitic state [26–28]. This remarkable property makes them particularly well-suited for implementation in actuators since the SME is functional over a considerable strain range (ca. 2-5% strain) and is also characterized by a high force-to-stroke ratio [29]. The most commonly used SMA in the field of actuation is NiTi. Although the phase transition temperatures of this alloy can be varied by altering the mixing ratios of its constituent elements, NiTi is normally in martensitic phase at room temperature and typically undergoes thermal hysteresis between the martensite and austenite phases at a temperature range of 20-50 K. NiTi 's ability to undergo phase transformations in response to thermal changes makes it an excellent candidate for various actuation systems. The combination of its lightweight nature, compact size, and ability to generate significant force relative to its volume further enhances its applicability in actuator designs.

In actuator applications, NiTi can convert thermal energy into mechanical work. This capability allows it to perform tasks such as opening or closing mechanisms based on temperature fluctuations. For example, NiTi actuators are utilized in automotive applications, such as antiglare rear-view mirrors that automatically adjust based on ambient light conditions. Additionally, they are employed in microgrippers for precise manipulation of small objects in robotic systems. Another innovative application involves using NiTi in shape-morphing structures, such as aerodynamic wings or car spoilers that adjust their shape based on airflow or speed. This capability can enhance vehicle performance and fuel efficiency by optimizing aerodynamics dynamically.

The adaptability of NiTi actuators makes them suitable for various industries, including aerospace, robotics, and consumer electronics. As research progresses and manufacturing techniques improve, the potential for NiTi-based actuators continues to grow, paving the way for more advanced and efficient systems across multiple sectors.

Chapter 2: Bidirectional Actuator Based on NiTi

This chapter outlines the design challenges and methodologies for developing SMA-based actuators with enhanced functionality. Section 2.1 provides an introduction to the fundamental principles behind SMA actuation and highlights the limitations of traditional one-way SMA actuators, emphasizing the need for bias mechanisms to achieve reversibility. Section 2.2 introduces the concept of a novel SMA-based actuator incorporating a metamaterial geometry, detailing its design principles and unique properties. The theoretical model, presented in section 2.3, presents the theoretical model developed to predict the actuation performance of the system, including its global biaxial deformation capabilities. Section 2.4 describes the experimental methodology employed for prototyping and testing the actuator, while section 2.5 discusses the results and implications of the findings. Finally, section 2.6 summarizes the insights obtained from this study and their implications for future designs of SMA-metamaterial actuators.

2.1 INTRODUCTION

Since the implementation of SMAs in actuators [10–13] requires the application of a pre-strain, a stand-alone one-way SMA-based actuator is only suitable for one-time use, as once the actuator is heated it reverts to its original state and the initial level of pre-strain is not re-applied upon cooling. To avoid this design problem and impart reusability to the actuator, a so-called ‘bias’ mechanism is incorporated into the actuator, which counterbalances the actuation of the SMA component and returns it to its initial pre-strain state once the actuator is deactivated. The bias component imparts reversibility to the actuator by taking advantage of the differences in Young’s modulus between martensitic and austenitic phases (with the latter being the stiffer of the two). Ideally, the counterbalance component should ensure that the SMA component is at its maximal level of recoverable pre-strain in its cold phase while exerting the smallest possible amount of resistance to the SMA contraction upon heating [30]. This delicate balancing act between these two opposing factors is highly dependent on the relative stiffnesses, volume fractions, and type of mechanical interaction between the SMA and bias components, and careful consideration must be given at the design stage to these aspects to ensure that the optimal stroke and/or force output is obtained.

Several studies may be found in the literature regarding the design, fabrication, and implementation of SMA-based bias actuators in various applications [31]. The SMA component is typically employed in the form of wire, strip or spring, with the former two favoring high-force applications and the latter systems requiring a large stroke output. On the other hand, the bias component can be integrated in the form of a fixed weight, springs, a deformable elastic block of material, a flexing beam, or even a second, opposing the SMA component [32–43]. Furthermore, the actual actuation stroke/force of the actuator need not necessarily act in the same direction as the contraction of SMA component upon heating. It is possible to change the direction of actuation, enhance the resultant stroke and even obtain an overall elongation output instead of a contraction by mechanical design. One of the most well-known examples of such an actuator is the SMA-sandwich actuator, where the SMA component is integrated into the faces of a sandwich structure with a soft core and selective activation of the SMA component on one surface results in a tailorable flexural deformation that induces elongation of the actuator in the direction orthogonal to the contraction of the SMA component [44–50]. The resultant elongation stroke imparted by such a system can considerably exceed the actual contraction of the SMA component, but the enhanced stroke comes at the cost of a significant reduction of actuation force in the same direction.

2.1.1 Mechanical metamaterials

Mechanical metamaterials are a class of artificially engineered materials that exhibit extraordinary and often counterintuitive mechanical properties, which are rarely found in nature. These unique behaviors arise from their carefully designed microstructural geometry rather than the chemical composition of the materials used. These materials are constructed from repeating unit cells and can demonstrate remarkable static and dynamic properties, such as a negative Poisson's ratio, which is called auxetic behavior, negative compressibility, tunable stiffness, and exceptional strength-to-weight ratios. The tailored design of these materials enables them to achieve specific mechanical responses, opening up innovative possibilities for applications across a wide range of fields [51].

From a geometrical perspective, re-entrant structures, chiral honeycombs, and rotating rigid units represent the three primary classes of auxetic metamaterials, as illustrated in the Figure 9. These geometries have the potential to exhibit auxetic behavior, meaning they expand laterally under compressive loads and contract globally under tensile loads.

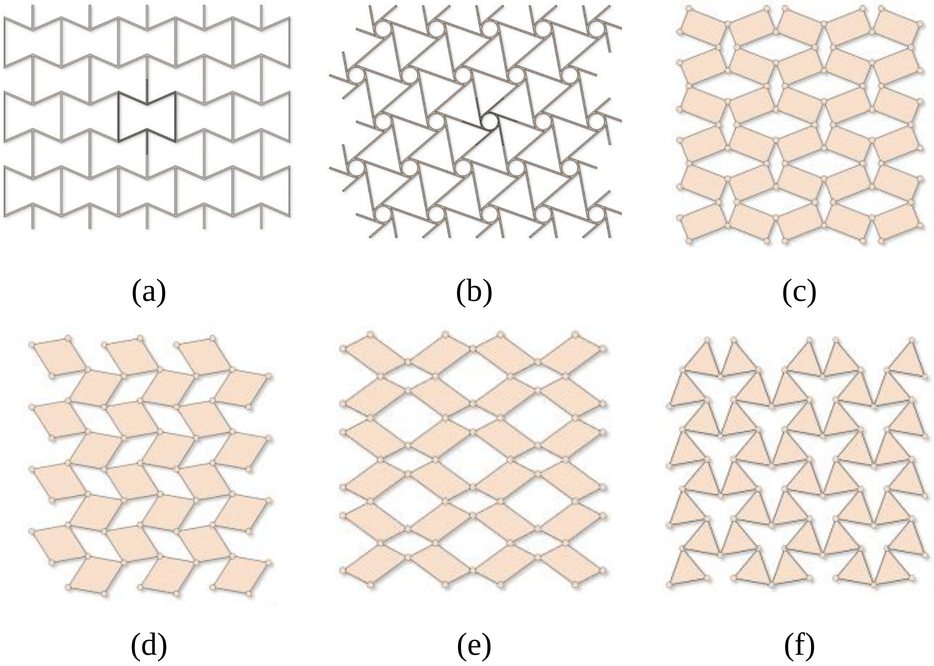

Figure 9. The three main categories of auxetic metamaterials include: (a) re-entrant hexagonal honeycombs, (b) hexachiral structures, (c) rotating rectangular plates, (d) rotating rhombohedral plates, (e) rotating parallelograms, and (f) rotating triangular plates [51].

In this work, a novel SMA-based actuator is proposed which takes this concept further and can exhibit a reversible, global elongation in multiple directions induced by the unidirectional contraction upon heating of a single SMA component. This actuator incorporates a metamaterial geometry coupled with a SMA and a bias component and takes advantage of the negative Poisson’s ratio and particular kinematic deformation mode of the metamaterial to generate a uniform controllable force/stroke output in both the axial and transverse directions. I have designed and assembled a fully-functional prototype of this actuator using additive manufacturing technology and commercially bought components and tested it under various loading conditions. In addition, I have also developed and validated a theoretical model which may be used to predict the actuation output of the metamaterial actuator based on the geometric parameters of the system and the material properties of the individual components.

2.2 DESIGN OF THE SMA-METAMATERIAL ACTUATOR

The SMA-metamaterial actuator proposed in this work is based on the rotating squares auxetic metamaterial geometry and is designed to exhibit an elongation stroke concurrently in both the x- and y-directions upon activation. The rotating squares system [52], shown in Figure 10 , is one of the most well-known geometries with the ability to exhibit a negative Poisson's ratio and belongs to a class of auxetic metamaterials known as rotating rigid unit systems. These systems include rotating rectangles [53,54], rhombi [55], parallelograms [56,57] and triangles [58,59] amongst others as well as 3D rotating polyhedra [60,61] and have the potential to exhibit giant negative as well as large positive Poisson's ratios. Like all classes of mechanical metamaterials, the mechanical properties of these systems are almost entirely dependent on their structure and can be tailored as function of the geometric parameters.

The rotating squares metamaterial, as its name implies, deforms through rotation of squares which are connected to each other at the vertices through pin-joints (in the mechanism's idealized state) [52] or through a thin strip/block of material (in a single-material perforated metamaterial system) [62–65]. It exhibits an in-plane Poisson's ratio of -1 which means that any elongation or contraction in one direction upon loading is accompanied by an identical strain in the transverse direction. In addition, as a pin-joint mechanism, the rotating squares geometry has also been shown to be completely unaffected by edge effects and deforms in the same manner in a periodic infinite, large-scale finite and small-scall finite environment. These two factors make it particularly well-suited for implementation in a biaxial actuation system.

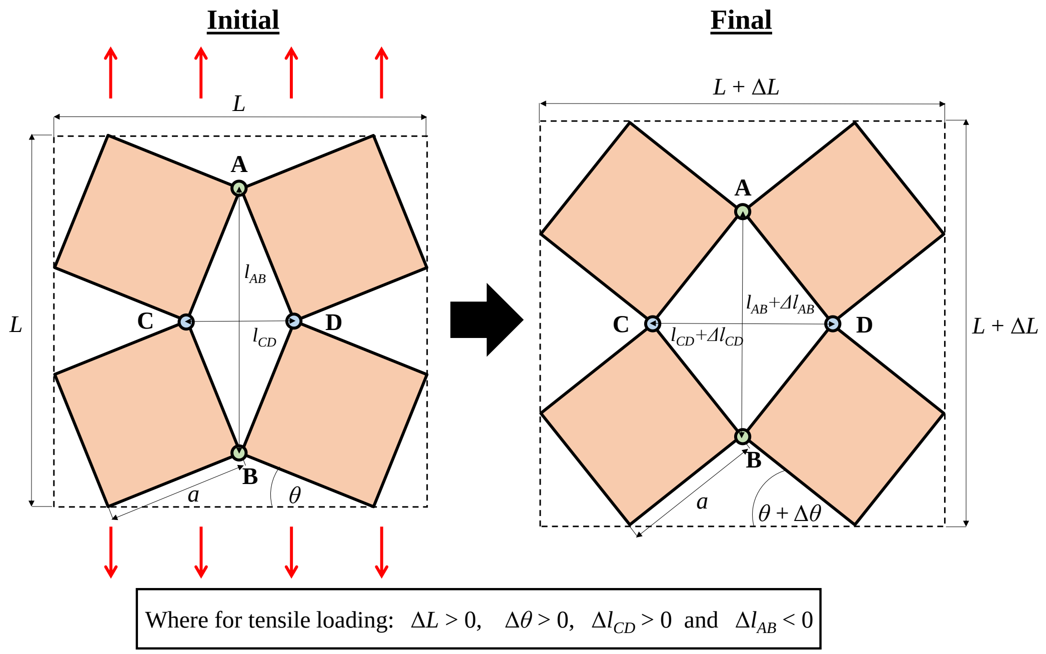

Where for tensile loading: $\Delta L > 0$, $\Delta\theta > 0$, $\Delta l_{CD} > 0$ and $\Delta l_{AB} < 0$

Figure 10. Schematic of a rotating square metamaterial unit cell before and after tensile loading.

To induce a global expansion of the actuator upon activation, it is first necessary to select the correct position for insertion of the pre-strained SMA component, which undergoes contraction upon heating. The deformation of the idealized rotation square system may be expressed in terms of the change in the angle between the square units, θ and this variable governs both the internal localized deformations of the structure and the resultant global strains. As shown in Figure 10, the SMA component must be inserted between the points marked A and B since a decrease in the distance between these two points, l_{AB}, upon rotation of the squares induces an expansion of the metamaterial system. Therefore, to quantify the relationship between the internal unit cell lengths l_{AB} and l_{CD} and the global lengths in the *x*- and *y*-directions, denoted by the *L*, these variables must be expressed in terms of the internal angle between squares, and the side length of the squares, *a*. The following terms may be obtained:

$$L = 2a[sin(\theta) + cos(\theta)] \qquad \text{Equation 1}$$

$$l_{AB} = 2a\,cos(\theta) \qquad \text{Equation 2}$$

$$l_{CD} = 2a\,sin(\theta) \qquad \text{Equation 3}$$

Since deformation occurs through a change in θ while the side length of the squares, *a*, remains constant, the relative changes in these three lengths once the metamaterial deforms may be expressed in terms of $\Delta\theta$. An example is plotted in Figure 11, where the relative lengths L/a, l_{AB}/a, and l_{DC}/a.

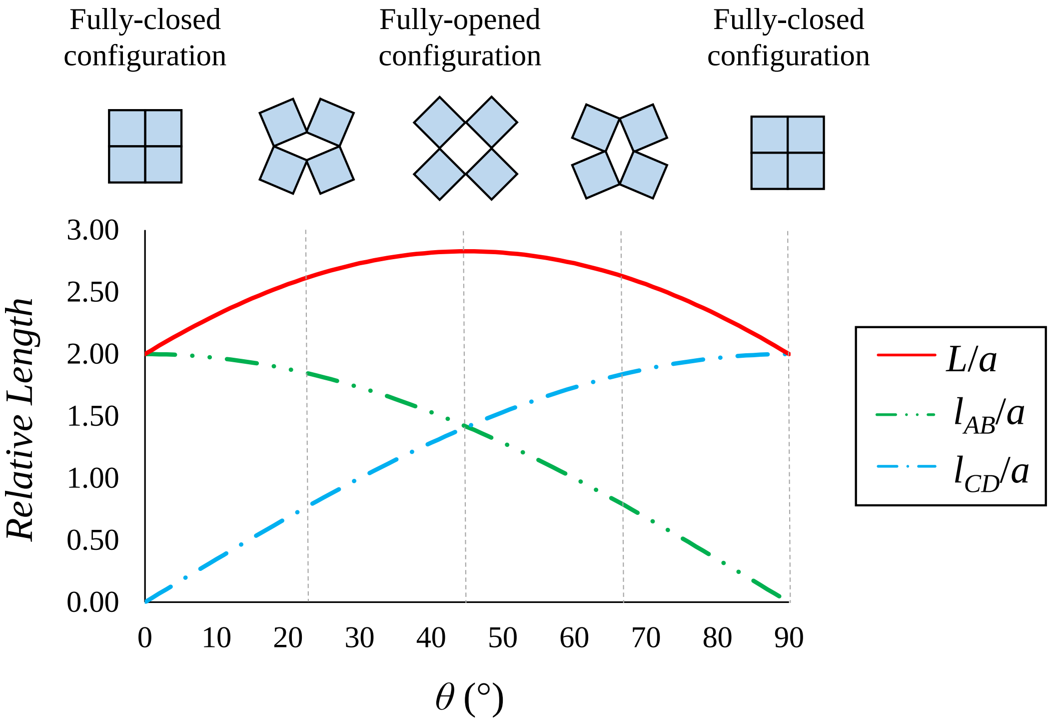

Figure 11. Plot showing the variation in relative lengths $L/a/$, l_{AB}/a, and l_{CD}/a upon varying the angle θ.

As one may observe, the resultant plot is axi-symmetric, and the system has one fully-opened configuration at θ = 45° where L/a = 2.828 and two fully closed configurations at θ = 0° and θ = 90° where L/a = 2. It is also evident that to have an inversely-proportional relationship between the lengths L and l_{AB}, the angle θ must be between 0° and 45°. Furthermore, this relationship is nonlinear and it is clear that at low θ values, a small decrease in the length of l_{AB} results in the largest relative increase in L.

2.3 THEORETICAL MODEL

Before a prototype SMA-metamaterial actuator based on this concept can be produced, it is necessary to first develop analytical expressions which may be used to predict the actuation output of the system as a function of the material properties of the individual components and the overall geometry of the system. As stated in the previous section, this actuator consists of three components: the SMA, the bias component and the metamaterial geometry; each of which has a distinct role to play in ensuring the overall functionality of the composite system. The SMA component induces the actuation of the system, the bias component imparts reversibility upon deactivation and reusability to the actuator, while the metamaterial geometry controls the actuation stroke and force output of the system in the axial and transverse directions. These three components are shown in Figure 12, where in order to maximize the actuation stroke output, the SMA component is placed in position l_{AB} and the bias component in position l_{CD}. This means that, as illustrated in Figure 11 the contraction of the SMA component upon activation is counteracted by an elongation of the bias component imposed through the kinematic constraints of the rotating squares metamaterial deformation mode. Since $l_{AB} > l_{CD}$, this also induces an overall positive actuation stroke of the actuator, i.e. L increases.

To quantify the actuation stroke of the system, it is necessary to equilibrate the forces and displacements of the SMA and bias component along the direction l_{AB}. Since the SMA component is aligned along l_{AB}, the force-displacement plot obtained from uniaxial loading of this component can be used directly, as shown in Figure 12 (green and red lines). However, this is not the case for the bias component, which is oriented in a direction perpendicular to l_{AB}. Therefore, the forces and displacements exerted by the bias component in the direction l_{AB}, which are necessary to equilibrate the system, must first be found through the kinematic laws that define the deformation of the metamaterial system.

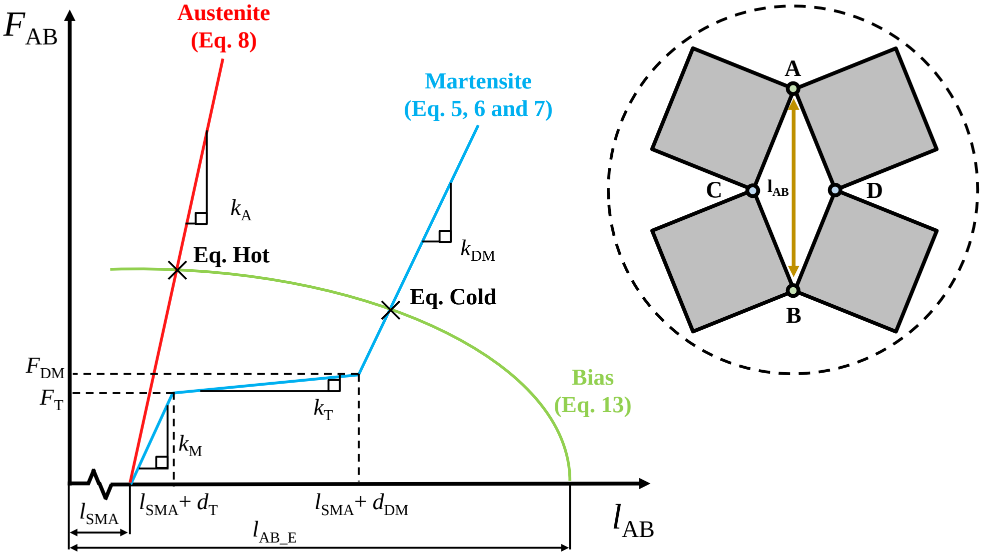

Figure 12. A qualitative plot showing the forces and displacements acting along l_{AB} for the SMA in martensitic (blue) and austenitic state (red) and the opposing bias component (green). The equilibrium points at the SMA hot and cold states are also indicated.

2.3.1 Assumptions

The model, which predicts the actuation output of the system on the basis of the equilibrium of forces generated by the interaction between the SMA and bias component, is based on a number of assumptions, listed below:

- The metamaterial geometry exerts a solely kinematic influence on the deformation of the overall system and does not contribute any internal energy in terms of work done to the actuator. The influence of factors such as friction at the joints of rotating units and weight is considered to be negligible.

- The stress-strain behavior of the SMA component at the martensitic phase can be represented in terms of a tri-linear model with each line representing the twinned martensite state (M), transition state (T) and detwinned martensitic state (DM), respectively (see Figure 12). On the other hand, the austenitic state is represented by a linear model. This approach corresponds with that utilized in previous works found in literature pertaining to analytical and numerical analyses of SMAs [30,66–68].

- Upon activation/heating, the SMA component undergoes a complete transition from martensitic to austenitic phase. This is typically the case for SMA systems with a small cross-sectional area such as wires and strips activated through the Joule effect.

- The model is static and, hence, the deformation of both the SMA and bias component is elastic, fully recoverable and unaffected by the velocity of activation (transformation from martensitic to austenitic phase is almost instantaneous once activated through the use of an electrical current).

The pre-strain of the SMA component is also fully induced by the elastic bias component, which in this case was assumed to be an elastomer or a spring which deforms linearly over high strains. This means that during assembly of the actuator, the SMA component should ideally be introduced first within the system at a pre-determined length, l_{SMA}, followed by the insertion of the elastic bias component. In order for the bias component to exert a pre-stress on the SMA component, the initial length at rest of the bias component, l_E, must be less than the length l_{CD} which corresponds to the length l_{AB} of the SMA component. This condition may be expressed as follows:

$$l_E < \sqrt{4a^2 - l_{l_{SMA}}^2} \qquad \text{Equation 4}$$

and it ensures that the pre-strain applied to the bias component in order to integrate it within the actuator imparts sufficient force to counterbalance the SMA and induces a pre-strain in the latter component.

At this point, it is important to note that although the bias component deforms axially in a linear elastic manner, the fact that it is placed in a position which is perpendicular to the SMA component, means that the equilibrating force induced by the bias component in the direction l_{AB} is nonlinear and kinematically dependent on the metamaterial geometry used. Thus, in Figure 12, the force-displacement plot of the bias component along l_{AB} is represented by a nonlinear curve.

2.3.2 Geometry-Force calculations

As stated previously, the force-displacement relationship of the SMA component in its martensitic phase is represented by a tri-linear model. The SMA has an initial length of l_{SMA} at rest and the model (shown in Figure 12) may be expressed in terms of force (F_{AB}) and total length (l_{AB}) along the line between the points A and B as follows:

$$\begin{aligned} &F_{AB} = k_M(l_{AB} - l_{SMA}), \\ &\text{where} \quad l_{SMA} \le l_{AB} < (l_{SMA} + d_T) \end{aligned} \qquad \text{Equation 5}$$

$$F_{AB} = F_T - k_T(d_T + l_{SMA} - l_{AB}),$$
$$\text{where} \quad (l_{SMA} + d_T) \leq l_{AB} < (l_{SMA} + d_{DM})$$ Equation 6

$$F_{AB} = F_{DM} - k_{DM}(d_{DM} + l_{SMA} - l_{AB}),$$
$$\text{where} \quad (l_{SMA} + d_{DM}) \leq l_{AB}$$ Equation 7

where k_{M}, k_{T} and k_{DM} are the stiffness constants for the twinned martensitic state, transition state and detwinned martensitic state, respectively, while F_{T}, d_{T}, F_{DM} and d_{DM} represent the force (*F*) and displacement (*d*) thresholds required to switch from the first to second state (Equation 5 to Equation 6) and the second to third state (Equation 6 to Equation 7). These three lines represent the force-displacement Behavior of the martensitic SMA in the twinned, transition and detwinned state respectively and are valid within the limits defined in the equations.

This approach to modelling the force-displacement of martensitic SMA is identical to the analytical method employed previously by the same authors to model uni-axial bias actuator behavior [30] and is analogous to the Souza-Auricchio numerical method [66,67] used in many commercial FE software. The equations are expressed in terms of stiffness constants, transformation displacements and forces rather than Young's moduli, strains and stresses in order to ensure that these equations may be applied to an SMA component in any form, be it as a wire, strip, spring or even more complex geometric forms. In the case of SMA wires, as used in the experimental part of this work, these terms may easily be derived directly from basic stress-strain plots, while for other forms less straightforward analytical expressions may be required to obtain these constants. Similarly, the austenitic force-displacement behavior (indicated in Figure 12 by the red line) is represented by the following linear model:

$$F_{AB} = k_A(l_{AB} - l_{SMA})$$ Equation 8

where k_{A} represents the stiffness constant of the SMA in its austenitic phase.

On the other hand, as shown in Figure 12, the force-displacement behavior of the bias component counteracting the SMA is represented by a non-linear model along the line AB. This is due to the fact that although the stiffness of the bias component *per se* is constant, it is aligned along the line CD, orthogonal to the line AB. This means that the force component exerted along the line AB as a result of the elongation of the bias component varies non-linearly as a function of the initial configuration of the rotating square metamaterial as shown in Figure 13(c).

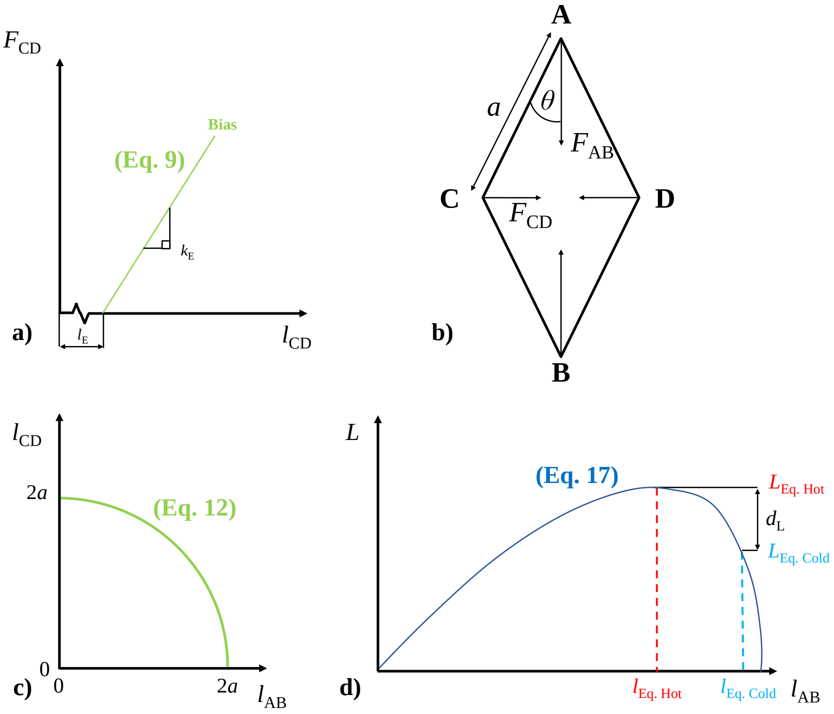

Figure 13. a) A qualitative plot showing the linear force-displacement model used to describe the deformation of the elastic bias component along the line between points C and D. b) A diagram showing the forces (F_{AB} and F_{CD}) acting along the directions l_{AB} and l_{CD} in the central pore between the rotating square units. c) A plot showing the relationship between changes in the lengths l_{AB} and l_{CD} and d) a graph showing the relationship between overall actuator length in axial and transverse direction, L, and the internal length parameter l_{AB}.

The force-displacement relationship along the line CD for the elastic bias component may be defined by Equation 9.

$$F_{CD} = k_E(l_{CD} - l_E)$$ Equation 9

where l_E is the initial length of the elastic bias component and k_E is the associated stiffness constant (see Figure 13(a)). This equation can be used to find the resultant force and displacement acting along line AB through the following kinematic and geometric relationships (shown in Figure 13(b)):

$$F_{AB} = \frac{F_{CD}}{\tan\theta}$$ Equation 10

$$\theta = arccos\left(\frac{l_{AB}}{2a}\right) \qquad \text{Equation 11}$$

$$l_{CD} = \sqrt{4a^2 - l_{AB}^2} \qquad \text{Equation 12}$$

which in turn can be used to obtain the following non-linear model for the bias component along line AB (shown in Figure 12):

$$F_{AB} = \frac{k_E\left(\sqrt{4a^2 - l_{AB}^2} - l_E\right)}{tan\left(arccos\left[\frac{l_{AB}}{2a}\right]\right)} \qquad \text{Equation 13}$$

The cold equilibrium point, shown in Figure 13, is the point at which the force exerted by the martensitic SMA component and the counteracting elastic bias component are equal. Ideally this point should be met at the detwinned martensitic state of the SMA component in order to ensure that the actuation stroke is completely recovered once the actuator is deactivated as demonstrated in [30]. Therefore, the resultant length at the cold equilibrium point, $l_{AB\ Eq.C}$, may be found by solving Equation 7 and Equation 13. Once the SMA component is heated and undergoes a reverse transformation, this equilibrium point shifts to the point where Equation 8 and Equation 13 are equal. By solving these two equations, one may find the resultant length at the hot equilibrium point, $l_{\mathrm{AB\ Eq.H}}$.

Once the lengths l_{AB} of the actuator when the SMA is in its martensitic and austenitic phase, $l_{\mathrm{AB\ Eq.C}}$ and $l_{\mathrm{AB\ Eq.H}}$, are known, these variables can be used to find the corresponding cold and hot equilibrium global lengths of the actuator, $L_{\mathrm{Eq.C}}$ and $L_{\mathrm{EQ.H}}$ (shown in Figure 13(b))), through Equation 14 and Equation 15:

$$L_{Eq.Cold} = l_{AB\_Eq.Cold} + \sqrt{4a^2 - l_{AB\_Eq.Cold}^2} \qquad \text{Equation 14}$$

$$L_{Eq.Hot} = l_{AB\_Eq.Hot} + \sqrt{4a^2 - l_{AB\_Eq.Hot}^2} \qquad \text{Equation 15}$$

These equations define the relationship between the contraction of the SMA wire and the global metamaterial geometry and are obtained through the expansion of the generic Equation 1.

The difference between these two values results in the predicted global actuation stroke in the axial and transverse directions, dL, as follows:

$$d_L = L_{Eq.Hot} - L_{Eq.Cold} \qquad \text{Equation 16}$$

Due to the nonlinearity of the relationship between L and l_{AB} (Equation 17), shown in Figure 13(d), it is evident that in order to obtain the maximum actuation stroke, dl, $l_{AB\ Eq.Cold}$, should ideally be close to the maximum permissible value of l_{AB}, i.e. $l_{AB} \rightarrow 2a$. This means that the initial configuration of the rotating squares metamaterials should ideally be at a θ value close to 0°. Yet, it is also important to note that one must be careful to ensure that the initial length of the SMA component, l_{SMA}, is not equal or almost equal to $2a$ since this would entail that the bias component cannot exert any meaningful pre-stress on the wire due to the rotating squares mechanism being blocked in its fully-opened state. Thus, the initial length of the SMA component which allows one to obtain the maximum permissible actuation for a given bias component must first be found through the analytical model.

$$L = l_{AB} + \sqrt{4a^2 - l_{AB}^2} \qquad \text{Equation 17}$$

To summarise, the model presented in this section demonstrates how the actuation stroke of the metamaterial actuator may be predicted and tailored as a function of metamaterial configuration and material properties of the SMA and bias components.

2.4 EXPERIMENTAL SET-UP

Bearing in mind the insights obtained from the theoretical model described in the previous section, a prototype actuator is designed based on this concept which is able to impart a global biaxial actuation. As detailed in the following sections, the metamaterial was printed using a fused-deposition method (FDM) 3D printer as four separate parts and assembled using commercially bought components. The SMA component was integrated within the system in the form of a thin wire attached between points A and B and was heated by passing through an electric current from a power supply while the bias mechanism was incorporated through the insertion of a number of elastic bands at points C and D of the actuator in order counter the contraction of the SMA wire upon heating.

2.4.1 Thermo-mechanical characterization of the SMA wire

A NiTi shape-memory wire with a diameter of 0.23 mm was used in this work. The chemical composition of the wire provided by the supplier is presented in Table 1. A thicker sample of wire (diameter 0.43 mm) with the same chemical composition was previously characterized by Panciroli [69] and it was found that the wire has a martensitic finish transformation temperature of 40°C (315 K) and an austenitic finish transformation temperature of 79°C (353 K). In order to characterize the force-displacement and stress-strain behavior of this wire at complete martensitic and austenitic phases, a sample was subjected to tensile loading using Galdabini® tensiometer. The wire was affixed to screws from both ends and trapped using two nuts. The screws were then inserted into two ABS 3D-printed holders which are clamped by the jaws of the tensile loading machine as shown in Figure 14(a).

Table 1. Percentage chemical composition of NiTi wire [69].

Ni	**Co**	**Cu**	**Cr**	**Fe**
55.42	0.005	0.005	0.005	0.005
Nb	C	H	O	Ti
0.025	0.037	0.001	0.033	44.46

The wire sample tested had an effective length of 206 mm and was tested at room temperature and under heated conditions (i.e. at complete martensite and austenite phases respectively). The wire was subjected to a two-step loading and unloading cycle. For the martensitic test, a tensile elongation of 24 mm at a speed of 6 mm/min was applied followed by a return to the initial position at the same speed. Before initiating the test, the samples were pre-heated and allowed to cool off gradually in order to ensure that any pre-strain applied to the wire during the clamping process is removed. For the austenitic test, a smaller tensile elongation was applied, and the wire was heated by the Joule effect throughout the duration of the entire loading and unloading procedure. This was done by connecting a power supply to the screws to which the SMA wire was affixed and applying a current of 0.75 A. In order to ensure that the applied current is sufficient to induce an austenitic transformation, the resistivity of the wire was measured prior to the tensile test at low and high ranges of current and was found to be 8.92×10^{-7} Ωm and 6.36×10^{-7} Ωm, respectively. These values are comparable with those found in literature for martensitic and austenitic nitinol wires [70]. Once the test sample is mounted, the ABS 3D-printed holders ensure that the wire is isolated from the metallic clamps of the tensile loading machine and that the current heats up the wire. The following stress-strain graph, shown in Figure 14(b), was obtained following data smoothening procedures to eliminate minor noise in the data points.

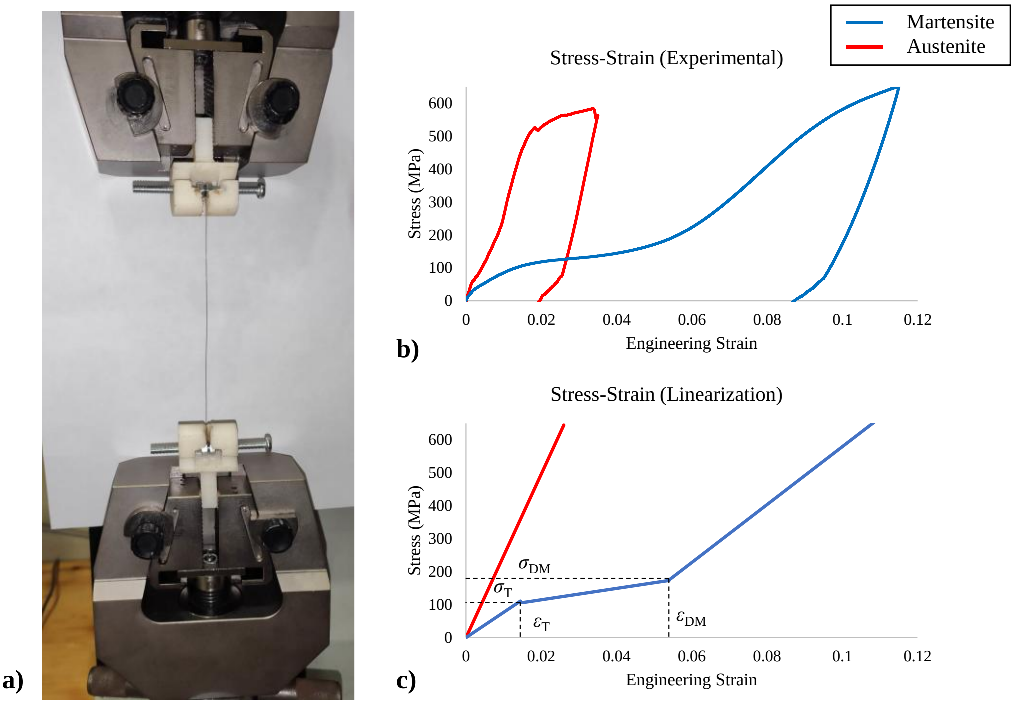

Figure 14. a) Image showing how the SMA wire was set up for the tensile loading test. b) Stress-strain plot of the SMA wire in martensitic and austenitic state and c) linearization of the experimental plot used to obtain the parameters implemented in the theoretical model (see Table 3).

2.4.2 Additive manufacturing and assembly of the SMA-metamaterial actuator

The rotating square metamaterial structure was designed to function as a single unit cell pin-joint system with minimal stiffness. The four identical square units making up the system were designed using SolidWorks® (see Figure 15(a, b, g)) and additively-manufactured from Onyx® material using a Markforged® FDM 3D-printer. These square units were designed with an effective side length, *a*, of 70 mm and an out-of-plane thickness of 20 mm. In order to lower the mass of the squares and avoid unnecessary waste of material, the squares were designed as thick truss systems with a cross pattern, which ensures that the squares retain their rigidity whilst minimizing the volume of printing material used [71]. The base metamaterial system was then assembled with the addition of metal commercially-bought hinges (see Figure 15(d)) which were attached to the square units through screws, positioned at points A and B shown in Figure 6e. On the other hand, the squares were connected at points C and D through the 3D printed pin-joints shown in Figure 15(f). In order to support the actuator on a surface without influencing its in-plane deformation, spherical rolling bearings were attached to the center of each of the four rotating square units (see Figure 15(c)). Lastly, the joints (both plastic and metallic) and spherical bearings were all lubricated with machine grease in order to minimize friction.

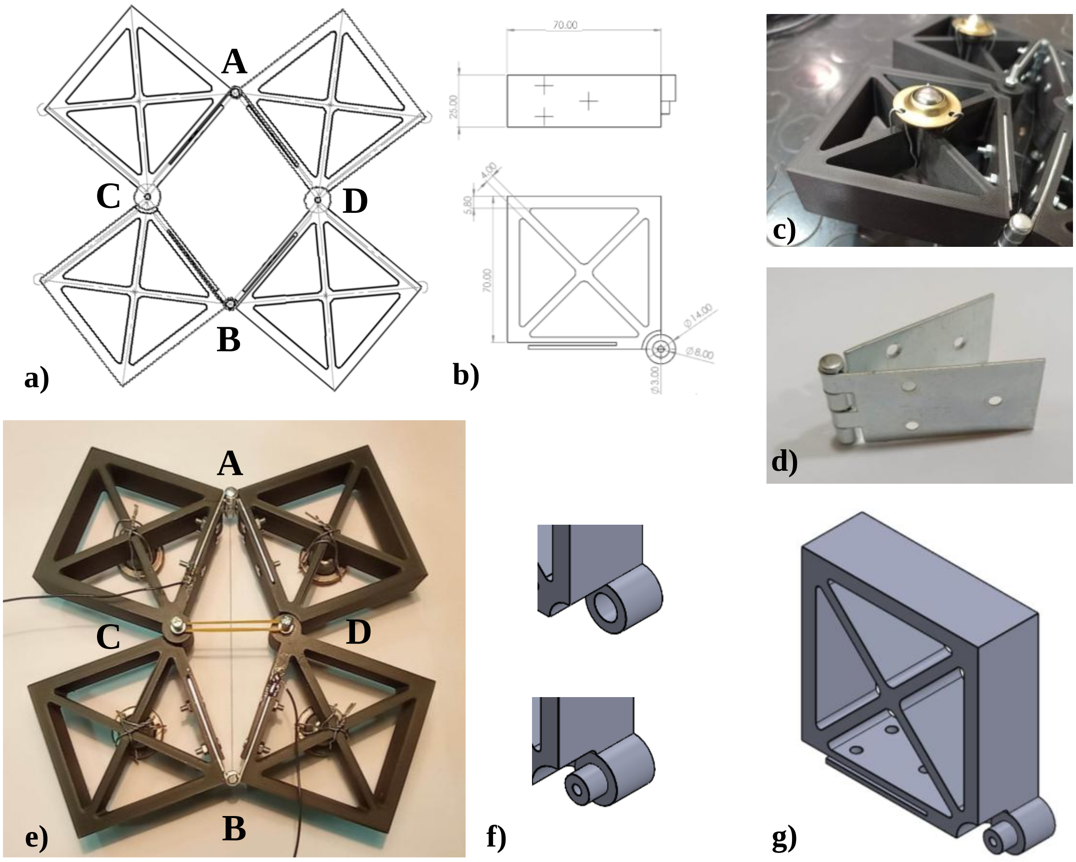

Figure 15. Technical drawing of a) assembled and b) individual rotating square units making up the actuator. c) Spherical bearings used to minimize friction between the supporting surface and actuator and d) metallic hinges inserted in points A and B of the system. e) SMA-metamaterial actuator showing the wire inserted between points A and B, the elastic rubber bands (bias mechanism) between points C and D and the wiring connecting the metallic hinges to the power supply. Figures f) and g) show a zoomed in version of the joints at points C and D which are jointed together through the insertion of a metal M3 screw.

A length of SMA wire was inserted into the actuator by attaching it to points A and B through the use of knots. The initial length of the wire used varied between different experimental runs, but in each case, it was chosen on the basis of resulting in a metamaterial configuration which has a θ value between 10° and 20°. The latter limit ensures that the inverse relationship between lengths l_{AB} and L is retained while the former guarantees that the level of pre-strain imparted by the bias mechanisms to the SMA wire does not result in the length l_{AB} surpassing the mechanical limit of l_{AB}/a = 2.828 which is equivalent to a geometrically unrealizable $\theta < 0°$ value.

Moreover, in order to ensure that any slippage of the wire during experimental testing is detected, the original length of the wire was marked with white corrective fluid after pre-heating it to eliminate any pre-strain applied during the assembly process. Following the insertion of the SMA, the bias component was added to the system in the form of elastic rubber bands attached to the protruding screws in positions C and D. The rubber bands (with an initial length, l_E, of 25 mm) were tested under tensile loading conditions using an extensiometer and were found to have an average linear stiffness of 0.1 MPa over a strain range of 0% to 160%. The system was then allowed to equilibrate before proceeding with the actuation tests. To activate the actuator by heating up the SMA component, a power supply was used and, following preliminary testing, it was found that a current of 1 A for a time period of 10 seconds was sufficient to guarantee that the wire reached its complete austenitic transformation. The power supply was connected to the actuator by soldering the wire to the metal hinges as shown in Figure 15(e) rather than directly to the SMA wire, in order to ensure that the connections do not interfere with the deformation of the actuator.

2.4.3 Experimental test runs

Three experimental runs were conducted in order to verify the functionality of the prototype SMA-metamaterial actuator. In the first test, a single elastic rubber band was used as a bias mechanism, in the second, two, and, lastly, in the third, three. The initial length of the SMA wire, l_{SMA}, for each test is listed in Table 2. In each testing run, the actuator was activated and deactivated 10 times in a row in order to analyses the reversibility of actuation stroke and reusability of the actuator. This was done through sequential 10 seconds of activation (with a current of 1 A from a power supply) followed by 60 seconds of deactivation in order to allow the SMA wire to cool and return completely to its martensitic state. The deformation of the actuator was captured using a digital camera (Nikon®) with a frame rate of 5 Hz. Key frames were extracted from the recorded video, and displacement measurements were carried out manually. In this methodology, a set of four points A, B, C and D of the actuator along with the external corners of the rotating squares, were tracked in order to obtain the experimental values of l_{AB}, l_{CD} and L throughout each activation and deactivation cycle, as shown in Figure 16. The global actuation stroke, d_L, for each cycle was calculated as the difference between the length of L before and after activation.

Table 2. List of parameters for three experimental tests run.

Test Number	**No. of Elastic Bands**	**Initial Length of SMA wire (mm)**
I	1	110.2
II	2	111.5
III	3	117.2

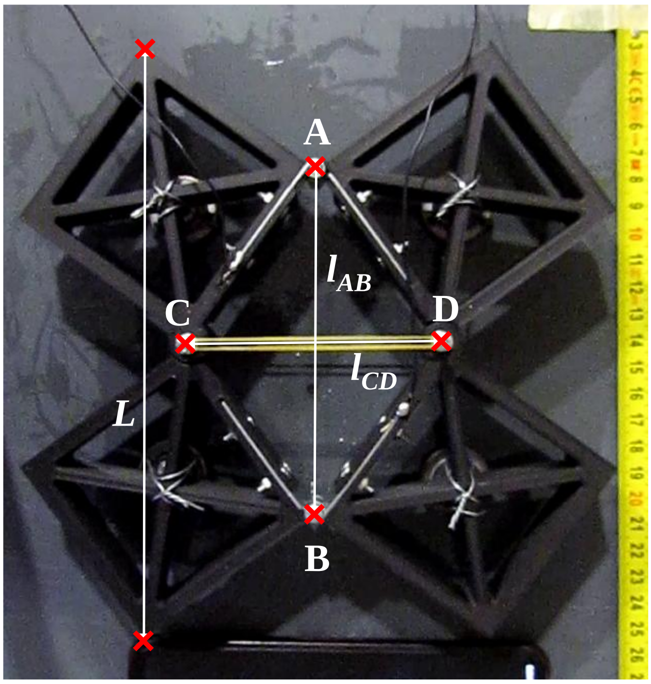

Figure 16. Image showing the points which were tracked using image correlation techniques (marked with a cross) in order to measure lengths l_AB, l_CD and L.

2.5 RESULTS AND DISCUSSION

The resultant global actuation stroke, d_L, obtained for each experimental run with respect to the number of activation/deactivation cycles, along with images of the actuator in its activated and deactivated states are presented in Figure 17. It is clearly evident from the plots that while in Test I the actuation stroke was almost nail, in Test runs II and III, a significant actuation stroke is observed which remained more or less stable over 10 consecutive activation/deactivation cycles, undoubtably demonstrating both the functionality and reversibility of the prototype actuator. Moreover, as shown in Figure 17(a), the actuation stroke is biaxial, and the rotation of the square units is plainly visible indicating that the pin-jointed metamaterial structure is indeed deforming as intended.

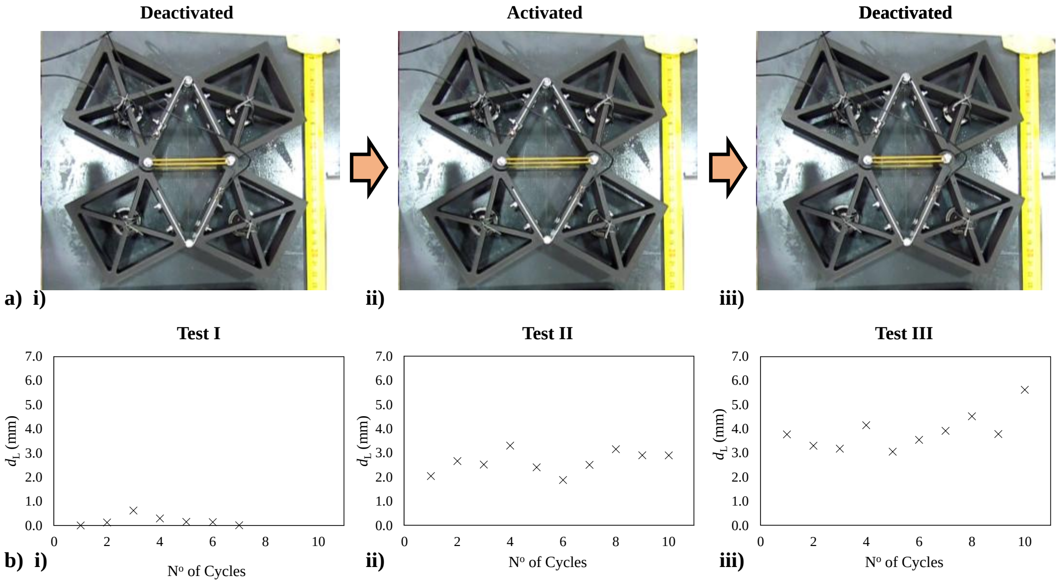

Figure 17. a) Images showing the second cycle i) deactivated actuator, followed by ii) activation and iii) deactivation] of the actuator with 3 elastic rubber bands (Test III) b) Plots showing the resultant global actuation stroke measured for each activation/deactivation cycle of the three experimental tests listed in Table 2. Note that in Test I, the number of cycles was terminated early due to the fact that almost no actuation stroke was observed over repeated cycles.

In order to analyze these results in the context of the predictions of the theoretical model presented in Section 3 of this article, it is necessary to first obtain the Young's moduli, E_A, E_M, E_T and E_{DM}, transformation stresses, σ_{T} and σ_{DM}, and strains, ε_{T} and $\varepsilon_{\mathrm{DM}}$, of the SMA in martensitic and austenitic phase. Utilizing linear regression, the following constants, presented in Table 3, were obtained from the stress-strain plot shown in Figure 14(b).

Table 3. Young's moduli, transformation stresses and strains obtained from the austenitic and martensitic stress-strain plot shown in Figure 5b.

SMA Parameters			
EA	24815.14 MPa	$f_{t.}$	0.015
EM	7614.26 MPa	σ_{T}	106 MPa
ET	1724.63 MPa	$\varepsilon_{\mathrm{DM}}$	0.054
EDM	8790.63 MPa	σ_{DM}	175 MPa

These terms can be used to obtain the corresponding stiffness constants and transformation forces and displacements necessary to plot the tri-linear martensitic model (Equation 5- Equation 7) and linear austenitic model (Equation 8) as follows:

$$k_A = \frac{E_A A}{l_{SMA}}$$ Equation 18

$$k_M = \frac{E_M A}{l_{SMA}}$$ Equation 19

$$k_T = \frac{E_T A}{l_{SMA}}$$ Equation 20

$$k_{DM} = \frac{E_{DM} A}{l_{SMA}}$$ Equation 21

$$F_T = \sigma_T A$$ Equation 22

$$F_{DM} = \sigma_{DM} A$$ Equation 23

$$d_T = \varepsilon_T l_{SMA}$$ Equation 24

$$d_{DM} = \varepsilon_{DM} l_{SMA}$$ Equation 25

where A is defined as the cross-sectional area of the SMA wire ($\pi d^2/4$) and l_{SMA}, the length of the wire. The initial lengths used for each test are listed in Table 2. For the elastic rubber bands, the stiffness constant of a single rubber band, k_{R}, was equal to 0.1 MPa and, thus, the stiffness constant used to plot the force/displacement plot of the bias mechanism, k_{E}, may be found as follows:

$$k_E = N k_R$$ Equation 26

Where N is the number of rubber bands used in each test (listed in Table 2).

Utilizing these constants, the simultaneous equation pairs: Equation 7 and Equation 13, and Equation 8 and Equation 13, were solved numerically in order to obtain the cold and hot equilibrium points, $l_{AB\,Eq.C}$ and $l_{AB\,Eq.H}$, respectively. These values were then used to find the predicted actuation stroke, d_L, for each of the three experimental test runs using Equation 14 -Equation 16. These theoretically predicted values are plotted along with the average value of the global actuation stroke obtained from the experimental results in Figure 18.

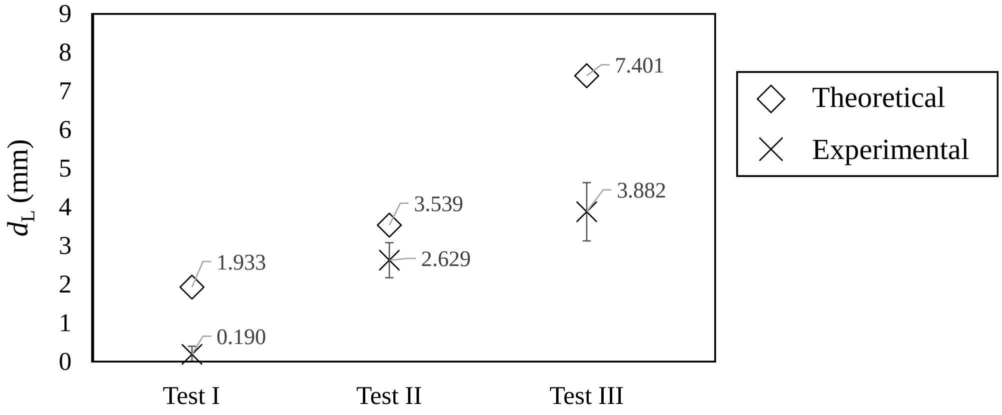

Figure 18. The plot showing the comparison between the theoretical d_L values predicted by the analytical model and the corresponding average experimental values (over 10 cycles) with standard deviation.

It is evident from Figure 18 that while the theoretical model overestimates the experimental actuation stroke, particularly for Tests I and III, the trends obtained using both methods are congruous with each other. The discrepancies in the magnitude of the values were also to be expected since the experimental prototype does not completely conform with all the assumptions used to derive the analytical expressions. For example, the model assumes ideal frictionless rotation of the square units, however some friction is always present despite the lubrification of the joints and the use of spherical bearings. Moreover, the model does not take into account the influence of functional fatigue, which cannot be disregarded completely for actuator configurations where the SMA component is subjected to a high initial level of pre-strains such as in Test III. In view of this, the theoretical model is envisaged to be primarily utilized as a pre-design tool for the fabrication of SMA-metamaterial actuators since it has the highest accuracy for predicting the initial actuation cycles of the system.

The results obtained from the tests on the metamaterial actuator prototype also provide a number of additional insights on the functionality of this actuator. In the case of Test I, where only one rubber band was used, it was clearly evident that the force generated by this elastic bias component was not sufficient to guarantee a sufficient level of pre-strain to the SMA component in order to allow it to reach its complete detwinned martensitic state. This, in turn resulted in an extremely low actuation stroke output (as also predicted by the theoretical model) as well as decreasing the amount of recoverable actuation stroke due to the fact that the cold equilibrium point is reached at the transition phase of the martensitic SMA. This highlights the importance of having a bias component that is capable of generating the necessary level of pre-strain in the SMA component, elsewise the actuation output will be extremely low. However, whilst increasing the level of pre-strain will give a higher actuation stroke, it is also important to keep in mind that a large pre-strain value will lead to an increase in the fatigue of SMA component, resulting in yielding, and thus a decrease in functionality, occurring at a lower number of actuation cycles. This factor was, in fact, particularly evident in Test III. Although the plot shown in Figure 17(biii) indicates an almost constant actuation stroke, d_L, throughout the 10 activation/deactivation cycles, a closer analysis of how the absolute value of the global length of the actuator, L, varies with each cycle (see Figure 19a(ii) and 10(b)) shows that this value is significantly decreasing after every cycle despite the actuation stroke remaining constant. This indicates that the SMA wire is undergoing irreversible yielding with each cycle due to the high level of pre-strain imposed by the bias mechanism (in this case 3 rubber bands). This effect is not visible in the Cycle No° vs d_L plot shown in Figure 17(biii) due to the fact that the elastic bias mechanism is undergoing a large level of pre-strain itself and thus the actuation stroke lost due to yielding relaxation of the SMA component is re-gained by the imposition of an additional increment of pre-strain on the wire. This leads to an initial masking of the SMA yielding effect which is advantageous if maintaining a constant actuation stroke is the main function of the actuator, however it is also expected to result in a more rapid deterioration of actuator functionality over time. On the other hand, in the case of Test II, it is clear that the change in L is minimal over 10 cycles and that both actuation stroke and absolute actuator dimensions remain almost constant (see Figure 19(ai)). This indicates that out of the three configurations tested, this is the one which shows the best performance since it is characterized by an appreciable actuation stroke while the observed yielding of the SMA component is minimally over 10 cycles.

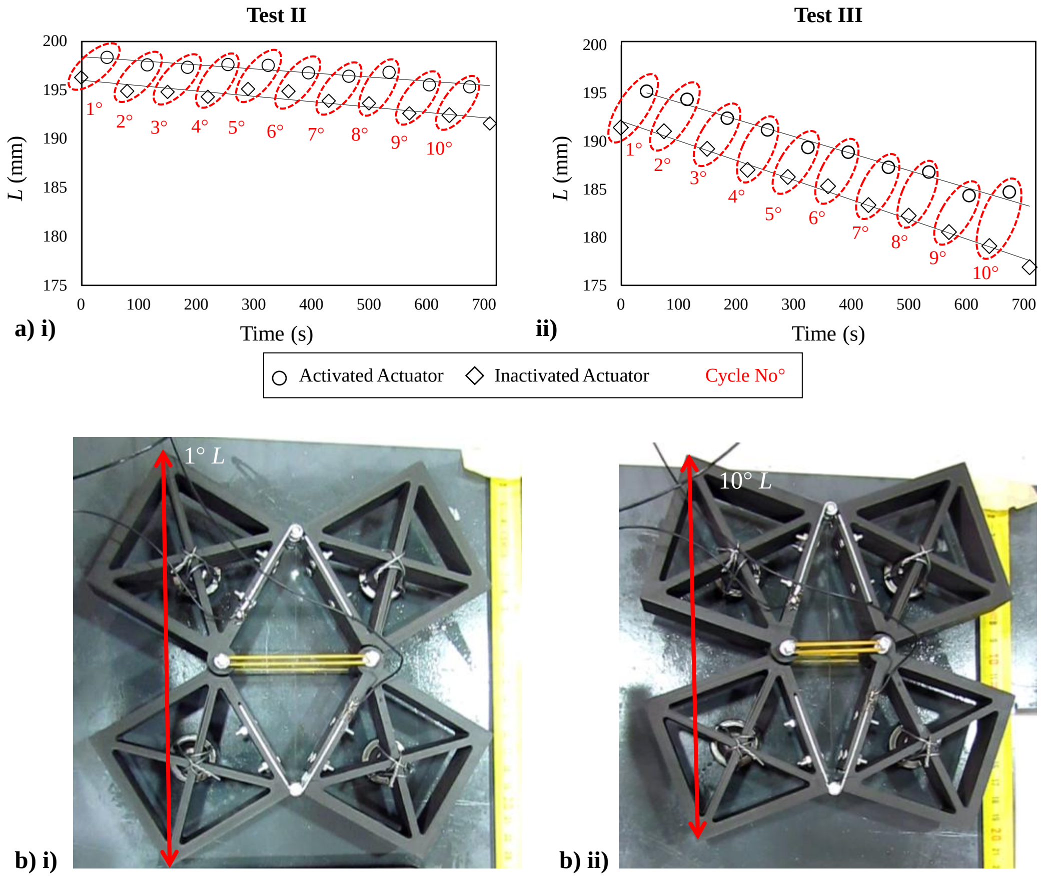

Figure 19. a) Plots showing how the absolute value of *L* changes over testing time for i) Test II and ii) Test III. The dotted red lines indicate the actuation cycles while the black lines are plotted by linear regression of the actuator in its activated and deactivated state separately in order to roughly indicate how *L* changes over time. b) Images showing the difference in the deactivated configuration of the actuator in Test III after i) the 1° cycle and ii) the 10° cycle.

From the insights obtained from the theoretical model and experimental results, it is clear that in order to design an SMA-metamaterial actuator with optimal performance based on the rotating squares mechanism, one should aim to:

- Ensure that the bias mechanism used exerts sufficient force on the SMA component in order to bring it to the highest possible allowable pre-strain value which does not result in irreversible yielding effects. By reaching the optimum equilibrium point one can obtain the highest actuation stroke of the SMA component while minimizing loss of functionality due to fatigue.
- Design the rotating square metamaterial system in such a way as to have an initial configuration at the cold martensitic equilibrium point which has a

low θ value. This ensures that the actuation stroke of the SMA component ($L_{Eq.Hot} - L_{Eq.Cold}$) is amplified to its maximum level and translates in a large global actuation stroke, d_L.

Before concluding, it is imperative to point out that the SMA-metamaterial actuator proposed and prototyped in this work is merely one example which illustrates the potential of this new class of SMA actuators. The main advantage of using a metamaterial geometry to control the global actuation output of an SMA-based actuator lies in the fact that one can manipulate the deformation of these systems based on geometry. Thus, the designer has a variety of options to choose from when designing these types of actuators in order to obtain a tailored and desired output. For example, the actuator presented in this work, which is designed to exhibit a biaxial positive stroke, can easily be changed into an actuator which delivers a biaxial negative stroke (i.e. overall global contraction) simply by inverting the positions of the SMA wire and bias component, i.e. placing the SMA wire in position CD and the bias mechanism in position AB. Furthermore, the force exerted by the bias mechanism can be tuned simply by changing its placement with respect to the SMA component. By changing the position (such as for example attaching it to the center of the rotating squares), one can alter the bias force it exerts in counteracting the SMA component and hence one can simply optimize the SMA-bias equilibrium point as a function of bias component positioning rather than by using a different material.

The use of a biaxial actuator which is activated through the uniaxial deformation of a single component such as the one proposed in this work presents various advantages over traditional biaxial actuators powered by separate components for each direction. The most obvious advantage is the reduced risk of unequal actuation in the transverse and axial directions in case of a malfunction. Since the global actuation stroke is induced solely by a single SMA component and is kinematically governed by the metamaterial geometry, the ratio of axial to transverse actuation stroke is fixed by design and cannot physically change while the system is in place. This means that if actuation is blocked in a single direction, then by default it is also obstructed in the orthogonal direction, thus retaining the uniformity of bi-directional actuation. This, in turn, also reduces the need for constant recalibration of the actuator after use, as is the case for biaxial actuators which are driven by separate, independent components for each direction. This property makes metamaterial-based actuators particularly well-suited for potential future use as platforms for biaxial loading testing rigs as well as implementation in deployable structures requiring tailored biaxial actuation.

Finally, it is important to emphasize that while in this work the main aim was to design a reversible actuator capable of producing an equal biaxial actuation stroke and, hence, the auxetic rotating square mechanism with a characteristic Poisson's ratio of -1 was chosen, a plethora of other rotating structures may be found within the literature, which may be used to design similar actuators with different advanced functionalities. For example, certain configurations of the rotating rectangle mechanism are known to have the capability of exhibiting giant negative/positive Poisson's ratio and one may take advantage of this property to simply greatly amplify the actuation stroke of the standalone SMA component in a single direction. On the other hand, if one wishes, for instance, to design an actuator which exhibits an equal tri-axial deformation, rotating systems with trigonal in-plane symmetry such as rotating triangle structures may be used as a basis for such an actuator. All in all, the possibilities for designing and realizing SMA-metamaterial actuators with multi-axial actuation capabilities and geometrically-tailored outputs are nearly endless, and I believe that the results presented in this work will give rise to further studies on this interesting class of smart composite structures.

2.6 SUMMARY AND IMPLICATIONS

In this work, I have designed a new reversible SMA-based actuator with an equal biaxial actuation stroke based on an auxetic metamaterial structure. Through the use of the rotating square system, which is characterized by a Poisson's ratio of -1, the axial unit-directional contraction of the SMA component upon activation is translated into a biaxial global expansion of the overall actuator. An experimental prototype of this actuator was manufactured and assembled and then tested under three different configurations over 10 activation/deactivation cycles. A theoretical model which may be used as a pre-design tool for the realization of SMA-metamaterial actuators with a tailored actuation stroke has also been developed and its predictions compared with the experimental results. This work highlights the potential of SMA-metamaterial actuators for implementation in systems requiring a multi-axial actuation output and I hope that the findings presented in this work will function as a blueprint for the design of other metamaterial-based SMA actuators with advanced functionalities.

Chapter 3: NiTi Stent for Biomedical Applications

This chapter provides a comprehensive exploration of the development, design, and optimization of self-expanding (SX) NiTi stents, with a focus on their application in minimally invasive treatments for vascular diseases. It begins with an introduction (section 3.1) to atherosclerosis, the clinical motivation for stent development, and an overview of percutaneous vascular interventions (PVI) as a preferred treatment method. Section 3.13.1.1 reviews the historical evolution of stents, from early bare-metal designs to advanced drug-eluting and biodegradable stents, highlighting key advancements and challenges. Section 3.1.2 classifies stents based on material properties and deployment methods, emphasizing the distinct roles of balloon-expandable and self-expanding stents. Sections 3.1.3 through 3.1.5 delve into the material properties, geometrical designs, and figures of merit critical to optimizing stent performance.

Finally, the chapter delves into the manufacturing techniques employed in the fabrication of NiTi stents, with a particular focus on braiding, laser cutting, and AM.

Section 3.2 focuses on the optimization of braided stents to enhance their mechanical performance and adaptability to complex vessel geometries. This goal is achieved through FE simulations and optimization techniques, with detailed results from the Multi-Objective Particle Swarm Optimization (MOPSO) algorithm presented in subsection 3.2.5 derived from analytical modelling and validated through FE analysis (subsection 3.2.4). The results and discussion in subsection 3.2.6 provide a comprehensive analysis of the stent's improved performance metrics, highlighting key insights into the relationship between design parameters, and their influence on radial force, stiffness, and foreshortening under simulated physiological conditions.

Section 3.3 explores the laser-cutting technique, with the Scitech-Solaris stent as a case study. The stent's design, featuring a hybrid open- and closed-cell structure, is detailed in subsection 3.3.3, with precise dimensions obtained through microscopic imaging and integrated into CAD models. subsection 3.3.4, introduces the superelastic NiTi material model, refined through experimental testing and FE simulations. The discussion in subsection 3.3.5 highlights the capability of simulations to evaluate the impact of various geometrical design parameters, providing insights into optimizing the stent's performance.

Section 3.4 addresses the emerging field of AM, emphasizing its transformative potential for creating next-generation, patient-specific stents. The section provides an overview of AM's advantages and challenges, including its ability to fabricate complex geometries and tailor stents to individual patient anatomies, moreover it focuses on laser-based powder bed fusion (LB-PBF) and its key process parameters. Challenges such as anisotropy and surface roughness are addressed in Subsection 3.4.2 with solutions including chemical etching and heat treatments.

Together, these sections present a comprehensive understanding of the manufacturing processes and design considerations necessary for advancing NiTi stent technology.

3.1 INTRODUCTION

Atherosclerosis is the hardening and narrowing of blood vessels caused by the accumulation of plaque or lipid deposits lining the vessels over time, causing vascular occlusion, and affecting the blood flow. Severe atherosclerosis could lead to diseases like coronary artery disease, cardiovascular disease, peripheral artery disease (PAD), and other cardiovascular pathologies. Historically, traditional surgical operations have been utilized to address severe cases of atherosclerosis. However, in recent years, percutaneous vascular intervention (PVI) has emerged as one of the most effective alternative treatments [72]. Unlike traditional open surgery, PVI is a minimally invasive treatment in which a catheter with a balloon or stent is inserted into a stenosed or occluded vessel to open it up and restore the cardiovascular circulation which has been clogged by atherosclerosis. Percutaneous transluminal angioplasty (PTA), venoplasty, and stenting are different types of PVI techniques. PTA involves inserting and inflating a balloon within the narrowed artery to compress the plaque away and widen the vessel lumen, while venoplasty extends this concept to the venous system, addressing stenoses/occlusions and restoring venous patency by using a similar balloon dilation technique in veins rather than arteries [73]. Stenting, on the other hand, involves placing a stent in the stenosed/occluded vessel permanently to provide structural support and prevent the vessel from recoiling and re-narrowing. A stent is a tiny tubular structure, which is in most cases made of metal, to support and maintain the patency of narrow or blocked vessels. Compared to traditional open surgery methods, PVI stenting offers several clinical advantages. By eliminating the need for conventional open surgery, PVI stenting minimizes patient trauma, operation time, hospital stays and convalescence. Beyond its clinical implications, PVI stenting is advantageous on the economic side for both healthcare systems and patients, as it decreases the need for prolonged hospitalization, post-operative care, and rehabilitation expenses. Additionally, PVI stenting provides benefits on the social side by offering patients faster recovery times and lowering re-hospitalization chances, allowing them to return to their daily activities sooner.

PAD presents a significant economic burden; the annual costs on hospitalization alone in the U.S. exceeding $21 billion [74]. As stated previously, stenting has emerged as a promising solution in endovascular peripheral applications due to their remarkable mechanical properties and potential clinical benefits. However, the success of stenting relies on a comprehensive understanding of key factors influencing stent performance.

3.1.1 Evolution of stents

The word "stent" was first used in the context of medical devices in the mid-20th century. It is named after a British dentist, Dr. Charles T. Stent, who contributed to the development of materials used in making early medical devices [75]. He designed and developed a stainless steel “coil spring graft” successfully placed in the femoral artery of a dog [76]. He also developed NiTi coil wire stents [77] that led future research on stenting [78]. In 1986 doctors U. Sigwart and J. Puel placed the first stainless steel stent into the stenosed lesion of a man, immediately following balloon angioplasty [79–81]. After this first intervention, the use of stents grew exponentially and there has been continuous improvement in the design and materials of the stents since then. Unfortunately, the first generation of bare metal stents (BMSs) showed in-stent restenosis (ISR) rates up to 20%, leading to necessary re-intervention [82]. ISR is a gradual re-narrowing of a stented vessel segment that can occur a few months after stent placement [83]. Adverse effects were not only caused by the stent itself, but also by its malapposition and, in general, by the deployment methods [82,84]. Nevertheless, research on nondegradable BMSs rapidly led to the development of better performing stents characterized by good processability, mechanical properties, and economical efficiency which are currently in use for various treatment of cardiovascular diseases

[84]. A decade later, the first drug-eluting stents (DESs) were used, improving clinical outcomes by minimizing ISR rates down to 4% [82]. DESs, like BMSs, have the base platform made of stainless steel, CoCr alloys, NiTi alloys, or other biocompatible alloys, but they also provide drug delivery (e.g. paclitaxel, everolimus) through coating technology (polymer-controlled or polymer-free). Localized drug delivery was an important improvement in the development of better-performing stents, resulting in a decrease in ISR rates, however, the problem of stent thrombosis (ST) [81] remained unsolved. Stent thrombosis is more common in perioperative peripheral arterial disease patients, especially those with chronic total occlusion lesions. Factors such as stent type, loss of collaterals, and edge restenosis contribute to stent thrombosis. Additionally, complex lesion characteristics, dual antiplatelet therapy duration, and stent fractures play a role in stent thrombosis [85]. Non-stented thrombosis rates affecting the femoro-polpliteal district vary with different angioplasty methods. Histopathological studies reveal collagen deposition, intramural calcification, and thrombotic material in chronic total occlusion lesions, which affect stent expansion. Short dual antiplatelet therapy duration may significantly contribute to stent thrombosis. Disease location, especially in superficial femoral artery stents, influences stent thrombosis risk [86,87]. Distal stent locations contribute to worse long-term outcomes due to contiguous popliteal and infrapopliteal disease [88,89].

Ideally, a stent, after being implanted and having performed its function for the expected timeframe, would disappear. Although this is utopian, considerable research has been carried out on the development of biodegradable/bioresorbable stents (BDSs/BRSs), both with a polymeric or metallic platform. The degradable polymers include polylactic acid (PLA), poly-L-lactic acid (PLLA), polycaprolactone (PCL), racemic polylactic acid (PDLLA) and many others. The degradable alloys include magnesium, zinc and iron alloys [80]. The use of BDSs would bring many clinical benefits, such as avoiding adverse events associated with the presence of the stent in the vessel, recovering the unimpeded vasomotion [90] of vessels (which was due to the presence of a “foreign body” like a stent), and the possibility for the patient to undergo MRI (magnetic resonance imaging) without concerns [91]. Unfortunately, initially developed BDSs had strut thicknesses much higher than their nondegradable counterparts to compensate for their weaker mechanical properties [82], especially due to the low elastic modulus of the biodegradable material. BDSs are still considered a promising development, but their associated drawbacks mean that there is still need for further investigations before they can be widely utilized [81].

3.1.2 Classification of stents

Stents can be classified based on different factors, such as the stent's topology, material selection and deployment method. Here, I classified them based on the material properties and subsequent insertion/deployment method, which can be either self-expanding (SX) or balloon-expandable (BX).

Balloon-expandable and self-expanding stents. In BX stents, the stent is mounted on a balloon-tipped catheter and deployed at the plaque site by means of a guidewire. When the stent is in place, the balloon is inflated, causing the stent to expand and apply radial pressure against the vessel walls. This breaks the plaque, which is often calcified, recovering the vessel patency, and providing structural support. After deployment, the balloon is deflated and removed, leaving the stent in place due to plasticization of the material Figure 20(a). Conversely, SX stents are designed to expand on their own once deployed due to their inherent material properties. These stents are crimped onto a delivery system inside a sheath and deployed in position. Upon release from the delivery system, the sheath is removed, and the stent expands until it reaches the vessel wall, exerting outward pressure to keep the vessel open. The expansion is due to the superelastic recovery of the NiTi alloy from which the stent is made, as elaborated upon in the next section. Like BX stents, SX stents are left in place permanently to provide long-term support, prevent vessel recoil, and maintain blood flow Figure 20(b).

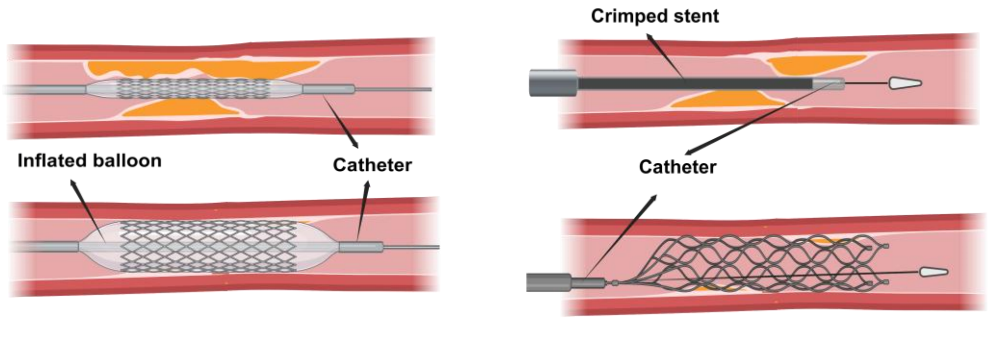

(a) (b)

Figure 20. Two deployment methods of stents: (a) balloon-expandable stents, (b) self-expanding stents.

It must be noted that angioplasty or other vessel preparation techniques can be performed before inserting a SX stent [92] for several reasons, including preparing the lesion site by dilating the narrowed artery, facilitating stent positioning and deployment, debulking atherosclerotic plaque to create space for stent placement, and reducing the risk of complications. This preparatory step is particularly crucial in cases of calcified lesions or tortuous vessels to ease stent delivery and ensure optimal stent function. More often SX stents require post dilation balloon angioplasty to reach full expansion and proper arterial wall apposition. SX stents exhibit continued expansion over several days until they reach their maximum diameter, typically occurring within a few weeks following implantation [79] as opposed to BX stents, where the maximum diameter is achieved immediately upon implantation.

During the manufacturing process, BX stents are produced in a crimped state and then expanded to the diameter of the vessel by inflating a balloon, resulting in the stent being plastically deformed. Therefore, BX stents must be able to withstand plastic deformation to maintain the required size after deployment [93,94]. On the other hand, SX stents are typically designed with a slightly larger diameter than the vessel in which they will be deployed, therefore, they must possess sufficient elasticity to be crimped into the smaller delivery system before expanding in the desired position [94]. The lower elastic modulus of SX stents, compared to BX stents, makes them more compliant and therefore easier to insert, thus reducing the risk of stent dislodgement and migration [93,95].

BX stents have limited radial compliance compared to SX stents, making them more susceptible to permanent deformation when exposed to external forces. This limitation affects their performance in arteries like the femoro-popliteal district ones, which experience significant deformation (torsion and bending) during daily activities. SX stents are better suited for dynamic arteries with large biomechanical deformation such as these [96]. SX stents can also better adapt to the artery’s shape and diameter, making the deployment easier and minimizing trauma during implantation [97]. BX stents show less recoil in comparison to their SX counterparts when placed in calcified lesions, hence they are still preferred for renal and coronary stenting [93].

All this indicates that SX and BX stents have important differences for clinical and mechanical purposes and their suitability for insertion is primarily determined by the type of the vascular system in question. In this review, I will focus primarily on SX stents and their applications in venues and arterial vessels.

3.1.3 Available materials for stents

The selection of materials for stent fabrication is a critical aspect, which involves several key factors to ensure optimal performance and patient safety. The primary concern is the biocompatibility of the stent, ensuring that it does not induce any adverse reactions when deployed into the patient's body. Furthermore, the stent material must have radiopacity, allowing for easy detection under fluoroscopic imaging to ensure the stent is positioned accurately during deployment. Moreover, it is crucial to select a stent material with excellent corrosion resistance to avoid corrosion, as this significantly impacts the long-term durability and performance of the stent [98].

In addition to the previously mentioned characteristics, stents require specific mechanical properties as a result of a balance between stiffness (required to sustain dilation and resisting elastic recoil of the vessel) and compliance (to accommodate bending during the deployment phase and during the body movement).Figure 21(a) shows a typical stress-strain curve illustrating the behavior of ceramics, metals, and polymers. Unlike ceramics, which have a low fracture toughness and lack plasticity, and polymers, which struggle to achieve sufficient strength and stiffness, metals are an excellent choice for manufacturing stents due to their natural balance of elasticity and rigidity compared to other materials [99]. Generally, the metals often used in stent manufacturing include 316L stainless steel (316L SS), cobalt-chromium (CoCr), NiTi, titanium (Ti), magnesium (Mg) alloys, pure iron (Fe), platinum-iridium (PtIr) alloy and tantalum (Ta) [84,94].

The characteristics of materials required for stents vary depending on the application. NiTi is one of the most effective materials for SX stents [98,100]. In fact, a SX stent must undergo large deformation and have quite low elastic modulus to maintain its compliance, allowing it to be crimped inside a sleeve for delivery and expanded after deployment [101,102]. On the contrary, BX stents must have high modulus of elasticity for minimum recoil and possess high strength and the ability to work also slightly beyond the elastic region [94,98], making the stainless steel an appropriate material for this kind of stents [98].

Figure 21(b) shows the static stress-strain curve of stainless steel and NiTi, where it can be seen that, thanks to its superelastic behavior, NiTi could reach large deformations (more than 8%) [103], and yet being capable of recovering its initial shape. It is worth noting that this work is intended to focus its attention on NiTi SX stents.

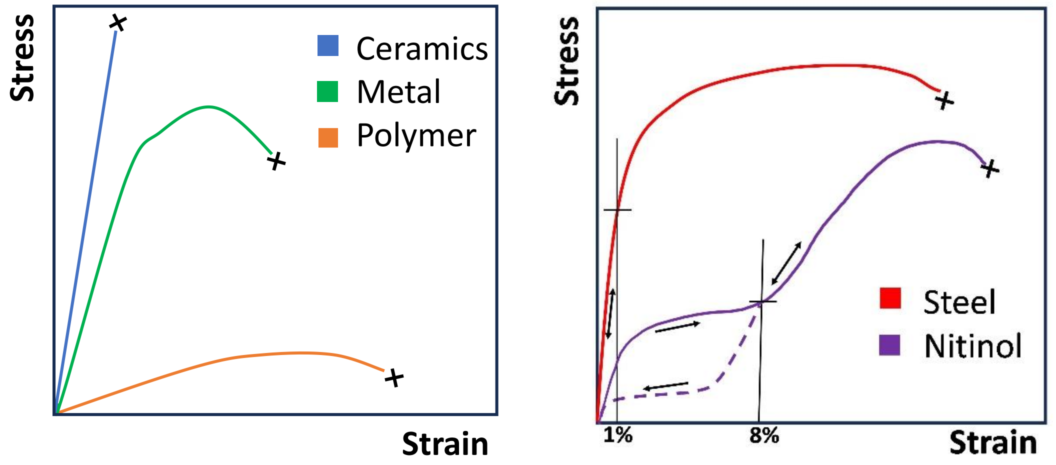

(a) (b)

Figure 21. (a) Qualitative stress-strain curves of metals, ceramics, and polymers, adapted from [99], (b) stress-strain curve of stainless steel and NiTi, adapted from [104].

NiTi satisfies the requirements for medical applications, due to its excellent biocompatibility, mechanical properties, and corrosion resistance. However, it is important to note that NiTi’s inherent radiopacity is lower than that of traditional stainless-steel stents, which can hinder clear visibility under imaging techniques such as fluoroscopic and X-ray imaging [105]. This visibility is essential for accurate stent placement and effective post-procedure monitoring. To address this limitation, radiopaque markers made of high-density materials (platinum, gold [106] and tantalum [107]) are inserted at key points of the stent and significantly enhance visibility during imaging. This approach offers practical solutions to enhance the stent's visibility without compromising its mechanical properties.

For the case of SX stent design, it is possible to benefit from the SE of NiTi as the performance of a SX stent is dependent on the ability of the material to store elastic energy whilst it is constrained in the delivery system, making it an ideal choice for manufacturing this kind of stents [100]. Most of the NiTi stents can be crushed until they are almost completely flat and yet return to their original shape without any permanent deformation. This feature is especially important in superficial vessels like the carotid artery that are vulnerable to external crushing [100].

The shape memory properties of the NiTi are not utilized in stenting applications, since the transition temperatures (which are dependent on the stoichiometric element ratio) ensure that the material never transitions to the twinned martensitic phase at body temperature.

In most cases, after the insertion of SX stents, additional angioplasty procedures are also performed to help the stent better performance and efficiency [93,108] and this procedure increases the complexity of the force displacement path of a NiTi stent during deployment. For instance, based on the work of T.W. Duerig and M. Wholey [93], Figure 22 shows a schematic to clarify this point by showing normalized radial forces (N/mm) on the stent and on the vessel, with respect to their diameters (mm), in three phases of stent deployment. The dashed blue line depicts the initial crimping of the stent, from a completely uncrimped stent (maximum diameter, no radial force on it (point **a** in the Figure 22), to a crimped state (minimum diameter, maximum radial force on it, point **b** in the Figure 22). Upon release from the sheath, the stent expands until it encounters the inner wall of the vessel at point **c**. From this point the force on the vessel increases until the stent and the vessel find an equilibrium diameter and stress (point **d** in the Figure 22). Further expansion is then achieved through balloon angioplasty, extending the stent to point **e**, which in turn causes the vessel to expand to the same diameter (point **e'**). Following balloon deflation, compressive force from the vessel is exerted on the stent, causing it to recoil to the diameter at point **f**. This marks the final equilibrium in stress and diameter between the stent and the vessel. It should be noted that the stiffness during the loading of the stent, k_l (initial crimping phase and last recoiling phase after angioplasty) is larger than the stiffness during the unloading, k_u, of the stent, according to the hysteresis cycle due to the superelastic nature of the material.

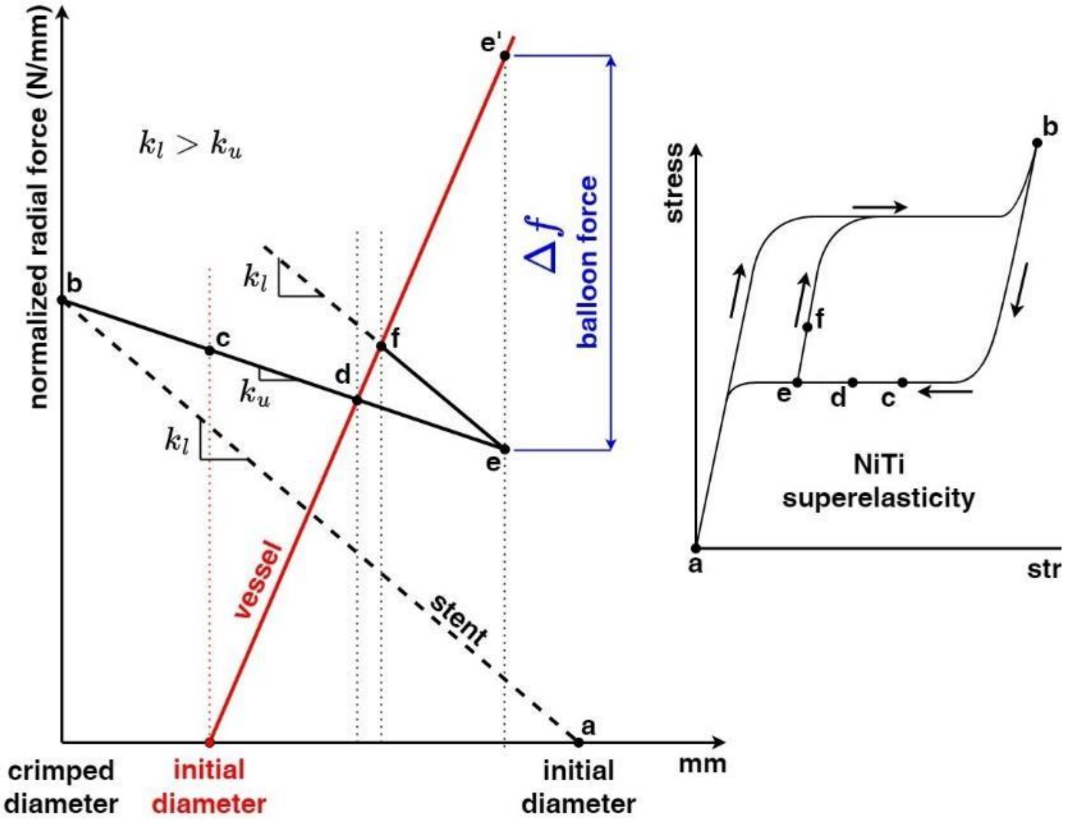

Figure 22. Schematic (adapted from [93]) of radial force exerted by a NiTi SX stent when deployed in a vessel with subsequent angioplasty as a function of the diametral dimension (left) and schematic stress-strain curve of superelastic NiTi (right).

Path	Force-displacement diagram	Stress-strain diagram
a →b	Minimum stent diameter, max force reached with k_l stiffness	First loading phase, max stress and strain
b → c	Stent deployment, force decrease with k_u stiffness, onset of vessel impingement	Unloading following lower stiffness branch
c →d	Stent and vessel reach a first equilibrium point in **d** (before balloon angioplasty)	
d → e / e'	Balloon inflation, vessel expansion to point **e'**, stent expansion to point **e**	
e / e' → f	Balloon deflation, vessel and stent reach last equilibrium point	Second loading phase due to vessel elastic spring back

3.1.4 Figures of merits of SX stents

This section investigates some of the main figures of merit associated with SX NiTi stents, highlighting key mechanical characteristics and performance indicators essential for evaluating their effectiveness in clinical settings [109]. Each property plays a crucial role in determining the functionality and durability of stents within the dynamic environment of the human body. Understanding these figures of merit is essential for both stent designers and healthcare professionals to ensure optimal patient outcomes and minimize complications associated with stent implantation. These figures of merit are intended to help the designer to fully exploit the potential of AM technology in designing the new generation of stent and, to this end, the list focuses on the mechanical behavior of the stents rather than the clinic aspects, which can be evaluated only with proper trials. The figures of merit identified here are a comparison tool for various stent designs. In this work I decided to adopt an approach based on general definitions, without having a reference stent as a benchmark, due to great variability in the design of commercially available stents.

Foreshortening

Once the stent is expanded radially, it becomes shorter in the axial direction because of Poisson’s effect, as shown in Figure 23. The term used to describe this phenomenon is called foreshortening and can be calculated through the Equation 27 where L_0 represents the initial stent’s length before deployment in the vessel, while L_D represents the final length of the stent after it has been inserted in the blood vessel.

A stent with an excessive axial reduction is very difficult to precisely position at the atherosclerotic plaque site. This difficulty can lead to incomplete coverage of the plaque, causing damage to the thin endothelial layer and reducing the treatment's efficacy [80,110].

The axial misalignment, that in the most severe cases could also lead to the migration of the stent inside the vessel, is related both to the deployment procedure and to the foreshortening and it must be considered as one of the potential clinical problems which undermines the stent efficacy in restoring the vessel patency [111].

To enhance the performance of the stent, and have better clinical outcomes, foreshortening should be minimized [79,80], with the ideal target being zero.

$$Foreshortening = \frac{L_0 - L_D}{L_0} \qquad \text{Equation 27}$$

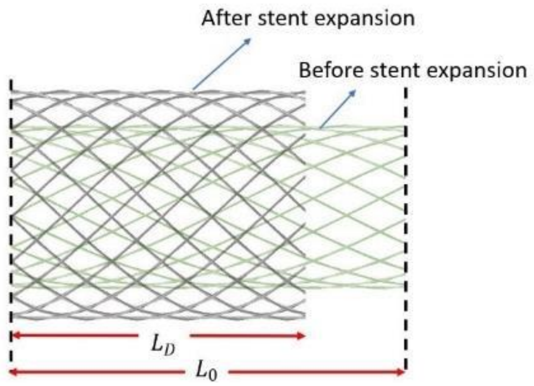

Figure 23. Schematic of the foreshortening effect before and after the SX stent deployment, adapted from [102].

Radial Elastic recoiling

After releasing the stent from the catheter, it fully expands until it touches the vessel wall. Therefore, the pressure exerted by the vessel wall opposes the expansion of the stent, resulting in a reduction of the stent's diameter upon opening, as depicted in Figure 24. The radial elastic recoil [112,113], quantifies this new equilibrium condition, which could also occur gradually after an extended period of time due to the viscoelastic behavior of the vessel. Radial elastic recoil is influenced by different factors, including the design and material composition of the stent and its formula, in accordance to technical literature, is reported in Equation 28, R_0 is the radial diameter of the stent when it reaches full expansion immediately after deployment, and R_f represents the final diameter of the stent in the last equilibrium position. The elastic recoil is strictly linked to radial stiffness. After deployment, if the stent shows high elastic recoil, it may lack the ability to adequately support blood vessels and maintain patency. Target value tends to be zero or the lowest possible.

$$R_{recoil} = \frac{R_0 - R_f}{R_0} \qquad \text{Equation 28}$$

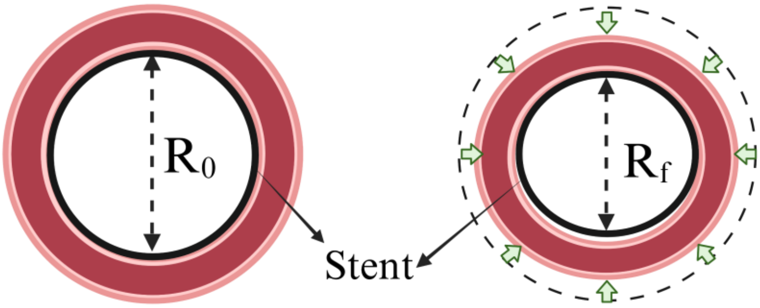

Figure 24. Schematic representation of stent recoil, stent after deployment and full expansion (a) and stent after recoiling (b) due to vessel elastic springback.

Dogboning

During vascular expansion, the stent undergoes non-uniform expansion which could cause vascular wall problems. This uneven deformation typically leads to the two ends of the stent being more open than the center, giving it a shape resembling a "dog bone" as shown in Figure 25. This phenomenon happens since the proximal and the distal parts of the stent are less stiff than the central part of it. This occurs since the central part of the stent is supported by both sides, providing stability and rigidity, however, the two ends of the stent are only attached from one side, making them less supported and more prone to widening. Dogboning (D_b) can be calculated through Equation 29 where D_{distal} is the maximum diameter of the stent at both distal or proximal part of it, while $D_{central}$ corresponds to the minimum diameter at the middle of the stent [114]. Uneven deformation at the distal ends results in substantial plastic deformation in those areas, leading to potential stent fracture and causing damage to the vessel at the stent edges, which in turn, contributes to restenosis [110]. Minimizing dogboning is essential to ensure uniform expansion across the entire stent. Target value is zero or negative.

$$D_b = \frac{D_{distal} - D_{central}}{D_{distal}} \qquad \text{Equation 29}$$

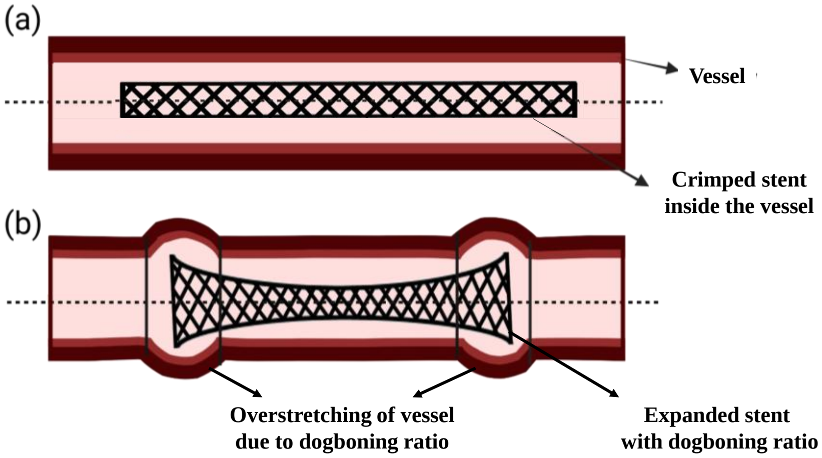

Figure 25. Stent dog-boning mechanics schematic, adapted from [115]. (a) Crimped stent inside the vessel, and (b) expansion of the stent with an out of scale, which causes the artery to overstretch.

Stiffness

Stents are designed specifically with the aim of upholding the patency of lumens (blood vessels, bile ducts, urethra) and they experience a combination of mechanical actions that twist, compress, elongate and bend them [116]. Femoro-popliteal district stents are mechanically the most stressed class of stents because femoro-popliteal district arteries (FPAs) twist and bend with almost any activity undertaken by the patient, including basic functions such as walking and sitting [117]. Due to the complexity and variety in design geometries of stents, SX NiTi stents of the same diameter and length can show very different stiffnesses, as evidenced by a number of studies which performed *in-vitro* (benchtop) tests to obtain the stiffnesses of various stent designs [117–119].

Figure 26 depicts the main forces and moments acting on the stent after its deployment in the blood vessel, namely the axial force N, the bending moment M, the torque T and the radial pressure Δp. Therefore, four different stiffnesses (and consequently four compliances) can be envisioned: axial, bending, torsional and radial stiffness.

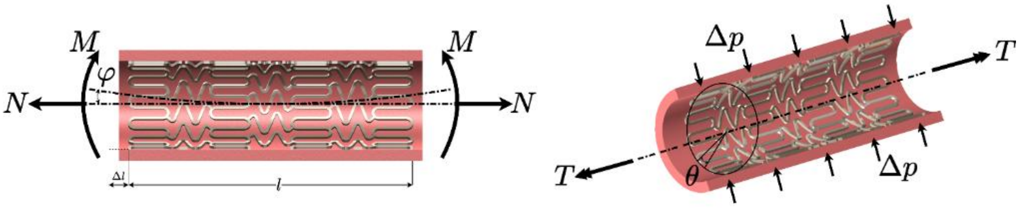

Figure 26. Forces and moments acting on the stent.

Axial stiffness. Axial stiffness, k_N and its inverse, axial compliance, c_N, is defined according to Equation 30 where N is the axial force acting on the stent, Δl is the elongation (when positive) or shortening (when negative) of the stent in the axial direction, E is the Young modulus of the material (NiTi in the austenitic phase in this case), A is the equivalent cross-section of the stent and l is the length of the stent after its deployment in the blood vessel [120]. The experimental test rig is reported in Figure 27 with tensile (Figure 27(a)), and compressive(Figure 27(b)) loading position.

$$k_N = \frac{N}{\Delta l} = \frac{\mathrm{EA}}{\mathrm{l}} = \frac{1}{\mathrm{c_N}} \qquad \text{Equation 30}$$

Bending stiffness. To assess stent bending stiffness, a common method used is the three-point bending test [121], in which the stent is bent under controlled conditions to evaluate its ability to flex without permanent deformation, usually under a three-point bending condition as showed in Figure 27(c-d). Bending stiffness, k_M, and its inverse, bending compliance, c_M, is defined according to Equation 31 where M is the bending moment acting on the stent, φ is the bending angle of the stent, E is the Young modulus of the material (NiTi in the austenitic phase for this case), J_n is the second moment of the cross-sectional area of the stent around the x-axis, l is the length of the stent after its deployment in the blood vessel [120,122].

$$k_M = \frac{M}{\varphi} = \frac{\mathrm{EJ_n}}{\mathrm{l}} = \frac{1}{\mathrm{c_M}} \qquad \text{Equation 31}$$

Torsional stiffness. Torsional stiffness is an important factor mostly for stents designed for FPA stenoses [74]. Torsional *in-vitro* tests can be performed restricting axial deformations and executing tests with different angles or angular displacement rotations in both clockwise and counterclockwise directions with a chosen speed [118], as shown in Figure 27(e-f). Bending stiffness, k_T and its inverse, torsional compliance, c_T are defined according to Equation 32 where T is the torque acting on the stent along the z-axis (namely the stent axis, which I assume is the same as the vessel axis), θ is the torsion angle, G is the shear modulus of the material (NiTi in the austenitic phase), J_O is polar moment of inertia of the stent, l is the length of the stent after its deployment in the blood vessel [120].

$$\mathrm{k_T} = \frac{\mathrm{T}}{\theta} = \frac{\mathrm{GJ_O}}{\mathrm{l}} = \frac{1}{\mathrm{c_T}} \qquad \text{Equation 32}$$

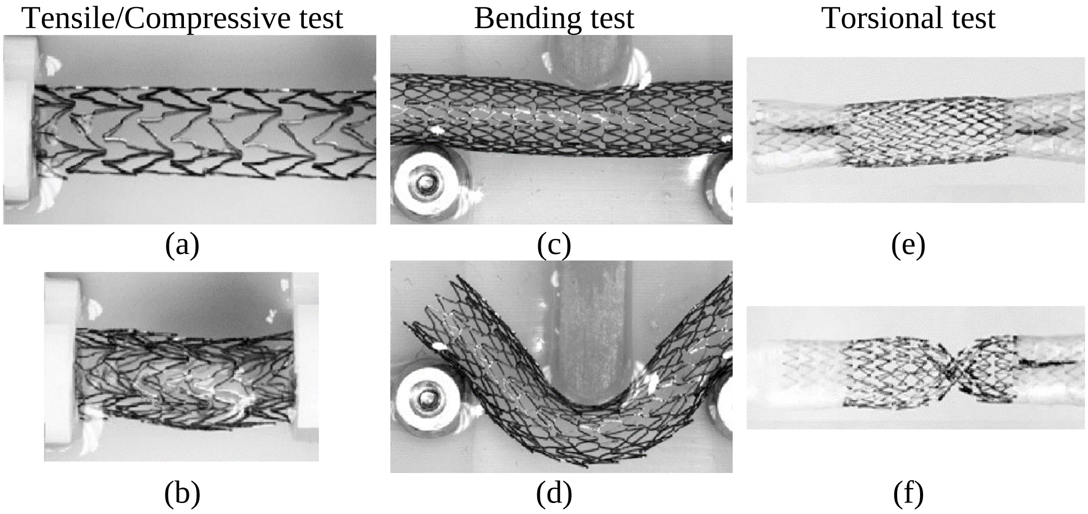

Figure 27. Stent testing according to [118]. Axial test: (a) tensile load and (b) compressive load. Bending test: (c) neutral position and (d) load pin displacement applied to the middle of the span. Torsional test: (e) neutral position and (f) 90°/cm torsion.

Radial stiffness. Radial stiffness defines how the stent responds to changes in diameter with respect to external pressures. It is a measure of the ability of the stent to provide radial structural support against recoil within a blood vessel [98] and it is quantified by the variation of pressure over the diametral hoop strain as expressed in Equation 33. In accordance with [123–125], Δp is the pressure the vessel exerts on the stent, ε_{hoop} is the hoop strain, d is the initial diameter of the stent, Δd is the diameter variation of the stent and c_r is the radial compliance of the stent [126].

$$\mathrm{k_r} = \frac{\Delta \mathrm{p}}{\varepsilon_{\mathrm{hoop}}} = \frac{\Delta \mathrm{p} \cdot \mathrm{d}}{\Delta \mathrm{d}} = \frac{1}{\mathrm{c_r}} \qquad \text{Equation 33}$$

Usually, radial stiffnesses are calculated as slopes of linear regression fits of loading curves obtained through experimental data [118]. The radial pressure and radial stiffness are strongly interdependent since this relationship relies not only on the absolute value of the pressure but also on the slope of the pressure-hoop strain curve. To demonstrate this, in Figure 28, a comparison between two distinct stent designs is illustrated; curve A and curve B represent the mechanical behaviors of these designs under different radial pressures but the same diametral hoop strains. Curve B exhibits higher radial pressure but a slight slope, while curve A has lower maximum pressure at a given strain with a steeper slope. Despite curve A's lower maximum pressure, its steeper slope signifies a greater increase in pressure per change in diameter, suggesting higher radial stiffness than curve B ($k_{r,A} > k_{r,B}$). This comparison highlights that while the value of radial pressure often aligns with radial stiffness, the slope of the pressure-diametral hoop strain relationship profoundly influences the stent's overall mechanical behavior and greater maximum radial pressure does not necessarily translate to greater radial stiffness in stents. This behavior depends both on geometry and on the material model, which follows a superelastic curve.

While high radial stiffness is essential to prevent arterial collapse by enhancing the ability of the stent to restore blood flow and prevent it from recoiling [118,127], low radial stiffness is important for minimizing stress on vessel walls and reducing the risk of inflammation and restenosis. Therefore, achieving an optimal trade-off between high and low values of radial stiffness is key in stent design to ensure both structural support and vessel wall health.

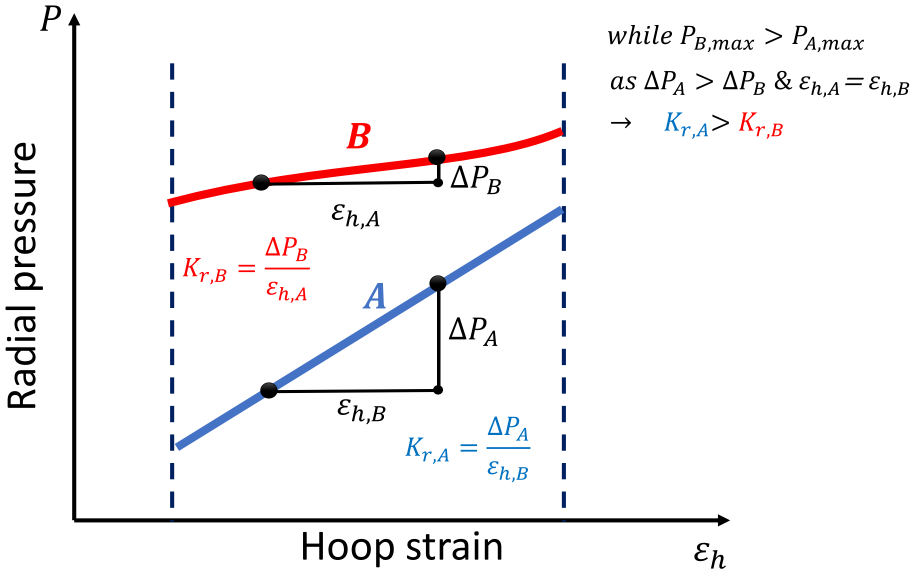

Figure 28. Comparison of radial pressure-hoop strain, curve A with low pressure and high stiffness and curve B with low stiffness and high pressure.

Oversizing

A SX stent is often chosen with a diameter slightly larger than the vessel's diameter to serve its function effectively within a blood vessel and prevent migration [128]. The ratio between the initial stent diameter (D_s) and the vessel inner diameter (D_v) is called oversizing (OS), which can be calculated from Equation 34. Clinical observations and studies suggest that for SX NiTi stents, oversizing ratios in the range of 1.1 to 1.4 lead to improved lumen gain, reduced incomplete stent apposition, and Favorable long-term fatigue performance [128–131]. On the other hand, an increase in the oversizing ratio beyond this ideal range ($OS > 1.4$) can result in high radial forces, potentially causing damage to the artery wall and compromising the stent's long-term efficacy including collapse.

$$OS = \frac{D_s}{D_v} \qquad \text{Equation 34}$$

Radial forces

Radial forces, whether exerted on the stent or by the stent onto the vessel wall, are critical to the design and function of stents, making it essential to understand their significance for optimizing stent design and deployment strategies. In the following section, the significance of three main radial forces listed below and illustrated in Figure 29(a-c), is described:

- Radial Resistive Force (RRF)
- Chronic Outward Force (COF)
- Crush Resistance (CR)

RRF. As already mentioned, when a SX stent is designed, it's often manufactured in a larger size than vessel diameter to serve its function effectively within a blood vessel (point 1in Figure 29(d)). However, to deliver it to the target location within the vessel, it needs to be crimped to a smaller size to fit into a delivery catheter (point 2 in Figure 29(d)). The force required to achieve this compression is called the radial resistive force (RRF). RRF describes the force that is required to compress the stent radially during circumferential loading (crimping) to fit the catheter. To maintain the stent diameter and reduce the risk of restenosis, a stent must have enough RRF [86,87]. However, the precise amount of RRF needed in-vivo, is still debated [48] since it depends on the stent-wall interaction.

COF. When the stent is removed from the catheter and inserted into the vessel, it expands, as shown by Figure 29(d) from point 2 until the expansion is stopped by the contact to the vessel wall (point 3 in Figure 29(d)). At this point the stent and the vessel reach a stress equilibrium, and the stent cannot expand anymore. Therefore, it continues to exert a continuous outward force onto the vessel wall known as chronic outward force (COF). The COF is the force that the stent exerts on the vessel wall when it undergoes expansion (during unloading) [132]. Although low COF on the vessel ensures vessel patency and prevents stent migration and restenosis [133], excessive COF has the potential to cause avoidable damage to the surrounding tissue [109,118].

Elastic hysteresis of NiTi allows for a continuous COF on the vessel wall which remains very low even when subjected to significant deformations. In contrast, the stent's ability to resist compression, which is represented by RRF, increases rapidly as the stent deforms until it reaches a plateau stress level (as shown in Figure 29(d), from point 3 to point 4). This dynamic interplay between COF and RRF showcases NiTi's capability to provide effective support while minimizing the risk of vessel damage, making it a valuable material for stent design and deployment. Generally, stent designers attempt for the maximum achievable RRF while keeping the COF to a minimum [100]. Both characteristics of RRF and COF were analyzed using the radial force-tester method [121].

CR. The last parameter has a simpler definition: Crush-resistance (CR) is the force required to compress the stent in one radial direction [133] as shown in Figure 29(c). To measure CR, the stent is compressed between parallel plates from its expanded state up to a 50% diameter reduction [134]. The main issue related to CR is that insufficient CR raises the risk of restenosis [135].

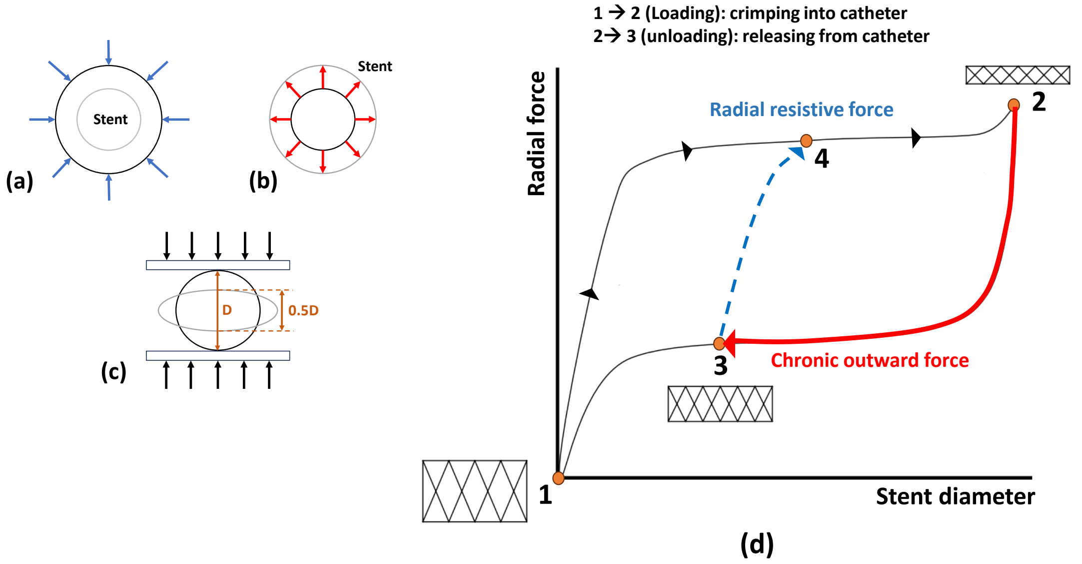

Figure 29. Schematic illustration, adapted from [9], of the compression mechanism during the testing of (a) RRF, (b) COF, (c) CR force, and (d) RRF and COF as a function of the superelastic hysteresis loop, adapted from [136].

The experimental setup required to estimate the radial force is not trivial. A couple of examples are reported in Figure 30, where a special machine is exploited in Figure 30(a) or a test rig with rollers and a thin aluminum sheet is used to apply a quasi-uniform compressive pressure on the stent Figure 30(b).

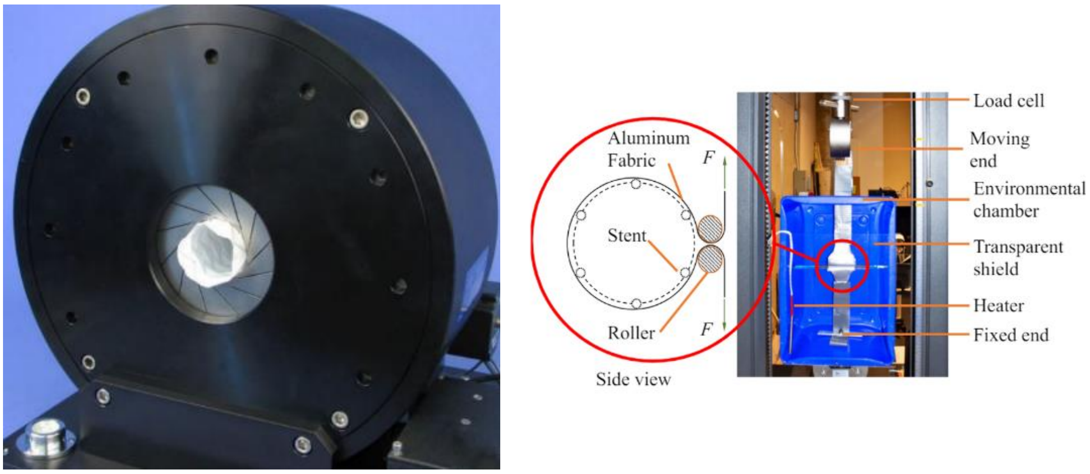

Figure 30. Radial force measurement of a stent: (a) radial RX-650 with several blades to radially compress the stent uniformly [133], (b) a stent wrapped in a sheet in a circular configuration attached to tensile machine grippers radially compressing the stent [123].

Fatigue life of the stents

Once implanted, stents are subjected to continuous loadings due to pulsatile cardiac pressure within the bloodstream. Furthermore, depending on the region in which they are implanted, they can be subjected to bending, compression, and torsion. For example, several *in-vivo* tests on cadavers showed that during hip flexion and knee bending, the superficial femoral artery (SFA) and the popliteal arteries are subjected to axial compression and bending [137,138]. Most of the bending occurs behind the knee, but some bending also occurs on the straight tract of the SFA. Over time, the continuous pulsatile and mechanical stresses can induce fractures in stents. In regions such as the FPA bending occurs in the order of magnitude of 10^6 cycles per year [96]. According to 1995 FDA guidelines [92,98] when implanted in SFAs, stents would need to be certified for at least 400 million cycles without a single fracture. Fatigue of stents, being a very complex subject, is still an open problem for NiTi, although several works exist on assessing the fatigue behavior of stents [92,96,139] through finite element analysis (FEA) in order to predict their *in-vivo* fatigue resistance.

Although changing the design of the stent can affect its fatigue life, most studies are devoted to improving the fatigue life of the base material [92]. For metals such as steel or linear elastic materials in general, a stress-based approach [82] such as Wohler curves is used, but for NiTi and superelastic materials in general, a strain-based approach is preferred in order to consider the superelastic behavior of the material.

Therefore, a possible factor of safety (FOS) definition for a NiTi stent is shown in Equation 35, where ε is the critical strain amplitude of the material and ε_a is the strain amplitude withstood by the stent during its life. [92,140]. The critical strain amplitude experimentally measured for NiTi is around 0.4-0.55% [92,141] for mean strains below 3%, which is a compatible range for stent devices. Fatigue is also strongly dependent on the surface finish of stents which explains the very precise and careful polishing and etching of the stent which reduces the roughness of metal and improves the fatigue performance.

$$FOS = \frac{\varepsilon}{\varepsilon_a} \qquad \text{Equation 35}$$

Wall shear stress

This last figure of merit is the only one related to the hemodynamic and not to the mechanical properties of the device, which is very important since it affects the stent performance. Generally, a vessel wall is subjected to two main forces. First, the blood within the vessel exerts pressure outward onto the wall of the vessel known as blood pressure, leading to circumferential stress. Secondly, as blood flows through the vessel, it creates a frictional force along the inner surface of the vessel. This frictional force, generated by the blood flowing in the vessel wall in tangential direction, is called wall shear stress (WSS) [142,143]. The shear stress levels vary within different segments of the circulatory system. In the venous system, shear stress typically ranges from 0.1 to 0.6 Pa, whereas in the arterial vascular network, it generally varies from 1 to 7 Pa [144]. In context of stent implantation, the insertion of the stent in a blood vessel can lead to additional stress on the vessel wall [143]. This additional stress leads to changes in the normal blood flow and local shear distribution which in turn causes implications for the overall hemodynamic performance of the vessel and may influence factors such as neointimal proliferation and restenosis.

When a stent is deployed, it alters the natural geometry of the artery, leading to changes in blood flow patterns. Specifically, the increased curvature at the stent's edges can result in regions where blood flow becomes turbulent or oscillatory [145]. Furthermore, the increase in diameter of the stent after deployment may reduce blood velocity, potentially exacerbating adverse hemodynamic conditions that contribute to restenosis [146]. Research has shown that the design parameters of the stent, particularly the number and dimensions of struts, surface topology and the stent-to-artery deployment diameter significantly influence WSS and clinical outcomes such as neointimal hyperplasia and restenosis [147–149]. For instance, a higher stent-to-artery deployment ratio can increase exposure to WSS compared to a lower ratio [147]. Moreover, increasing the height and number of struts can generate disturbed WSS zones, while reducing strut thickness can decrease areas subjected to WSS [147]. Thinner struts generally lead to improved re-endothelialization. Research indicates that thicker struts create more disturbed flow patterns and higher shear stress levels, which can delay endothelial healing and increase the risk of thrombosis and restenosis [150,151]. For instance, a study [145] highlighted that thicker bioresorbable stents resulted in delayed re-endothelialization compared to thinner drug-eluting stents.

Hemodynamic performance of stents is often evaluated by a WSS index, quantifying the impact of in-stent restenosis [112,152]. This index is calculated through Equation 10, where n is the normal vector to the vessel surface and $\overrightarrow{\overrightarrow{\tau_{ij}}}$ is the fluid viscous stress tensor [153]. An ideal stent design should aim to achieve superior biological hemodynamic performance with minimal changes to laminar blood flow properties and WSS distributions.

$$\tau_w = n \cdot \overrightarrow{\overrightarrow{\tau_{ij}}} \qquad \text{Equation 36}$$

General discussion on the figures of merit

The effectiveness of SX NiTi stents is dependent on several key mechanical properties and performance metrics, as discussed in this section. These figures of merit are crucial for evaluating stent functionality and durability within the vessels. To facilitate stent design and optimization, it is essential to establish desired optimal values (or ranges) for each of these properties to serve as benchmarks for stent designers and manufacturers, guiding them towards achieving optimal performance while minimizing potential complications associated with stent implantation. Table 4 provides a summary of the desired values of each parameter, offering valuable insights for enhancing the efficacy and reliability of SX NiTi stents in clinical settings. Based on Table 4, an ideal stent should exhibit zero foreshortening, dogboning, and elastic recoil, although achieving this is challenging, particularly concerning dogboning and recoiling parameters. Yet, advancements in stent design offer promising strategies to mitigate these issues. In minimizing foreshortening, research has shown promising results, for instance P.K.M. Prithipaul et al. achieved zero foreshortening with some hybrid auxetic cell design in their study [112]. Addressing dogboning, a balance in the radial stiffness of the middle and end parts of the stents should be adjusted, which can be done either by increasing the thickness of the struts on the ends of the stents [154,155] or by adding closed-cell segments to those parts of the stent to make them stiffer. To prevent recoiling, the higher the radial stiffness of the stent, the more resistant it can be to the pressures from the vessel wall and the less recoiling. Therefore, increasing radial stiffness can effectively prevent stent recoil. On the other hand, excessive radial stiffness can reduce stent compliance and apply high radial pressure to the vessel wall, resulting in damage to the vessel and therefore causing ISR. Therefore, based on the amount of pressure and the radial force that the vessel can withstand, which strongly depends on the vessel positions, it is possible to increase the stiffness of the stent to a certain extent. Similarly, the RRF range should be carefully selected to push away the plaques and keep the vessel open effectively without causing vessel damage. Oversizing can have a significant effect on the amount of RRF. Higher oversizing leads to higher RRF. Typical endovascular procedures suggest to apply the slightly larger stent available, but applying a 10 mm stent on a 9 mm vessel causes an RRF and a COF lower than 10% compared applying a 6 mm stent on a 5 mm vessel, according to Equation 34. Since commercial stents are commonly shelf devices with predefined dimensions it is hard to prescribe an optimal solution. In addition, an ideal stent should maintain normal blood flow. In other words, it should not increase further WSS on the vessel wall. Despite the inevitable changes in WSS caused by stent implantation, the design of the stent can be optimized to reduce its impact on WSS. By designing the stent with smooth edges and ensuring that struts are aligned as parallel as possible to the vessel direction, the likelihood of disturbing blood flow and increasing WSS is reduced [149]. In conclusion, optimizing the mechanical properties and performance metrics outlined in Table 4 is essential for enhancing the efficacy and reliability of SX NiTi stents.

Table 4. Desired values for SX NiTi stents.

Figures of merit (unit)	**Desired value**	**References**
Foreshortening (%)	Minimum the best	[79,80]
Radial elastic recoil (%)	Minimum the best	[112]
Dogboning (%)	Minimum the best	[110]
Radial stiffness (MPa)	Nominal the best	[118,127]
Axial stiffness (N/mm)	Minimum the best	[118]
Bending stiffness ($N \cdot mm/rad$)	Minimum the best	[80,118]
Torsional stiffness ($N \cdot mm/rad$)	Minimum the best	[118]
Oversizing (%)	$10\% < OS < 40\%$	[128–131]
RRF (N)	Nominal the best	[118]
COF (N)	Minimum the best	[100,118]
CR (N)	Maximum the best	[135]
Fatigue life (number of cycles)	Maximum the best	[92,124,156]
Wall shear stress (Pa)	Minimum the best	[143,146,157]

To summarize, thirteen figures of merit for describing SX NiTi endovascular stents were analyzed, qualitatively and, where possible, quantitatively. Specific quantitative ranges for each figure of merit were not provided, given the wide variety of regions in which endovascular stents can be deployed. Each of these districts requires the optimization of some specific characteristics of the stent (for example, a stent for the FPA requires greater bending compliance than a stent for the SFA). Only oversizing is given a more precise range of values, since a general trend of applicability was found in the stent applications guidelines [131].

3.1.5 Classification of stents based on geometry

From the point of view of the shape, stents are grouped into coil, slotted tube, and modular designs [158]. Coil stents are constructed using wires that are shaped and arranged into a circular coil configuration to form the stent scaffold. In the case of slotted tube stents, a metal tube acts as the stent's basis material, and a specific design or pattern is generated using laser cutting [102,104]. The modular stent's construction involves interconnected individual modules, allowing for a more customizable and adaptable structure. This last design is intended to overcome specific challenges present in traditional stent designs. For instance, it addresses the poor radial force and higher restenosis rates associated with coil stents, as well as the drawbacks of slotted tube stents, which may have low bending compliance and deliverability. The modular design provides a balance between the bending compliance of coils and the radial strength of slotted-tube designs [81]. In Figure 31 a schematic classification of stents alongside images illustrating representative examples of each stent type are presented.

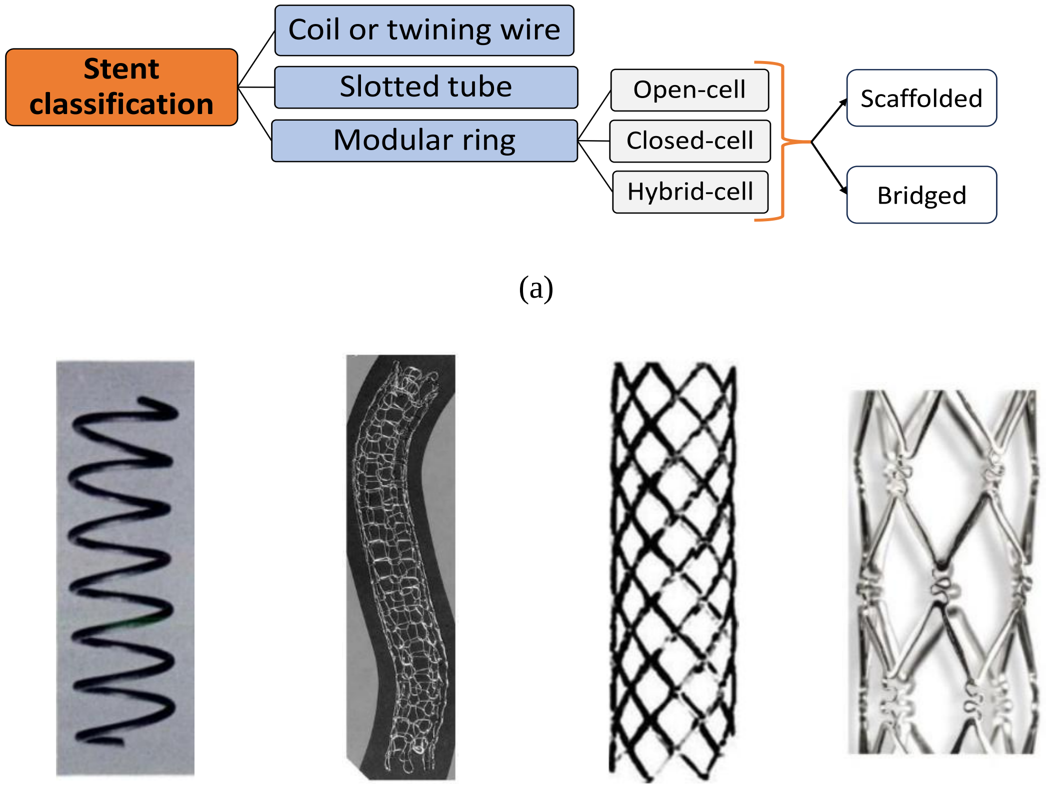

(a)

(b) (c) (d) (e)

Figure 31. (a) Schematic classification of stents based on the geometry, (b) NiTi coil wire stent by Dotter et al. [77], (c) Strecker stent made of knitted tantalum wire [159], (d) slotted tube structure of Palmaz-Schatz stent [122], (e) a modular ring with closed-cell design [160].

Modular ring stents are classified into three groups: closed-cell, open-cell, and hybrid-cell. Closed-cell designs (Figure 32(a)) are characterized by interconnected stent strut with smaller free cell area, while the open-cell designs (shown in Figure 32(b)) have larger free cell area with fewer interconnections [158,161]. Additionally, there are also hybrid-cell configurations that combine these first two groups to gain the benefits of both designs [162], mostly with the same design at proximal and distal segments and a central different cell design (Figure 32(c-d)). Hybrid stents, such as Scitech-Solaris, have an open-cell design in the central part, for improving the bending compliance of the stent, and a closed-cell design at the two ends to adjust the stiffness in the distal parts (as depicted in Figure 32(c)). Other hybrid stents such as Cristallo

Ideale, a Medtronic carotid stent [163], combine open-cell design at the proximal and distal sections (as shown inFigure 32(d)) enhancing conformability, flexibility and reducing radial force in the healthy vessel segments. The closed-cell design in the central part secures the appropriately high scaffolding at the lesion site preventing plaque prolapse.

More gaps between the cells in an open-cell design makes it more compliant compared to a closed-cell design, which is particularly advantageous for complex arteries with angular or twisted anatomies [159]. On the other hand, as the closed-cell design has more interconnections, it is stiffer, offering better plaque coverage and structural support [162,164]. However, this increased stiffness comes with potential drawbacks such as higher risk of restenosis post-stenting. Another difference regarding hemodynamics properties is that a closed-cell stent allows for a higher blood flow velocity through the stented region compared to an open-cell stent structure [165]. A summary of the differences between open-cell and closed-cell stent designs is provided in Table 5.

The last geometrical considerations regard the scaffolded or bridged structures. The former are characterized by the direct connection and arrangement of representative unit cells (RUC) as in Figure 33(a). On the other hand, bridged structures, as depicted in Figure 33b are composed of bridge/connector and rings. In this design, rings play a pivotal role in radially expanding and providing support to the blood vessel, while bridges/connectors connect the rings axially, contributing to the stent's axial stiffness [166]. Each ring is typically composed of circumferential struts as shown in Figure 33(c).

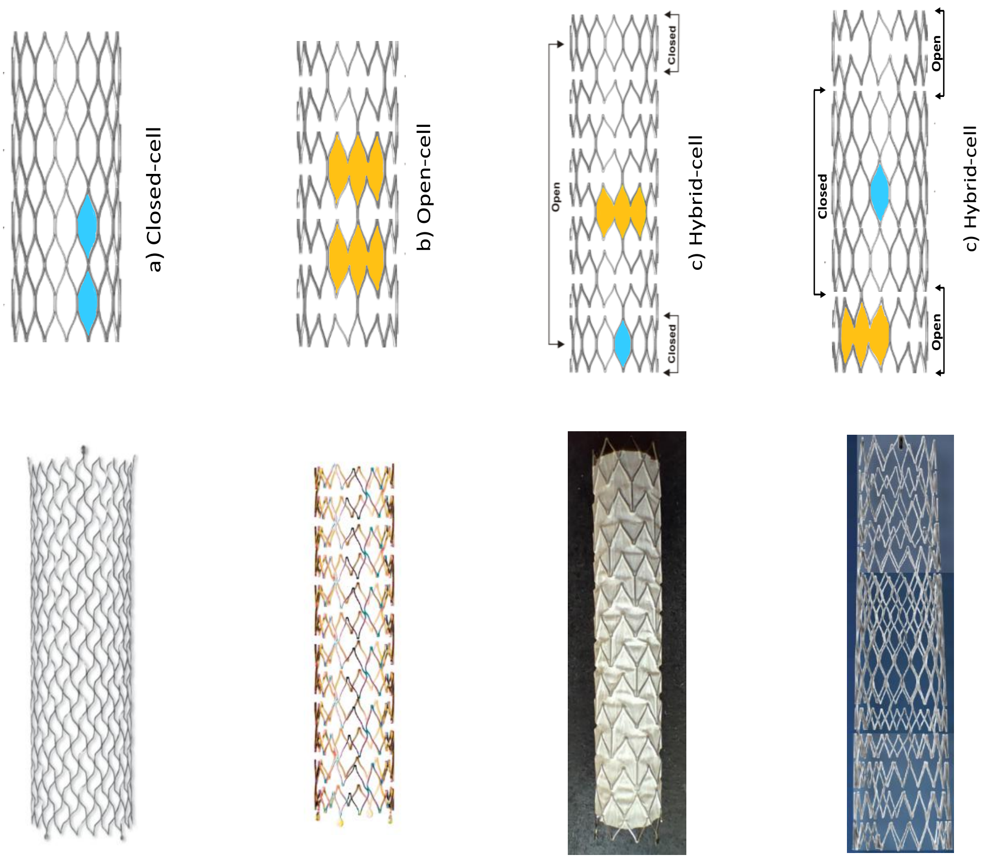

(a) (b) (c) (d)

Figure 32. Modular stent arrangements, adapted from [167], with corresponding available stents: (a) closed-cell, Optimed Sinus-XL [168], (b) open-cell, Biotronik Pulsar [163,169], and (c-d) hybrid-cell configurations, Scitech Solaris, Medtronic Cristallo Ideale [163].

Table 5. Comparison of parameters between open-cell and closed-cell stent designs.

	Open-cell stents	**Closed-cell stents**
Compliance	↑	↓
Radial stiffness	↓	↑
Applicability for complex vessel	↑	↓
Plaque coverage	↓	↑
Higher risk of restenosis	↓	↑
Velocity of blood flow after stenting	↓	↑

Understanding the impact of strut and bridge topology on stent performance is one of the crucial factors for stent design. Researchers commonly concentrate on optimizing stent performance by investigating factors such as the shape, arrangement, and number of bridges, along with the width, thickness, and length of the struts, so providing insight on this factor is helpful, hence the compact form shown in Table 6.

Generally, a decrease in the number of bridges/connectors between struts tends to enhance the bending compliance of the stent [170]. Moreover, according to some clinical studies, stents with the higher thickness of the strut are associated with the higher risk of restenosis in the vessel [171–173]. Additionally, aligning the struts parallel to the blood flow helps in maintaining a more uniform distribution of WSS within the vessel [149]. While different strut dimensions may imply different impacts on the stent's performance such as stiffness, radial forces, etc., they do not affect the foreshortening, as the foreshortening is dependent on the cell geometry and affected by the angle between the stent's strut and the axial direction of the stent [174].

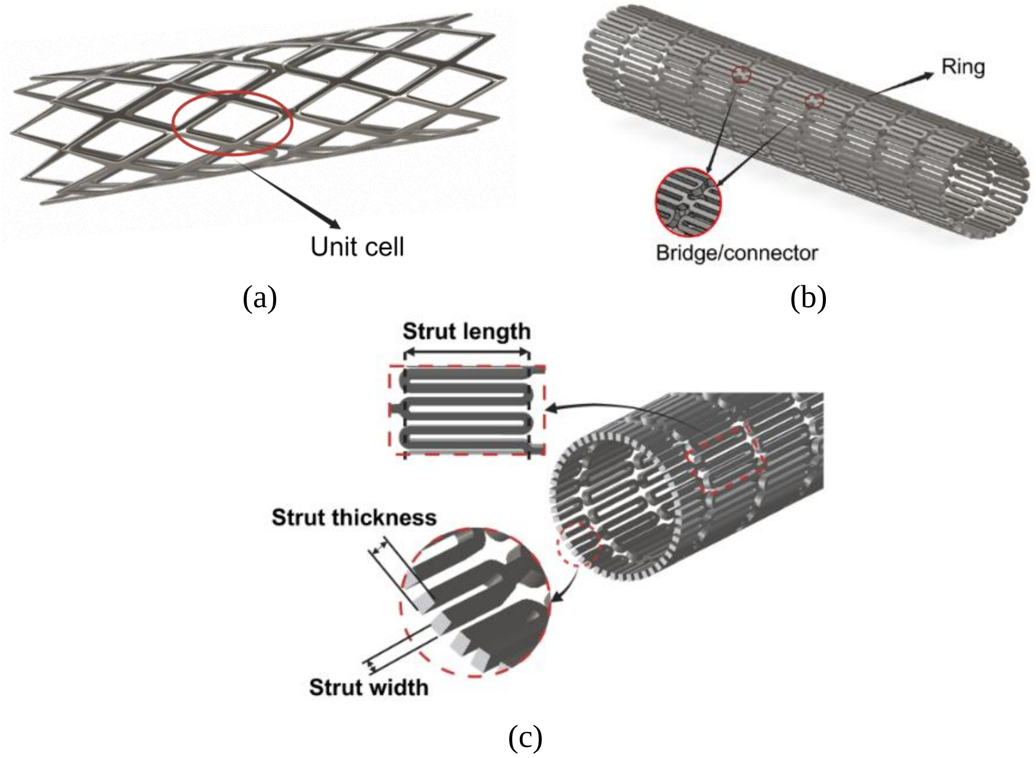

(a) (b)

(c)

Figure 33. Two types of modular stents: (a) scaffolded structure [175], (b) bridged structure [176]. (c) Cross-sectional view of a segment of the stent illustrating strut dimensions.

Table 6. The effects of strut dimensions on the figure of merits of stents.

	Strut dimensions			**References**	**Note**
	↑ Width	**↑ Thickness**	**↑ Length**		
Foreshortening	-	↓	-	[174]	Depending on the cell geometry: considering same displacement in radial direction
Recoiling	↓	↓	↑	[154]	Stiffer stents cause lower recoiling
Dogboning	↓	↓	-	[154,155]	Increasing width and thickness of the strut selectively at both stent ends reduces dogboning
Radial stiffness	↑	↑	↑	[177]	
Axial, torsional, and bending stiffness	↑	↑	↓	[170,178]	
Oversizing	-	-	-	[128]	Depends on the stent/vessel diameter
RRF, COF, CR	↑	↑	↓	[113,178]	
Fatigue life (isostress)	↑	↑	↓	[177]	Mechanical tests at same load
Fatigue life (isostrain)	↓	↓	↑	[178]	Mechanical tests at same displacement
Wall shear stress	↑	↑	-	[147]	Larger struts cause more flow turbulence

3.1.6 Stent manufacturing technique

Stents are not of simple manufacture; their strut thickness is of the order of magnitude of hundreds of microns; therefore, they need careful manufacturing and strict tolerances. Moreover, being medical devices, they need to be compliant with strict guidelines and rules, for example in Europe they need to have the CE (Conformité Européenne) mark and in the United States the FDA (Food and Drug Administration) approval is required.

The manufacturing techniques for stents can generally be categorized into three primary methods: braiding technique, microinjection molding, laser cutting, and recently AM [81]. Generally, stents are not immediately usable after the manufacturing process because their surface quality must be improved to increase the stent’s fatigue life, to grant its biocompatibility, and to diminish abrasion problems that could cause vessel injuries; therefore, stents usually undergo a series of post-processing steps after fabrication.

Each manufacturing method offers distinct advantages and challenges, depending on the specific design requirements and applications of the stent. In the following sections, each of these techniques will be examined in detail. A representative stent design manufactured using each method will be analyzed, highlighting the manufacturing process, mechanical performance, and suitability for specific biomedical applications.

3.2 SELF-EXPANDING NITI STENTS: DESIGN AND PERFORMANCE BASED ON SUPERELASTIC BEHAVIOR

3.2.1 Braiding technique

Figure 34 shows an image extracted from a patent for the braiding technique of stents [179]. The braiding technique consists of winding wires (for example six interwoven NiTi wires in the case of Abbott Supera [180]) around the carrier, and then the wires are woven along the axis of rotation of the stent in order to build it [79,81].

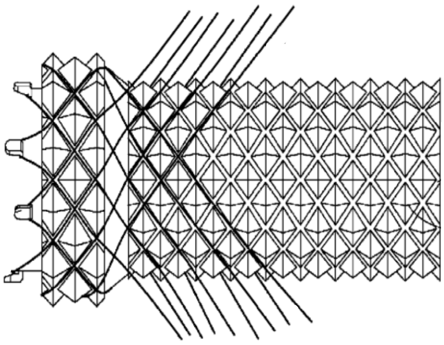

Figure 34. Braiding technique [179].

Braided stents have a simple shape, consist of a series of interwoven wires that can expand and contract like a spring which can be categorized into two types: open-ends and looped-ends. The term "open ends" refers to the design where the ends of the wires are left exposed. In contrast, looped-ends braided stents have their wire ends looped back and secure.

Braided SX stents offer several advantages in the treatment of vascular disease including very high torsional stiffness, and adaptability to complex vessel shapes, allowing them to reduce the risk of injury or complications. Their kink resistance helps to prevent collapse or damage during deployment, and their flexible design causes less damage to the vessel wall, reducing the risk of restenosis or thrombosis [181–187]. They do not buckle even under high axial compression [118].

Braided stents also have some limitations that need to be addressed. One critical issue is the friction between the interwoven wires in these stents, which can affect their mechanical performance. The slippage and sliding between the braided wires, driven by friction, results in a large alteration in the braided angle during deformation. This friction-induced, wire-on-wire displacement can degrade some stent properties such as conformability, foreshortening, and radial stiffness [188]. Interwoven friction also has been reported to have an influence on the CR of stents, while the radial force is only slightly affected. One of the main drawbacks of braided stents is their lower radial stiffness when compared to laser-cut or welded stents [189,190]. This limitation can impact on the stent's ability to effectively scaffold and keep the vessel open long-term, increasing the risk of recoiling and therefore restenosis. In addition, braided stents often exhibit substantial foreshortening compared to other designs [191,192], which may result in insufficient covering of the target lesion and may also result in partial wall contact [193].

In addition to the importance of the materials used to manufacture stents, evaluating the structure and geometry of stents is also crucial. A mathematical model of an open-ends self-expanding braided stent was proposed by [194] to describe both mechanical and geometrical properties of the stent and validated through experimental tests. Later, a study by [195] investigated whether the suggested model can be used to predict the mechanical behavior of looped-ends braided stent designs. There are several factors that can be considered when optimizing stents to improve their performance, such as the material used, the geometry design of the stent, the size and shape of the cells, and the coating applied to the stent. [196] used an optimization technique based on the Response Surface Method (RSM) and the Sequential Quadratic Programming (SQP) algorithm to enhance the fatigue life of a SX NiTi stent. Findings indicated that optimizing the strut length and cross-section will enhance the stent’s fatigue resistance. Moreover, [197] proposed a shape optimization framework using a finite element method (FEM) toolkit to improve the compression effect of biodegradable magnesium alloy stents (BMgS). In addition to an improvement in radial strength and a more uniform distribution of residual stress, their findings demonstrated a successful reduction in undesirable effects such as dog-boning and longitudinal foreshortening. [198] developed a novel optimization framework for minimizing strain in transcatheter aortic valve which showed a cost-effective solution for optimizing the TAV stent. In a subsequent study [199],they addressed challenges in transcatheter aortic valve implantation. Their optimized model design shows a significant improvement in all objective functions over the reference device and could enhance prosthesis performance and reduce malfunction risks. In [200] a new stent design framework was proposed to address the challenges posed by stent insertion and deployment uncertainties. The aim was to create a stent design that is less sensitive to uncertainties such as slight shifts in the stent's position on the balloon catheter during deployment and variations in vessel geometry and unknown biomechanical forces. To comprehend the relationships between the geometrical parameters of the stent and its biomechanical responses, surrogate mathematical models were developed. A Multi Objective Particle Swarm Optimization (MOPSO) algorithm was then employed to reduce dog-boning, foreshortening, elastic radial recoil, and stresses on the artery wall during stent deployment.

3.2.2 Aim of the research

In this work, I focus on an open-ends, braided SX stent. I aim to optimize the geometry design of an open-ends NiTi braided stent in order to enhance some of its mechanical properties. It is important to note that braided stents inherently exhibit good bending compliance due to their structure, and the use of nitinol further improves flexibility [189]. However, key disadvantages of braided stents include their relatively low radial stiffness [189,190] and the tendency for substantial foreshortening during deployment [191,192], which can lead to inaccurate placement and potential complications. Therefore, this approach specifically focused on the radial pressure stiffness and radial force of the braided stent, while minimizing the length variation during deployment, when it is fully deployed in the vessel. The novelty of this approach lies in the use of the Multi-Objective Particle Swarm Optimization (MOPSO) algorithm [201] to efficiently explore the design space and identify an optimal stent geometry.

In the first step, the mechanical properties of the NiTi braided stent structure are established through an analytical model proposed by [194]. Then, the mechanical behavior obtained using the analytical model and FE model was verified with the literature [195]. The MOPSO algorithm was then implemented to optimize the stent geometry and, finally, a radial compression test is simulated by means of a nonlinear

FE analysis of the stent in contact with the crimper, in order to confirm the algorithm's predictions.

3.2.3 Material selection

In this work, I considered, as previously done in [195], NiTi-based SX braided stent with a linear elastic behavior austenitic Young's modulus of 35.9 GPa, a yield stress of 489 MPa, a Poisson's ratio of 0.33, and austenite finish temperature (A_f) of 10℃ [202].

3.2.4 Cylindrical braided stents

The braided stent is a kind of SX design composed of two sets of interlacing wires twisted in a helical route along the stent axis in two opposite directions, clockwise and counterclockwise, as shown in Figure 35. The aim of the model is to estimate the geometry and mechanical characteristics of a self-expanding open-ended braided stent under the action of axial load F and radial pressure P. In the following section, the analytical formulae based on [194] to predict the mechanical and geometrical behavior of the braided stent under the axial load are summarized.

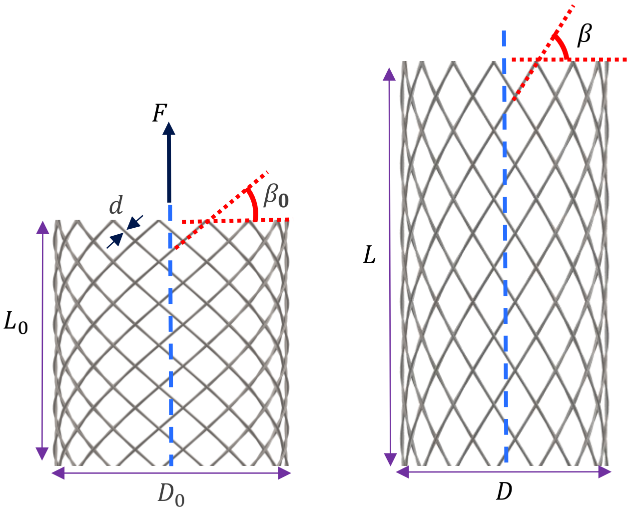

Figure 35. Stent elongation under axial loading F.

Stent geometry

The geometrical parameters of the braided stent (see Figure 35) are the initial stent diameter D_0, the initial length of the stent L_0, the diameter of a single wire d, the number of wires N, and the braided angle β_0. The braided angle is defined as the angle between any helix formed by the wire and the circumferential axis of the stent. When an axial load F is applied on the stent, the braided angle increases from β_0 to β. At the same time, the initial stent length, L0, extends to a new length L, while its initial diameter reduces to D. The initial pitch p_0 is the axial distance for one complete turn of the helix formed by a wire when the stent is in its initial configuration. Using these parameters, the initial pitch $p_0$and the number of coils c are given by the following equations [194].

$$p_0 = \pi D_0 tan\beta_0 \qquad \text{Equation 37}$$

$$c = {}^{L_0}/_{P_0} \qquad \text{Equation 38}$$

Based on the assumption that the length of the wires remains unchanged throughout deformation, the relationships between the ultimate length L and the diameter D and the braided angle are as follows:

$$D = \frac{D_0 cos\ (\beta)}{cos\ (\beta_0)} \qquad \text{Equation 39}$$

$$L = \frac{L_0 sin\ (\beta)}{sin\ (\beta_0)} \qquad \text{Equation 40}$$

Equation 41 also computes the minimum braided angle β_{min} associated with the maximum compressed configuration [203].

$$\beta_{min} = arctan\left(\frac{dN}{\pi D}\right) \qquad \text{Equation 41}$$

Mechanical properties

The stent model assumes that the behavior is similar to a collection of independent open-coiled helical springs. It is assumed that:

1) the stent undergoes only elastic deformation, and

2) the stent's ends are fixed against rotating around the longitudinal axis because of the friction between the wires at their crossing points.

Assuming the stent is subjected to a tension test, the axial force F exerted on the stent may be calculated using the following equation [203].

$$F = 2N\left[\frac{GI_P}{K_3}\left(\frac{2sin\ (\beta)}{K_3} - K_1\right) - \frac{EI.tan(\beta)}{K_3}\left(\frac{2cos\ (\beta)}{K_3} - K_2\right)\right]$$ Equation 42

Where K_1, K_2, and K_3 are constants as follows:

$$K_1 = \frac{sin\ (2\beta_0)}{D_0} \qquad K_2 = \frac{2cos^2(\beta_0)}{D_0} \qquad K_3 = \frac{D_0}{cos\ (\beta_0)}$$ Equation 43

$I$and I_P represent the moment of inertia and polar moment of inertia, respectively, and G and E are the shear modulus and Young's modulus respectively. The work done by load F is by definition dW=Fdδ. The same deflection δ can be generated by applying a uniformly distributed radial pressure P to an imaginary lateral surface πDL around the stent. The work done by the pressure P is equal to:

$$dW = P\pi DL\frac{dD}{2}$$ Equation 44

As P and F perform an equal amount of work, the pressure required to achieve the same deflection in a stent can be computed as follows:

$$P = \frac{2Fc}{DLtan(\beta)}$$ Equation 45

Therefore, the radial force F_R can be calculated as follows:

$$F_R = \frac{2\pi Fc}{tan\ (\beta)}$$ Equation 46

It is worth noting that the accuracy of all the aforementioned formulas was then verified by conducting a series of experiments by [194]. Their results showed good agreement between the theoretical predictions and corresponding experimental values for the stent diameter and axial force as a function of stent length. However, it was observed that the formula used to predict radial pressure as a function of stent diameter tends to overestimate the actual radial pressure when compared to the experimental data. This discrepancy is primarily attributed to the friction between the stent wires themselves and between the stent wires and the blocks used in the experimental setup, as noted by as noted by [194].To calculate the radial pressure stiffness K_P, the following equation is found in [203].

$$\begin{aligned} K_P &= \frac{dP}{dD} \\ &= \frac{2c}{K_3 \sin(\beta) \left(DLtan(\beta)\right)^2} \\ &\times \begin{bmatrix} 2DLN.\tan(\beta) \left(\frac{GI_p}{K_3} \left(\frac{2\cos(\beta)}{K_3} \right) - \frac{EI}{K_3} \left(\frac{2\cos(\beta)}{K_3} - \frac{K_2}{cos^2(\beta)} \right) \right) \\ -F \left(\frac{DL}{cos^2(\beta)} + K_3 \sin(\beta) \times (\pi c D - L.\tan(\beta)) \right) \end{bmatrix} \end{aligned}$$

Equation 47

Considering one of the open-coiled helical springs under the action of the load F, the bending and twisting moments (σ, τ) are given as follows.

$$\sigma = \frac{{}^{F}\!/_{N}\, sin(\beta).{}^{D}\!/_{2} \cdot d}{I}$$

$$\tau = \frac{{}^{F}\!/_{N}\, cos(\beta).{}^{D}\!/_{2} \cdot d}{I_p}$$

Equation 48

According to distortion energy, the equivalent Von Mises' stress σ_e is a function of shear stress τ and bending stress σ as follows:

$$\sigma_e = \sqrt{\sigma^2 + 3\tau^2} = \frac{8FD}{N\pi d^3} \sqrt{4sin^2\beta + 3cos^2\beta}$$

Equation 49

3.2.5 Optimization

An optimal stent, in addition to having sufficient flexibility (bending compliance) against pulses, should have considerable radial force and radial stiffness to maintain the vessels open [204]. In addition, foreshortening is an important parameter to consider when optimizing stents, since it can affect the performance and function of the stent. Foreshortening refers to the degree to which a stent is compressed along its longitudinal axis, which can occur during the deployment of the stent, as it expands radially. Although braided stents provide high coverage and flexibility, they significantly shorten after expansion, which leads to the stent being displaced from its position and decreasing the treatment's outcome [205]. Therefore, the geometrical design should be such that a change in the diameter value of the stent does not result in a substantial change in axial length.

Here, I used the MOPSO algorithm [201] in MATLAB to optimize the stent design. The MOPSO algorithm is a metaheuristic optimization algorithm that works by simulating a swarm of particles moving in a search space to find optimal solutions. While I acknowledge that optimizing a stent design ideally involves considering bending compliance as well, braided stents inherently exhibit good bending compliance due to their structure, and the use of NiTi which further improves their flexibility. The bending behavior of the same stent considered in this study was already analyzed by [206] where it is shown the relationship between bending stiffness and geometry of the stent. A spring-based mode shows that the stiffness increases proportionally to d4 and linearly to the number of wires. Therefore, the bending stiffness increases by $\frac{d_{opt}^4 N_{opt}}{d_{ref}^4 N_{ref}} - 1 = \frac{0.29^4 \cdot 16}{0.22^4 \cdot 30} - 1 = 61\%$. This amount seems large, but according to [206] is not problematic in terms of stress since the maximum stress is only 1.124MPa with a bending angle of 46°. The increase in stress therefore is proportional to the increase in stiffness and reaches 1.81 MPa, which seems acceptable. Therefore, in this study I primarily focused on maximizing the radial force, F_R and radial stiffness K_P of the stent while minimizing the length variation of the stent under axial loading L_{max}, to avoid foreshortening. In order to achieve an efficient stent, I used the MOPSO algorithm to explore three design variables, namely wire diameter (d), number of coils (N), and braided angle (β_0). The following ranges of d, N, β_0 are specified.

$$0.1\,mm \leq d \leq 0.30mm$$
$$10 \leq N \leq 40 \qquad \text{Equation 50}$$
$$\beta_{min} \leq \beta_0 \leq 70°$$

These ranges for N and β_0 were selected to encompass the common values for braided stents found in literature with slight extensions to cover broader possibilities. For instance, many papers report the number of wires in stents to be 12, 24, or 36 [207,208], so N was defined as a discrete variable restricted to an even value within the range of 10 to 40 to include all these possibilities. For the braided angle ($\beta 0$), observed values in the literature vary, with some reports indicating angles around 60° [209,210]. To accommodate these observations and explore further potential design optimizations, the range is extended up to 70° to explore additional design options. The range for the wire diameter d was set from 0.1 mm to 0.30 mm based on considering the reference design dimensions [195]. The reference design by [195] utilized a wire diameter of 0.22 mm, therefore, to explore a broader spectrum of design possibilities, the wire diameter range selected a slightly wider range. These ranges ensure a comprehensive exploration of potential stent designs while being grounded in observed practices.

Moreover, constraints are imposed on the maximum Von Mises stress and volume of the optimal designed stent in order to permit a fair comparison between the optimized design and the reference design [195] since the volume is the main parameter which drives the cost of the system.

$$\sigma_e \leq yield\ stress$$
$$Volume_{opt} \leq Volume_{ref} \qquad \text{Equation 51}$$

The flowchart of the MOPSO is reported in Figure 36.

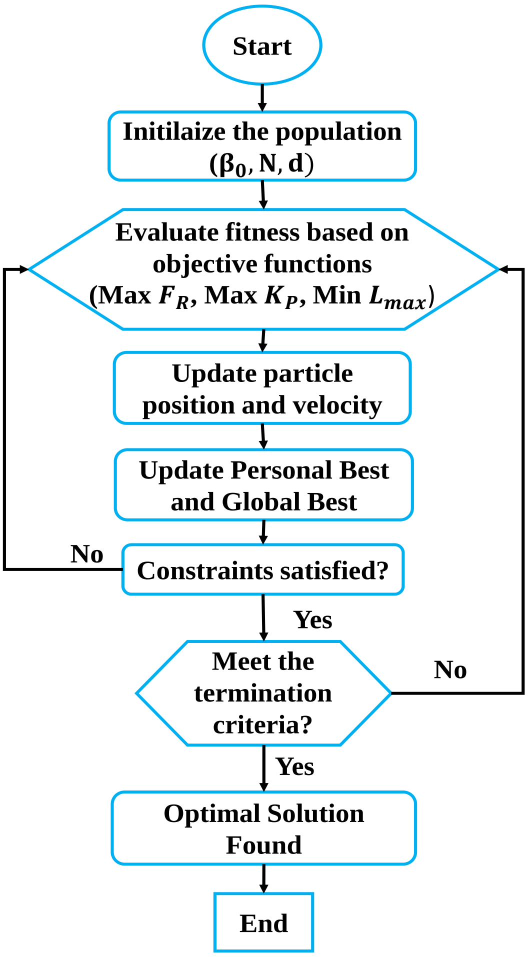

Figure 36. Flowchart of MOPSO.

Optimization parameters

The algorithm has several parameters that can be adjusted to influence its performance. In our study, I used a population size of 100 particles, and the maximum number of iterations is set to 200. I used a repository size of 100 particles, and 30 divisions for the adaptive grid. The values of the mutation rate and the global learning coefficients were set to 0.5, 1, and 2, respectively. These parameter values were chosen based on default values presented in the reference [201] that have shown their effectiveness in optimizing different problems. By fine-tuning these parameters, I was able to effectively explore the search space and find a set of stent designs that fulfill multiple objectives simultaneously.

3.2.6 Numerical simulations

To verify the accuracy of the results obtained from the numerical analysis and gain a deeper understanding of the mechanical behavior of stents during the crimping process, FE analysis simulations were conducted. The stent geometry was designed using SolidWorks software, utilizing the initial geometrical parameters, including braided angle (β_0), number of wires (N), the diameter of wires (d), and initial length (L_0) and diameter (D_0) of the stent. The generated geometry was imported into Abaqus/CAE version 6.14, providing the required framework for FE analysis. To analyze the stent's mechanical behavior, the geometry has meshed with 2-node linear beam elements (B31), which allows for both excellent computational efficiency and good accuracy of the responses. To model the contact between the braiding wires at the intersection points, I employed JOIN connectors, without friction. These elements were used to simulate the rotational behavior of wires at the intersection points by linking the two opposing nodes, allowing for unrestricted rotation around the intersection points, as already suggested in [211].

To accurately simulate the stent crimping process, a model of the crimper was exploited. The crimper was modelled as a cylindrical shell-type surface in Abaqus and meshed using a 4-node quadrilateral surface element, reduced integration (SFM3D4R). The inner surface of the crimper was also designated as a set to define the contact between the stent and the crimper during compression simulation.

Radial compression simulation

To accurately simulate the radial compression on the stent, a radial displacement was imposed on the crimper in cylindrical coordinates. Figure 37 shows the initial configuration of the simulation model. A frictionless surface-to-surface contact was then defined between the inner surface of the crimper and the outer node set of the stent. Additionally, to axially constrain the end of the stent, a displacement boundary condition was applied to the corresponding nodes. The material properties of NiTi were used for the stent, modeled as a linear material with an austenitic phase with the properties reported in section 3.2.3. Since the focus is on predicting the radial force on the stent wall at full deployment with approximately 40% global crimping, it is possible to assume that local stress stays within the linear elastic region, as the local deformation is fairly low. This condition was verified after the simulations.

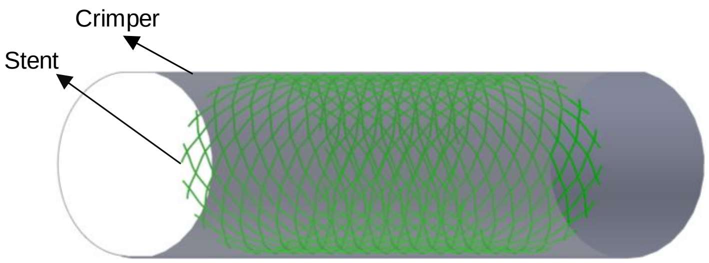

Figure 37. Model of the crimper and stent in the initial configuration.

3.2.7 Results and discussion

The findings of this study are provided in two main parts. Firstly, a comprehensive validation of the model's analytical results is presented. Secondly, the simulation results of the reference design and the optimized design are thoroughly compared.

Comparison of analytical and FE model

First, I designed a stent based on previous research conducted by [202] and then applied a radial displacement by means of the crimper surface to reduce the stent's external diameter from 22 mm to 10 mm ($D_0 \rightarrow D$). The design parameters for the stent and the characteristics of the FE model are presented in Table 7. By utilizing the FE model, I conducted a comparative analysis between our analytical/simulation results and the reference numerical data provided by [195] (see Figure 38). This approach enabled us to verify the accuracy of the analytical model and demonstrate its effectiveness in predicting the behavior of the stent.

As illustrated, the analytical model aligns perfectly with reference data in terms of length, radial force, and maximum ideal stress. In addition, the simulation results indicate strong agreement with the analytical and reference values for stent length versus stent diameter (Figure 38(b)). Figure 38(a) also shows that the simulation results for radial force follow a similar trend to the analytical/reference results, albeit with lower values.

It is important to mention that generally the free ends of the wires have a tendency to collapse, which lowers the force measured in the simulation when compared to the analytical model [203]. Furthermore, the previous study of [194] has shown that analytical model tends to overestimate radial pressure when compared to experimental results. Consequently, this overestimation affects the derived values of radial force and radial pressure stiffness as defined in Equation 46 and Equation 47. Therefore, the lower simulation values of the radial force compared to the numerical results suggest that our FE model in this study is closer to the actual experimental conditions than the reference model, which is an improvement over previous model.

Table 7. Design parameters for the stent and crimper, and characteristics of the FE model.

Parameters	**Stent**	**Crimper**
Initial external diameter D_0 (mm)	22	22.1
Final external diameter D_0 (mm)	10	10
Wire diameter d (mm)	0.22	-
Initial length L_0 (mm)	53.56	100
Initial branding angle β_0 (°)	30	-
Number of wires N	30	-
FE type	B13	SFM3D4R

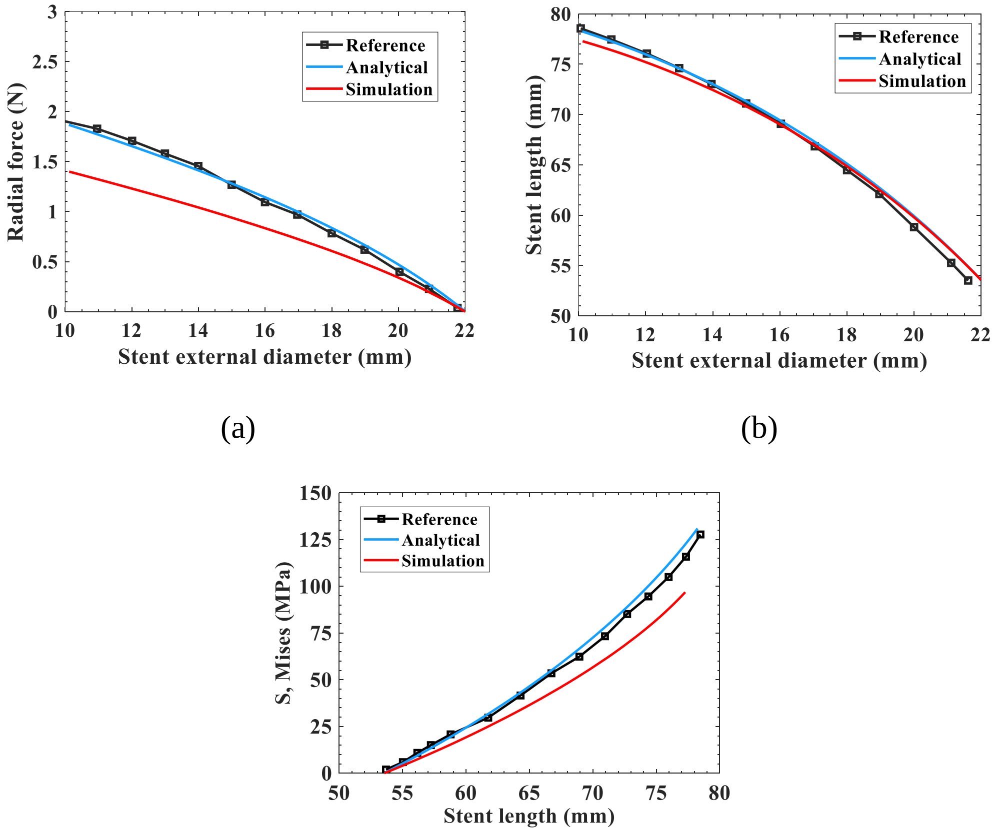

(a)

(b)

(c)

Figure 38. Comparison between the analytical and simulation results with the reference [195] : a) radial force versus the stent external diameter b) the length of the stent versus the stent external diameter and c) equivalent Von-Mises stress versus the length of the stent.

Moreover, the result of the simulation in terms of von Mises stress of a node-set positioned at the middle of the stent is depicted in Figure 38(c), which align well with the analytical/reference data. Additionally, our simulation results show that the maximum stress in the stent is around 135 MPa (as shown in Figure 39), which is in excellent agreement with the analytically derived maximum stress of approximately 130 MPa. The findings suggest that both the analytical and simulation models are effective tools for predicting stent behavior and designing the optimized stent geometry.

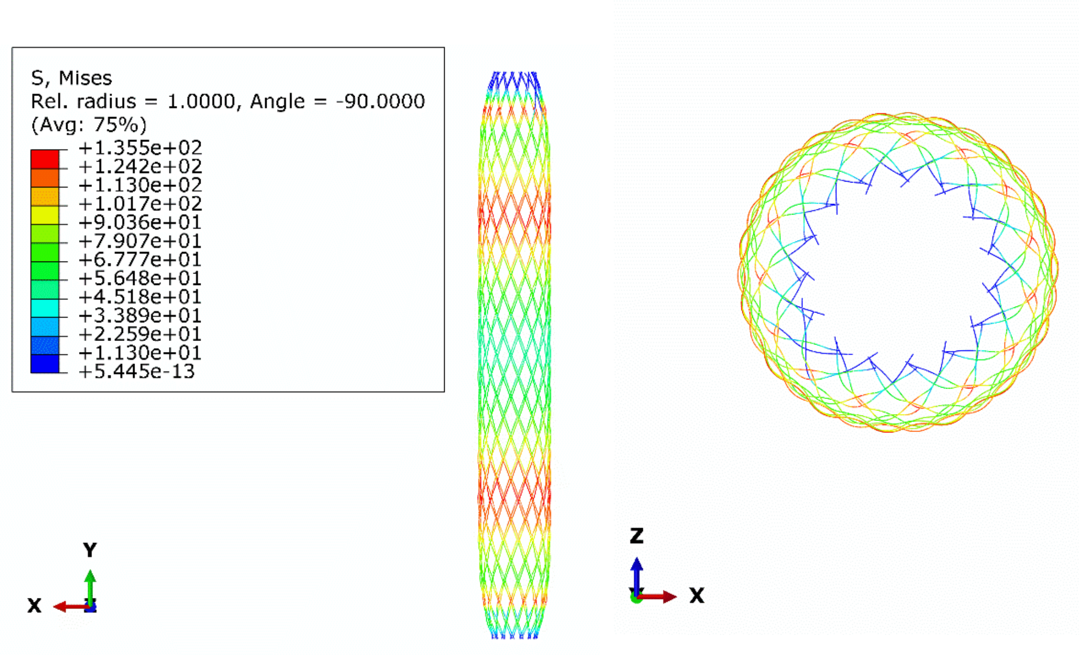

(a) (b)

Figure 39. Von Mises stress distribution under uniform radial compression; a) front view b) top view.

Optimized design

As stated previously in section 3.2.5, the stent design was optimized using the MOPSO technique. Our primary objective was to increase both radial force and radial stiffness while simultaneously reducing the length variation under axial loading. Through an iterative process of optimization, three design parameters are explored: wire diameter, number of coils, and braided angle. To ensure a meaningful comparison between the optimized and reference designs, constraints were set on both the volume of the stent and the maximum Von Mises stress. The optimized design parameters obtained through this process are presented in Table 8.

Table 8. Optimized design parameters

Initial branding angle $\boldsymbol{\beta_0}$ (°)	Number of wires N	Wire diameter d (mm)
42.55	16	0.29

Using the optimal set of parameters, the optimized design of the stent was created in SolidWorks (Figure 40). Then the generated model was imported to Abaqus to simulate its behavior under the radial displacement.

Figure 40. Comparative CAD design of the reference stent and optimized stent.

The Von Mises stress distribution of the optimal stent can be observed in Figure 41(a). The simulation findings indicate the maximum Von Mises stress is 155 MPa, which is still significantly lower than the yield stress (489 MPa). The initial assumption of elastic behavior is valid up to a strain of $\frac{yield\ stress}{Young's\ modulus} = 0.013$. Therefore, as long as the strain remains below this value, it makes no difference whether a linear model or a more complex model that considers non-linearity in the plateau region is utilized. Based on the simulation findings, I can confirm that the initial assumption is correct since the maximum strain on the stent is around $\frac{155}{35900} = 0.004$ (as shown in Figure 41(b)))), which is well below the elastic strain limit. It must be also noted that according to [212,213], ±0.4-0.5% is the maximum strain that must not be exceeded in order to avoid fatigue of NiTi. Considering that this level of strain is experienced only during crimping and deployment, and that the biomechanical forces are normally orders of magnitude lower, the safety margin for fatigue is sufficiently high.

Moreover, Figure 41(c) is included to illustrate the distribution and magnitude of radial reaction forces on the crimper. These values are critical for calculating the radial force exerted by the stent on the crimper. The radial forces depicted represent the individual forces at each node where the stent wires contact the crimper. To determine the total radial force exerted by the stent on the vessel wall, it is essential to calculate the reaction forces from all these contact points. Therefore, the total radial force is obtained by summing the radial reaction forces from all nodes.

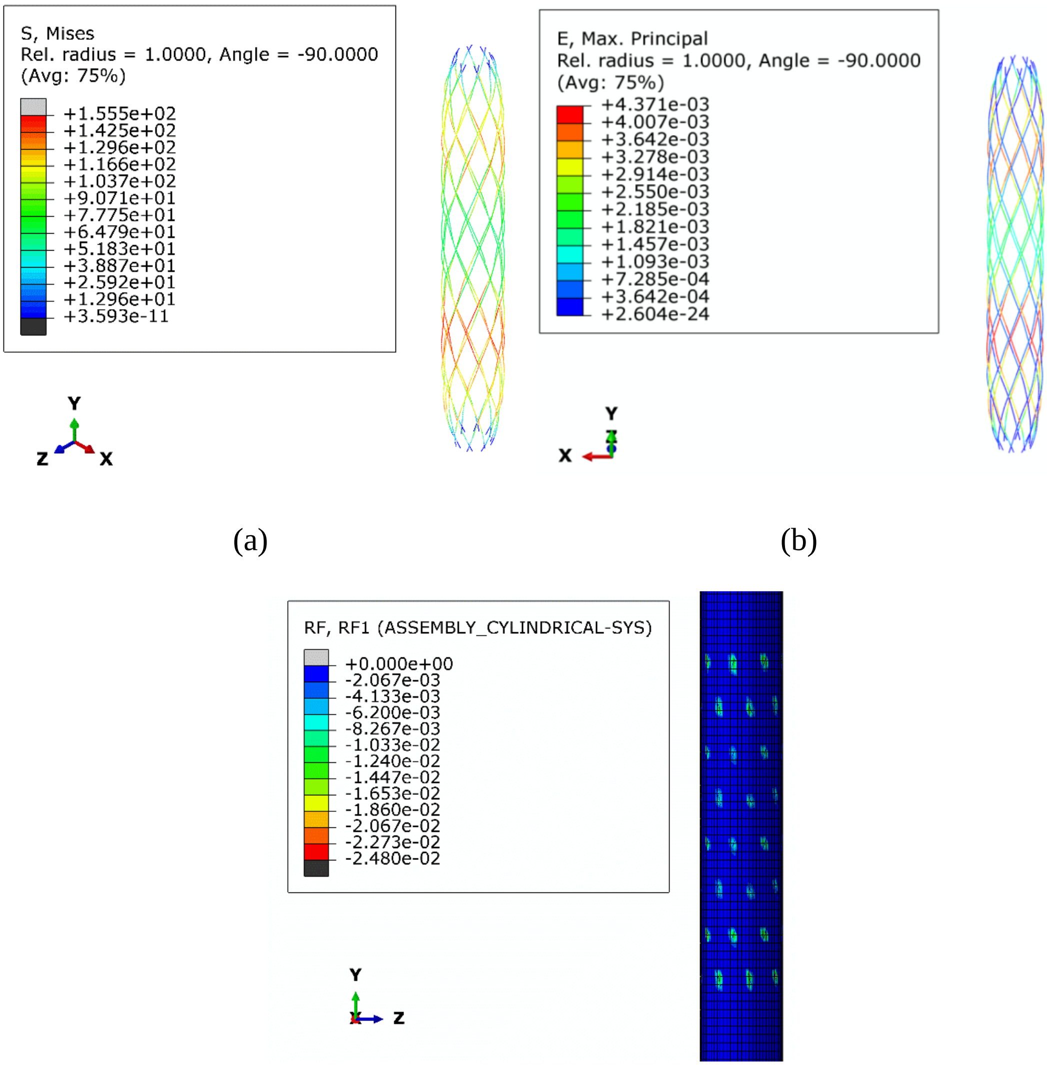

(a) (b)

(c)

Figure 41. Von Mises distribution of the optimal design, in MPa (a), principal strain distribution of the optimal design (b) and reaction force in radial direction on the crimper in N (c).

In this context, the reaction forces on all nodes on the crimper are summed at each time step, as shown in Figure 42(a).

As shown in the figure, the optimized stent design exhibits a maximum radial force of 1.83 N which represents a 31% improvement over reference design. Moreover, Figure 42(b) shows a comparison of radial pressure stiffness between the optimized and the reference designed which demonstrates improvements in all variations of diameter of around 40%. The length variation of the optimized stent was also reduced by 4.6% when compared to the reference design, as evident from Figure 42(c). While this reduction in foreshortening may seem modest and might not significantly impact clinical performance by itself, it is important to consider it in the context of the overall optimization, i.e., this improvement was achieved alongside substantial enhancements in radial force and radial stiffness, demonstrating the overall effectiveness of the optimization process.

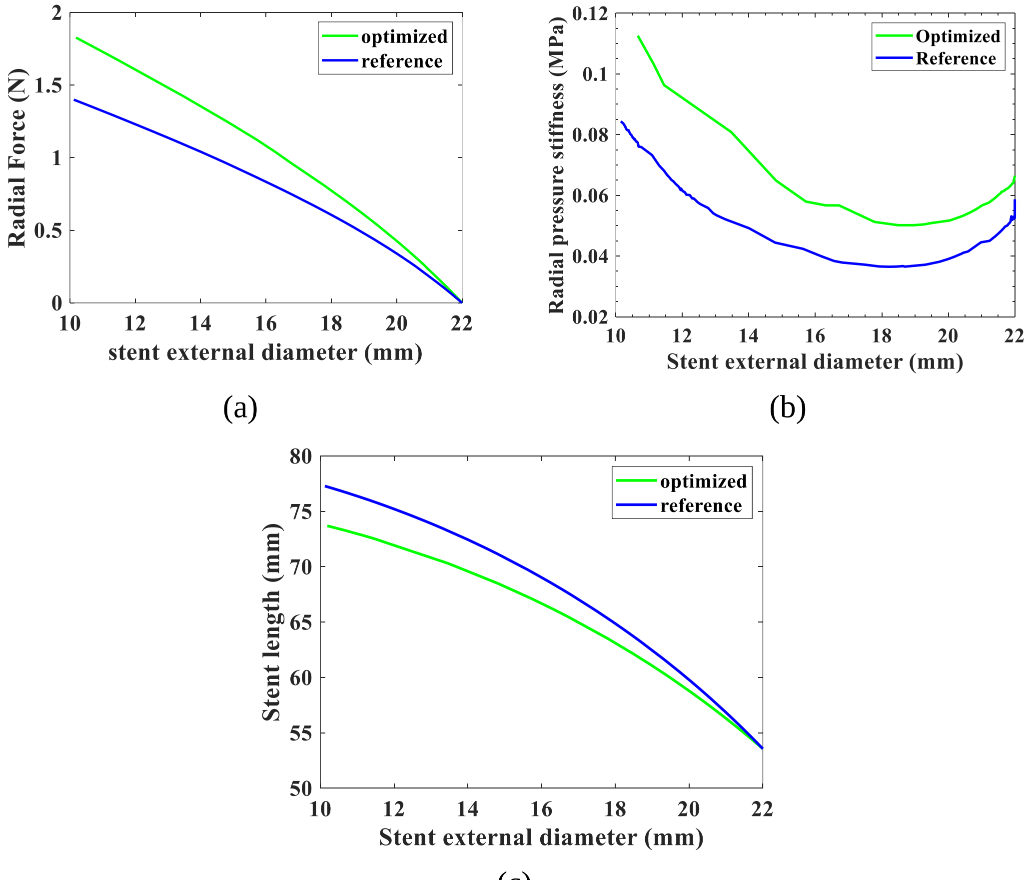

(a)

(b)

(c)

Figure 42. Simulation results: comparison between the optimized stent design and the reference design a) radial force versus stent external diameter b) radial pressure stiffness versus stent external diameter c) stent length versus stent external diameter.

In addition to assessing the effectiveness of the optimized stent, the performance of the optimized stent design was evaluated by calculating the percentage improvement in radial force and radial stiffness in comparison to the reference design. As a function of the stent diameter, as depicted in Figure 43, the improvement percentage chart clearly demonstrates that the optimized stent design indicated an overall improvement over the reference design for all diameter variations. The findings reveal that the MOPSO algorithm is capable of optimizing stent design, thereby enhancing stent performance and improving patient clinical outcomes.

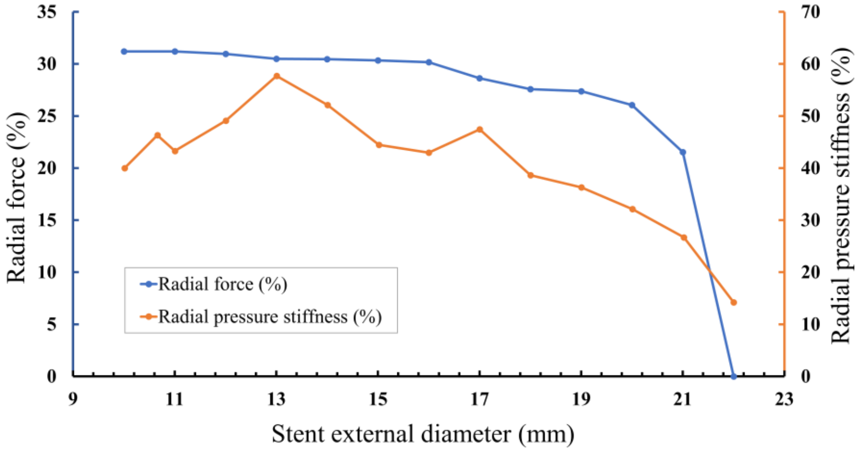

Figure 43. Radial force and radial pressure stiffness percentage increase of the optimized model versus stent external diameter.

Furthermore, in order to show the stent’s ability to endure substantial deformation without failure, the local strain and global hoop/circumferential strain can be compared. By utilizing the stress in the stent and the Young's modulus E, the local strain of the stent can be calculated using Hooke's law. To compute the global hoop/circumferential strain of the optimized stent design, we can consider the stent as a cylinder with a specific thickness equal to the optimized wire's diameter d of 0.29 mm (presented in Table 8), that changes from an initial external diameter D_0 of 53.56 mm to a final external diameter of 10 mm (see Figure 42(c))). The maximum hoop strain can be computed through Equation 52, where U_r, and r represent the displacement in radial direction, and radius of the cylinder, respectively [214].

$$\varepsilon_{\theta\theta} = \frac{U_r}{r}$$ Equation 52

Even though a considerable global hoop strain of approximately 54% is presented, the local strain, on the other hand, remained remarkably low, measuring only around 0.4%. This observation highlights the braided stent’s ability to undergo significant global deformation while simultaneously experiencing minimal strain in localized regions. These distributions of the global and local strains contribute to the stent's overall performance and durability by preserving its flexibility without causing structural failure.

3.3 SCITECH-SOLARIS, A SELF-EXPANDING LASER-CUT NITI STENT: DESIGN, SIMULATION, AND EXPERIMENTAL VALIDATION

3.3.1 Laser cutting technique

It is not possible to manufacture stents with conventional CNC (Computer Numerical Control) machining techniques, due to the high wear of the tool, poor dimensional accuracy and incompatibility with the intrinsic material properties of NiTi. Therefore, the laser cutting technique is currently the most widely used method for stent fabrication (Figure 44). The feedstock is a tubular workpiece of the desired material (for example, NiTi) with the desired diameter and thickness. A high-energy-density laser beam is focused on the surface of the workpiece and the material vaporizes leaving the desired stent mesh. The remaining material is then blown away by a pressurized air flow [79,81,215]. As a result, the cross section of the ligaments is roughly rectangular. This type of cross section has been reported to possibly promote turbulence in blood flow, which could lead to restenosis and late stent thrombosis [216]. After being laser cut, the NiTi microtubes are heat-treated and chemically etched to obtain the desired mechanical properties and surface finish [217].

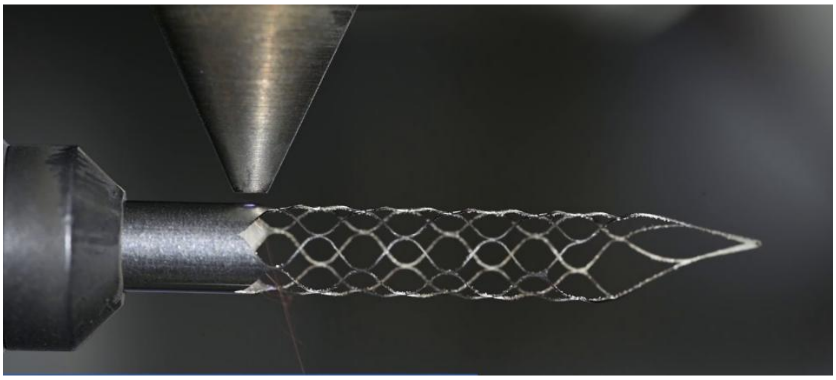

Figure 44. Laser-cut technique [218].

3.3.2 Self-Expanding NiTi Scitech-Solaris stent

The Scitech-Solaris is a self-expanding endograft featuring a laser-cut NiTi stent structure encapsulated by a thin polytetrafluoroethylene (PTFE) membrane, fabricated via an electrospinning process[219]. While the PTFE membrane enhances sealing properties and provides additional durability, this section focuses on the advanced laser-cut NiTi framework, which is the core structural component of the stent.

As shown in Figure 45, the device incorporates a hydrophilic pull-back delivery system designed for precise deployment and enhanced navigability. Key features of this system include an anti-jumping mechanism to prevent unintentional stent deployment, a braided hydrophilic shaft for enhanced flexibility and kink resistance, and radiopaque tantalum markers for superior visibility during imaging. Additionally, the atraumatic flexible tip minimizes tissue damage during insertion.

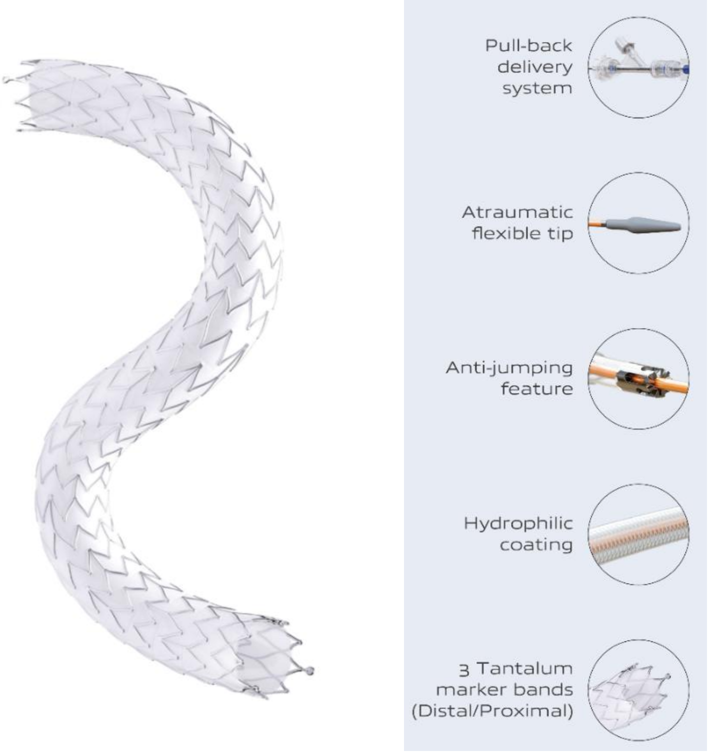

Figure 45. Scitech-Solaris stent with hydrophilic pull-back delivery system and key features [219].

The structural design of the Solaris stent is meticulously engineered, incorporating a hybrid configuration that combines open-cell and closed-cell designs. The central section employs an open-cell design, which enhances flexibility and facilitates smooth deployment, while the ends utilize a closed-cell design for improved radial support and anchoring. Each ring is interconnected by three straight bridges, ensuring robust structural stability while maintaining sufficient flexibility. This thoughtful design allows the Solaris stent to conform effectively to vascular anatomy while maintaining its mechanical integrity under physiological loads.

3.3.3 Dimensional measurement and CAD design of the Scitech-Solaris stent

A sample of the Scitech-Solaris stent is available as a case study in our facility.

Figure 46. Scitech Solaris.

To ensure optimal design and functionality, I employ microscopic imaging techniques to measure the precise dimensions of the stent. This data is crucial for our Computer-Aided Design (CAD) processes, allowing us to create highly accurate models that reflect the stent's specifications. I have utilized these CAD models for simulation in Abaqus then, which enables us to analyze the stent's performance under various conditions. Figure 47 and Table 9 present the dimensions obtained from microscopic imaging.

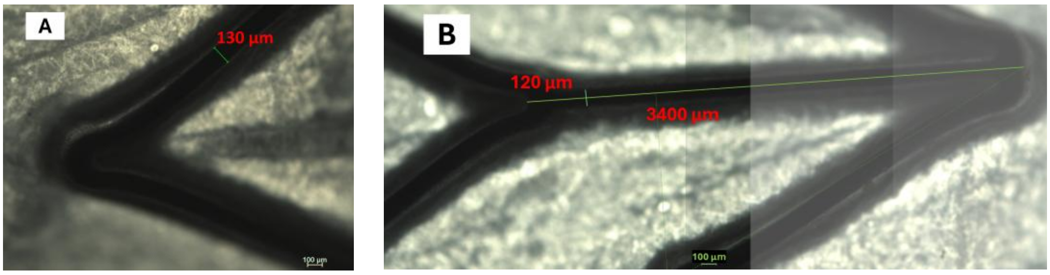

Figure 47. Microscope images of the Scitech-Solaris stent, A) struts' dimensions B) bridges' dimensions.

Table 9. Dimensions of the Scitech-Solaris stent obtained from microscopic imaging technique.

Parameter	**Stent**			**Bridge**		**Strut's width**
	Diameter	**Length**	**Thickness**	**Length**	**Width**	
Dimension (mm)	8	40	0.22	3.4	0.12	0.13

I have successfully developed a detailed Computer-Aided Design (CAD) model of the Scitech-Solaris stent using SolidWorks®, incorporating precise dimensional measurements derived from microscopic imaging techniques presented in Table 9, as illustrated in Figure 48.

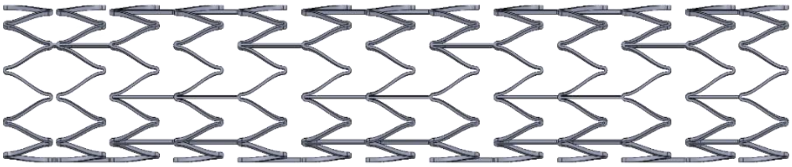

Figure 48. CAD design model of the Scitech-Solaris stent created in SolidWorks.

3.3.4 Superelastic material modelling for the Scitech-Solaris stent

The superelastic behavior of NiTi is modeled in this work starting from the framework set forth in previous work [220]. This model develops the complex, finite-strain superelastic behavior of SMAs, especially NiTi. This model was first developed by Auricchio et al. [220] as a constitutive framework to model the specific phase transformations these materials exhibit when subjected to large strains. Their methodology considers mechanical and thermal effects, thus providing a more realistic simulation of the behavior of NiTi during loading and unloading. Figure 49 shows a typical behavior of superelastic NiTi and the description of each parameter can be seen in n Table 10.

Table 10.

Following this foundational modelling, a trial-and-error approach that combined both experimental tests and finite element modelling of the Scitech-Solaris stent was used. I started by carrying out a series of experiments to gather data on the stent's performance under CR loading/unloading condition. Then, I ran FE simulations for CR to analyze the stent's behavior. By comparing the FE result and experimental data, I systematically adjusted the model’s parameters based on our observations to fine-tune the model, ensuring that our model accurately reflected the actual performance of the stent. This iterative process allowed us to achieve a precise alignment between the model predictions and experimental outcomes.

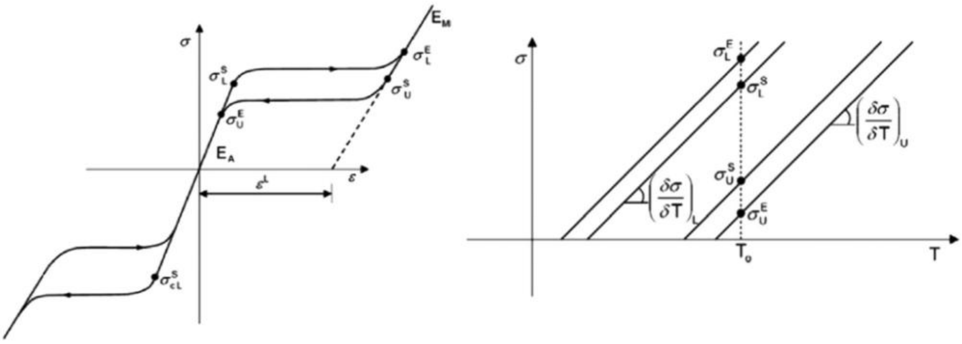

Figure 49. Stress-strain and stress-temperature curves of NiTi material [221].

Experimental setup for CR testing

As already mentioned, to refine the model's parameter, a series of preliminary CR tests were conducted. The CR test was assessed using parallel plates and a universal testing machine, following standardized protocols. A compressive force was applied to the stent until its diameter was reduced to 50% of its initial size, which is 8 mm, resulting in a final diameter of 4 mm. The experimental data, along with a depiction of the experimental setup, are presented in Figure 50.

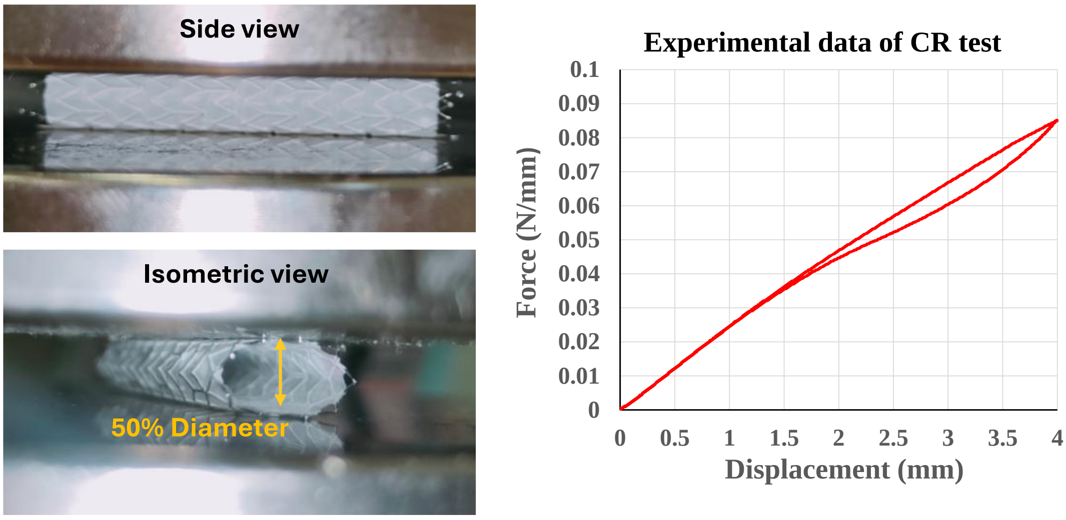

(a) (b)

Figure 50. CR test: a) experimental setup and b) force-displacement behavior.

FEM simulation and material modelling for the Scitech-Solaris stent

Due to the axial symmetry of the stent, the FEM simulation was conducted on a single cell of the stent. The outer surface of the stent, represented in its CAD design created in SolidWorks (as discussed in section 3.3.3), was imported into Abaqus. The section type was defined as shell homogeneous, which is appropriate for capturing the behavior of thin-walled structures like stents. Then a predefined temperature of 22 °C—consistent with the reference temperature—was assigned to the stent and to prevent any rotational movement during the simulation, two nodes were fixed in the horizontal direction.

In addition, two compression plates were modelled as 3D analytic rigid surfaces, each measuring 8 mm by 20 mm. A reference point was defined at the center of each plate's surface to facilitate accurate force measurements later. A surface-to-surface, finite sliding frictionless contact was established between the stent surface (designated as the slave) and the plates (acting as the master). Finally, a vertical displacement of 4 mm was then applied to the upper plate while keeping the lower plate fixed. Throughout this process, I recorded both the distance between the plates and the reaction force at the reference point of the upper plate. It is crucial to note that, due to symmetrical geometry in our model, the force obtained from this analysis was multiplied by the total length of the stent to derive final results, ensuring that our simulations accurately reflect the stent's overall behavior under loading conditions.

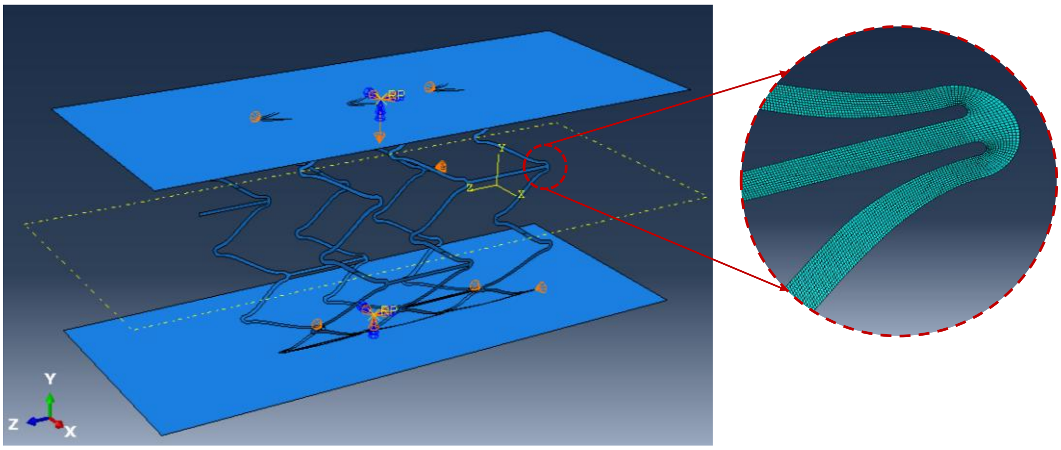

Figure 51. FEM of the Scitech-Solaris stent, illustrating the loading setup that depicts the interaction between the stent and compression plates, and meshing configuration.

The material model for the stent was defined using the built-in superelastic material model available in ABAQUS. To establish a baseline for the model’s parameters, I referenced initial values from a related journal article [221], which studies experimental and computational methods to discuss the requirements of a self-expandable stent. This provided a useful starting point for defining the parameters necessary for accurate modelling.

3.3.5 Results and discussion

Starting with the initial values from [221], the parameters within ABAQUS were adjusted to better align the simulation results with experimental data. By running a series of simulation and systematically comparing the outcomes with actual experimental observations, I was able to identify discrepancies and refine the parameter values accordingly that fitted the Scitech-Solaris model. The final model-fit parameters are presented in Table 10.

Table 10. NiTi material parameters that fit the CR test.

Symbols	**Description**	**Model-fit**
E_A	Austenite elasticity	6900 MPa
ϑ_A	Austenite Poisson’s ratio	0.33
E_M	Martensite elasticity	22000 MPa
ϑ_M	Martensite Poisson’s ratio	0.33
E^L	Transformation strain	0.04
$\left(\frac{\partial\sigma}{\partial T}\right)^L$	Loading	6.7
σ_L^S	Start of Transformation Loading	240 MPa
σ_L^E	End of Transformation Loading	310 MPa
T_0	Reference temperature	22
$\left(\frac{\partial\sigma}{\partial T}\right)^U$	Unloading	10
σ_U^S	Start of Transformation Unloading	180 MPa
σ_U^E	End of Transformation Unloading	120 MPa
σ_{CL}^S	Start of Transformation Stress during unloading in Compression as positive value	330 MPa
ε_V^L	Volumetric transformation strain	0.04

Figure 52 presents a comparison between the experimental data obtained from the CR test and the FEM simulation results derived from the fitted parameters detailed in Table 10. This comparison illustrates the effectiveness of our parameter adjustments, demonstrating how well the FEM model aligns with actual experimental outcomes.

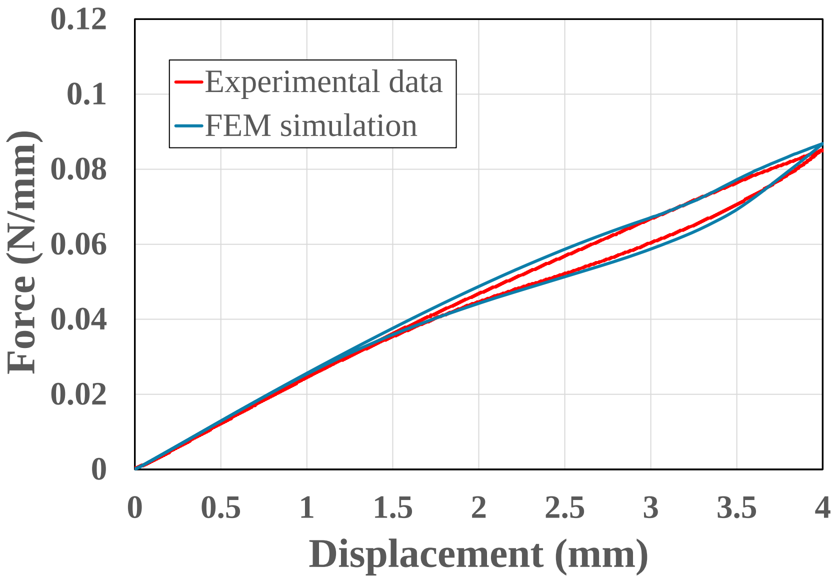

Figure 52. Comparison of experimental data from the CR test and FEM simulation results utilizing fitted parameters in n Table 10.

Table 10 for the Scitech-Solaris stent.

Building on this foundation, future work can focus on optimizing the stent's effectiveness by modifying key parameters, such as the thickness and width of struts or bridges. By running simulations to evaluate the effects of these changes on critical performance metrics like RRF and CR, it becomes possible to identify optimal dimensions for enhancing the stent's design and clinical functionality.

3.4 ADDITIVE MANUFACTURING OF NITI STENTS: TECHNIQUE, DESIGN, AND CHALLENGES

3.4.1 Additive manufacturing techniques

Additive manufacturing (AM) of stents is an area of growing research that has the potential to lead to substantial improvements in patient outcomes due to its ability to rapidly develop custom stents. Laser beam technology has developed to the point that today laser beams are very small (typically 20-80 µm); therefore, they can provide not only the means for developing stents through subtractive manufacturing but also AM through laser powder bed fusion [215]. Powder bed fusion (PBF) is defined by ISO/ASTM 52900:2021 standard and is an AM technique that uses either laser or electron beams to selectively melt or fuse powder particles on a powder bed in a layer-by-layer manner. Other PBF techniques such as electron beam powder bed fusion (EB-PBF) are unsuited for manufacturing vascular stents due to the larger spot size of the electron beams (about 100 µm) [222]. Therefore, nowadays only laser-based powder bed fusion (LB-PBF), sometimes also called selective laser melting, is a viable manufacturing technique for NiTi stents.

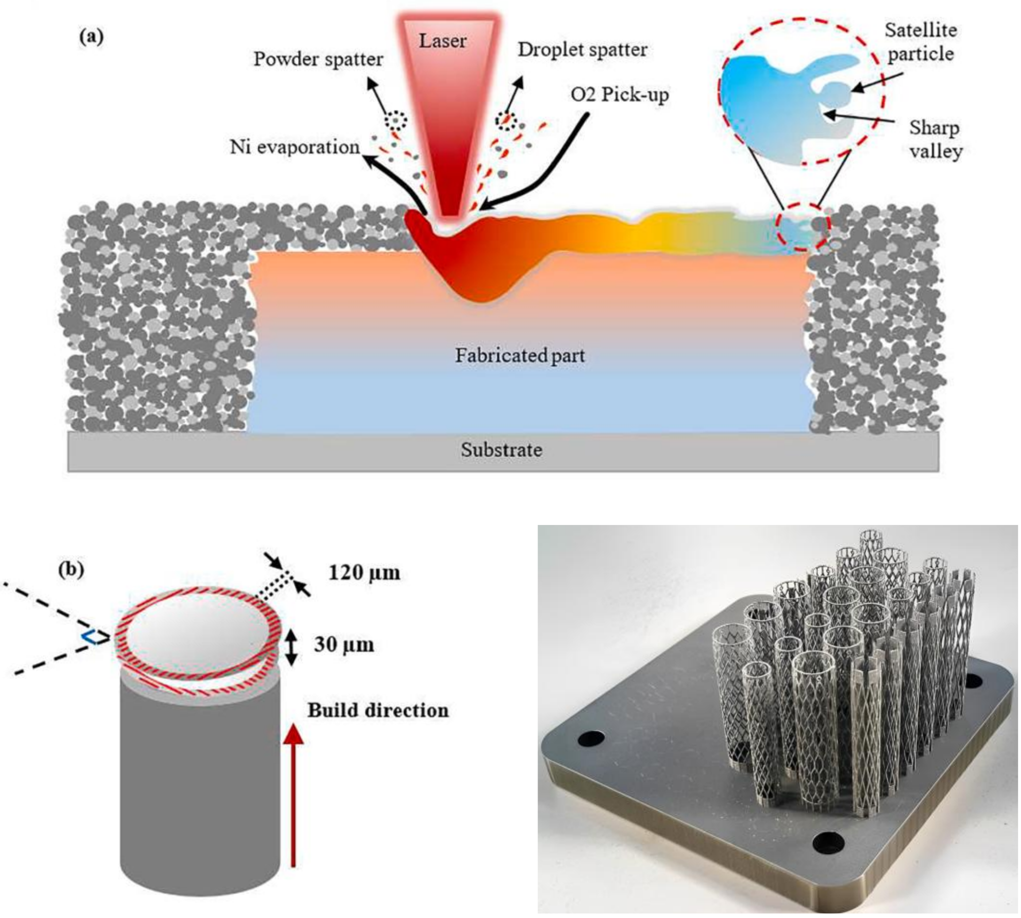

Figure 53. Additive manufacturing: (a) Schematic of selective laser melting process (b) layering and scanning strategy[223] and (c) SLM NiTi stent on the substrate [224].

A collaborative research project was recently undertaken by researchers from the Universities of Ferrara and Pisa, focusing on the selection of powders and optimization of process parameters for the fabrication of NiTi-based structures using the AM technique [225]. The findings of their study were presented at the 4.0 National AIM Conference (4.0° Convegno Nazionale AIM).

When using PBF to print NiTi powder, there are a number of parameters that need to be taken into account. These include laser power, layer thickness, hatch distance, laser scanning speed, thermal diffusivity, material conductivity, and distance from the point heat source. Some of these parameters are listed in Table 11, along with the ranges that were studied in their research to see how changing the parameters affected the microstructural morphology of the printed samples. The following provides a brief overview of the methodology employed in their research and the key results obtained. Using the parameters outlined in Table 11, they fabricated 10 cubic

NiTi samples. Moreover, the characteristics of the NiTi powder used in the process are detailed in Table 12.

Table 11. The range of parameters for preparing cubic samples with PBF AM technique.

Parameters	**Range**
Layer thickness	$30 - 60\ (\mu m)$
Hatch distance	$30 - 120\ (\mu m)$
Power	$75 - 250\ (W)$
Speed	$0.50 - 1.60\ (m/s)$

Table 12. Characteristics of the NiTi Powder.

Characteristics	**values**
Composition	50.8 %Ni
Particle size	53 µm (D90)
Impurity level	C= 351 ppm, O = 241 ppm
Transformation temperature (A_f)	-1 °C

The locations of all 10 printed samples on the normalized laser power (p*) versus normalized velocity (v*) graph, along with their corresponding porosity, are illustrated in Figure 54.

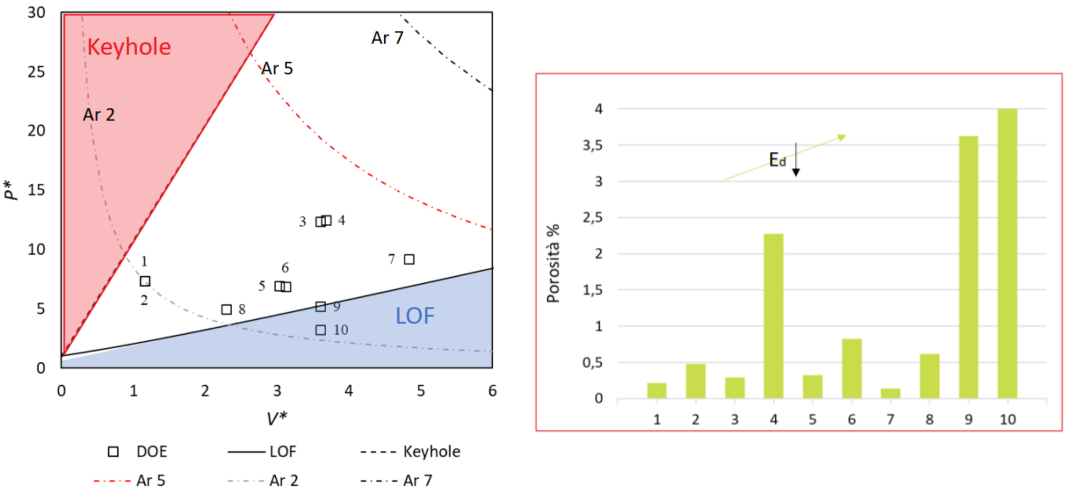

(a) (b)

Figure 54. Properties of the printed samples: a) normalized power and normalized velocity of each sample, and b) porosity of the printed samples[225].

As shown in Figure 54, samples 9 and 10 fall within the lack of fusion (LOF) region and exhibit the highest porosity. Additionally, sample 4 demonstrates greater porosity compared to its neighboring sample on the 2D p*-v* graph (sample 3).

A further analyzed in the morphological investigation was conducted to evaluate the correlation between the p*-v* value and the porosity of each sample with microstructural properties of the printed samples using optical and electronic microscopy. Figure 55 shows microstructural images of some of the printed samples, as can be seen sample 9 exhibits high porosity, displays a lack of fusion, sample 4 demonstrates keyhole morphology, while Sample 3 reveals a crack perpendicular to the build direction (BD). In contrast, no major defects are observed in sample 7, which has a density exceeding 99.5%.

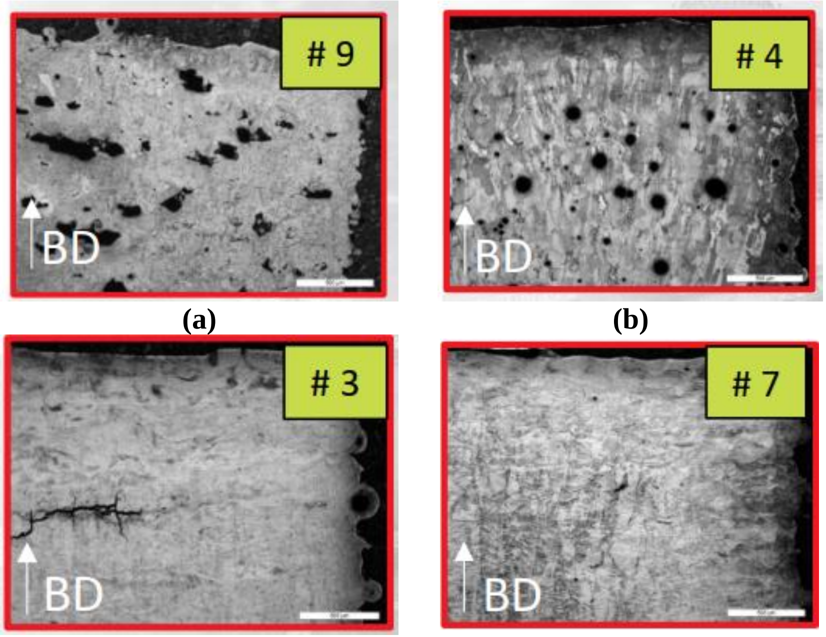

(a) **(b)**

(c) **(d)**

Figure 55. Microstructural images of some printed samples: a) sample 9 with LOF, b) sample 4 with keyhole c) sample 3 with crack perpendicular to BD and, d) sample 7 without major defect [225].

In conclusion, they found that the p*-v* value should be positioned within the white area showing in Figure 54, outside the lack-of-fusion (LOF) and keyhole zones. However, this does not guarantee a high-quality surface after the printing process, and other related factors should be further investigated. Additionally, a morphological investigation should be performed after the printing process to assess the surface quality of the samples and determine the optimal parameters.

3.4.2 Design and process challenges in AM of NiTi stent

The design and manufacturing of NiTi stents using AM present both significant opportunities and unique challenges. While AM techniques like LB-PBF enable the creation of highly customized stents with complex geometries tailored to patient-specific needs, they also introduce technical limitations that affect the mechanical properties, surface quality, and overall performance of the stents.

For what concerns the mechanical properties of additive-manufactured NiTi devices, they have been compared with the mechanical properties of NiTi devices obtained with traditional manufacturing techniques (e.g. laser cut) in several studies; for example, a work from Meier et al. [226] shows that both AM NiTi and conventional NiTi materials show a similar functional behavior during thermomechanical cycling, whereas fracture strength and fracture strains of AM NiTi are slightly lower. This highlights that AM is a promising manufacturing method for NiTi alloys. Another difference regards the surface finish of AM NiTi parts compared to conventional NiTi parts.

The most important advantage of applying AM to stent manufacture is the ability to produce fully customizable stents and, in general, medical devices based on patient-specific 3D models. These stents would have a variable geometry that is consistent with the anatomy of the patient. This design flexibility has also been demonstrated with the production of bifurcated geometries [227]. Another advantage of the AM of stents is that the production is not dependent or limited by the availability of suitable commercially available tubes for laser cutting. For the latter method, when the available tube diameters do not perfectly match the ideal diameter needed for the anatomy of a specific patient, the surgeons select a stent with a diameter slightly larger than necessary to ensure proper fitting, which could lead to negative consequences such as irritation of the vascular wall and possible inflammatory response due to stent oversize [228]. Furthermore, one last advantage not to be overlooked in utilizing the LB-PBF techniques, is waste minimization during production, compared to laser cutting.

However, there are also some significant limitations in the manufacture of AM stents. A main issue regards the low surface quality of the as-built surfaces, especially since the required strut thicknesses of NiTi stents are very small, in the order of 100-500 μm, which is comparable to the size of the powder particles (10-60 μm) and the laser beam. This requires careful control of the energy release but also the scan vector accuracy [215,227]. Many studies point out that only the energy level is not sensitive enough to predict the printing quality [216]. In addition, shape-memory and SE properties are highly dependent on the powder composition and process settings. Any slight changes in the nickel content due to the laser melting during the process in the composition can change the transformation temperatures and, subsequently, the superelastic behavior of the AM stents [229]. This further increases the difficulty of parameter optimization in the fabrication of thin NiTi structures through this method. The high-intensity laser beam could lead to increased porosity, significant residual stress, and high surface roughness [222]. A balance between the porosity and the transition temperature control is hard to achieve by controlling the laser process parameters, hence, consecutive heat treatments and surface finishing operations may be applied to modify the microstructure as built and improve the mechanical properties of AM stents [217]. To improve the surface quality of LB-PBF stents, chemical etching must be performed. This process also lowers the strut thickness, improving the stent performance [217,229]. This technique and other surface modifications, such as coating, passivation, laser polishing [230] and electropolishing, can also be advantageous in overcoming the potential issue of nickel release into the bloodstream in the human body, which is a fundamental issue to avoid in order to guarantee the biocompatibility of the stent [229,231,232]. Another important aspect to be considered for the AM of NiTi stents is that additive manufactured devices often present anisotropic mechanical properties due to the intrinsic manufacturing techniques adopted [233]. More precisely, there could be a different mechanical behavior of the stent due to the direction of printed layers. Building direction and scanning pathway are shown to greatly influence the behavior of additive-manufactured devices: M. Somireddy and A. Czekanski [234], showed that building orientation (edge, flat or upright) of additive-manufactured composite structures significantly influences the final properties of the structure, tested through flexural loading, while S. Dadbakhsh et al. [235], showed how building direction, scanning direction and scanning speed influence the compression behavior and shape memory response of selective laser melted NiTi specimens. The anisotropy of a device, often considered a negative aspect, could be exploited to modify the mechanical behavior of a stent in one direction compared to the others, but these considerations are beyond the scope of this review article. Future investigations in this sense will be necessary in the search for the ideal stent for the specific need. Furthermore, the design phase also needs to be considered when utilizing LB-PBF to produce NiTi stents. The stent design should avoid large overhangs to minimize supports during printing, and in addition, removing the support structure would affect the surface roughness of the final product [222,227–229]. Despite these limitations, AM opens up new avenues in terms of customization of the devices, which could be tailored to the patient’s vessels in combination with precise preoperative assessment (e.g. CT scan or MR).

Figure 56 shows some stent models that we created in SolidWorks to address the geometry limitations of the stent design with AM like as wall thickness, aspect ratio, overhang, and the need for support structures. By optimizing these geometric parameter values, the designs aim to enhance manufacturability. It must be noted that different 3D printing machines can have varying specifications and limitations. These constraints necessitate careful design considerations to ensure that the stent can be successfully printed within the capabilities of the specific machine being used. For instance, Design 1 and 2 in Figure 56 is made for a printing machine that has important constraints concerning two factors: the section sizes must be about 0.3 × 0.3 mm with a fillet of 0.05 mm, and the structures must be self-supported during printing. On the other hand, design 3 and 4 in Figure 56 are made for a different machine with distinct requirements, including an aspect ratio of 8:1, wall thickness exceeding 0.25 mm, fillet size more than 1 mm, and overhang greater that 47°. The following table summarizes the specifications for each stent design, including the outer diameter, length, thickness, width, and the need for support during printing.

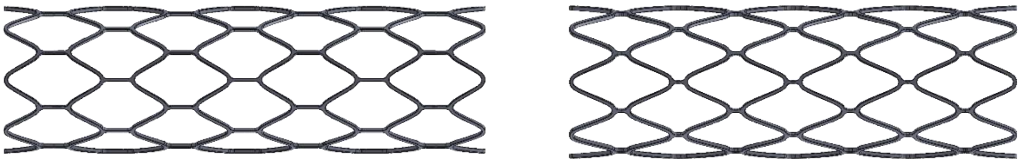

(a) Design 1

(b) Design 2

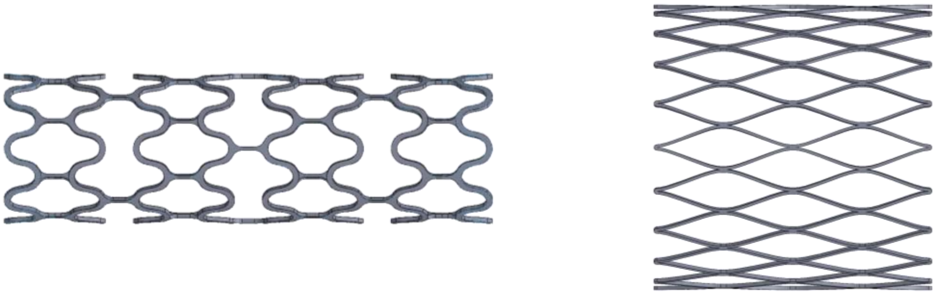

(c) Design 3

(d) Design 4

Figure 56. Stent models which are designed in SolidWorks to address geometry limitations with specific printing machines.

Table 13. Specifications for each stent design of Figure 56, including dimensions and support requirements.

(mm)	**Diameter**	**Length**	**Thickness**	**Bridge width**	**Strut width**	**Need of support**
Design 1	14	45.80	0.4	0.3	0.35	No
Design 2	14	41	0.4	0.3	0.35	No
Design 3	14	4.80	0.4	0.3	0.55	Yes
Design 4	30	30	0.4	0.3	0.3	No

3.5 ONGOING TRENDS IN STENT DESIGN

Cardiovascular disease remains a formidable global health challenge, contributing significantly to morbidity and mortality worldwide. Although stenting is an effective way to treat cardiovascular disease, the clinical reports reveal that there are still some issues such as vessel recoiling and stents migration post-deployment, fracture, and in-stent restenosis. Furthermore, the scarce presence of commercial stents suitable for deployment into some complex anatomy districts (bifurcations, diameter variation, and so on) exacerbates the challenges in cardiovascular intervention, where it falls upon the surgeon to choose one or more than one stent to meet the specific clinical needs of the patient [236]. Moreover, the inherent anatomical diversity among patients further complicates stent selection, adding another layer of complexity to treatment strategies. Thus, studying the design of an optimum stent that can mitigate these limitations is still a hot topic both for researchers and companies, aiming to enhance treatment efficacy and patients' health. Scholars devoted a strong effort to improving biocompatibility, reducing failure rates, and enhancing the performance of stents through advanced materials, optimum cell-design, and manufacturing techniques. Therefore, biodegradable stents are a significant trend nowadays [237–240], as they boast exceptional biocompatibility that plays a pivotal role in their rising popularity. They are designed to provide temporary support tissue growth before dissolving completely, thereby minimizing long-term complications. This evolution addresses the limitations inherent in durable polymer-based conventional drug-eluting stents, which raise the risk of in-stent restenosis and stent thrombosis by causing neoatherosclerosis and chronic local inflammation [241]. On the design and technology side, there is a growing interest in using AM techniques to manufacture stents. AM has emerged as a prominent trend in recent years, evident from the increasing number of publications on AM of different stents either BMS or BDS [222,229,237,242–246]. This trend signifies a fundamental shift in stent manufacturing methodologies, particularly in response to the limitations associated with conventional manufacturing processes such as laser-cutting. For instance, the dimensions of the stents that are conventionally manufactured by laser cutting from tubes, are dependent on available tubes, limiting dimensional selection of the stent. The available tube diameters may not perfectly match the ideal diameter needed for a particular patient's anatomy, forcing the surgeons to select a stent with a diameter slightly larger than necessary to ensure that it fits properly within the blood vessel, which can lead to negative clinical consequences, such as thrombosis and restenosis [228]. While considering AM, the design and manufacture of patient-specific stents, that precisely conform to individual vascular dimensions, is now possible and has started becoming more popular recently [247,248]. Moreover, AM can deal with complex geometries such as vessel bifurcations, which are typical of many regions in the vascular system. This approach has been recently investigated in technical literature [249] but AM in general offers a solution for creating and manufacturing complex geometries and cell designs. The freedom of shape given by AM has recently motivated designers to explore and analyze more complex geometries such as auxetic structures [250–252] to enhance mechanical properties and overall performance of stents.

The increasing use of AM opens the need for the designer to move from the current state of the art, largely based on laser-cut tubes and investigate new shapes and geometry, which is why the collection of dimensions and the definition of figures of merit is fundamental for the next generation of stents. The comparative tables reported in this review show that the solutions could be very different in terms of strut size, cell shape and design, and on top of this, strong improvements can be envisioned mainly relying on possible customization of these products based on computed tomography (CT) scans of patients. The use of new emerging technologies not only allows the designers to achieve the best trade-off between the several figures of merit of the endovascular NiTi SX stents but also opens new possibilities in terms of optimization of the geometry based on methods such as generative design and topological optimization [102,250,253,254].

In summary, the current trends in stent design and manufacturing reflect a significant shift towards addressing the limitations and challenges faced in cardiovascular interventions. Researchers are increasingly focusing on enhancing biocompatibility and improving stent performance through the use of advanced materials, optimal cell designs, and innovative manufacturing techniques such as AM. This work, providing a quantitative insight into the geometry, the dimension, and the mechanical properties of many commercial stents both for arterial and venous applications along with a detailed description of the main figures of merit of the stents, will help the future stent designers in exploiting new possibilities such as AM to improve the performance of these devices and enhance global health.

3.6 SUMMARY AND IMPLICATIONS

Endovascular stents have revolutionized the treatment of atherosclerotic vascular disease, offering a minimally invasive alternative to conventional open surgery. This advancement has significantly improved patient outcomes, minimizing trauma, recovery time, and associated healthcare costs. Among these, SX NiTi stents stand out due to their superelastic properties, which allow them to adapt dynamically to vascular deformation while maintaining vessel patency. Over the past two decades, the market has witnessed a proliferation of diverse stent designs, many of which incorporate hybrid configurations to balance flexibility, mechanical strength, and biocompatibility.

This chapter explored the key aspects of SX NiTi stent optimization, providing insights into their development, manufacturing methods, and mechanical performance. By combining historical perspectives with advanced analytical, numerical, and experimental techniques, the chapter highlights the potential of modern stent designs to address clinical challenges effectively. A comparative analysis of manufacturing methods—including braiding, laser cutting, and AM—offers a roadmap for future innovations in stent development, balancing mechanical performance, clinical efficacy, and cost-effectiveness.

3.6.1 Key findings

Braiding Techniques

- Braided stents demonstrate excellent flexibility and adaptability to complex vascular geometries. The chapter focused on optimizing braided stent designs using analytical modelling, FE analysis, and the MOPSO algorithm.
- Analytical modelling validated against reference FE data showed excellent agreement in terms of stent length, radial force, and stress parameters

(subsection 3.2.4). Using the MOPSO algorithm, optimal design parameters—including wire diameter, number of coils, and braided angle—were identified.

- The optimization results revealed significant improvements, with a 28% increase in radial force, a 40% boost in radial pressure stiffness, and a 4.6% reduction in length variation compared to reference design. These advancements highlight the precision and enhanced fatigue performance of the optimized braided stent, establishing it as a viable solution for tortuous and dynamic vessel regions.

Laser-Cutting Techniques

- The Scitech-Solaris stent was used as a case study to examine the capabilities of laser-cutting methods. The superelastic behavior of the stent, derived from experimental testing (discussed in subsection 3.3.4), validates its performance under physiological conditions.
- Despite their scalability and reliable surface finishes, laser-cut stents face limitations such as geometric constraints (e.g., rectangular cross-sections), which can disrupt blood flow and increase restenosis risk. These limitations underscore the need for more customizable manufacturing methods.

Additive Manufacturing (AM)

- AM techniques offer unparalleled customization potential, enabling the design of patient-specific stents with complex geometries, such as bifurcated or auxetic structures.
- However, challenges like anisotropic mechanical properties, high surface roughness, and process sensitivity to material composition pose barriers to widespread adoption. The results discussed in section 3.4 emphasize the importance of post-processing techniques like chemical etching and heat treatments to overcome these limitations.

The following table provides a concise summary of the advantages and disadvantages associated with the three primary manufacturing methods discussed in this chapter.

Table 14. Comparison of advantages and disadvantages of key manufacturing methods for self-expanding NiTi stents.

Manufacturing methods	**Advantages**	**Disadvantages**
Braiding	Provides flexibility and good radial strength due to interwoven wires. Capable of producing stents with varying geometries. Generally good biocompatibility with materials used.	Limited customization compared to other methods. Complexity in manufacturing may lead to inconsistencies.
Laser-cutting	Established process with reliable outcomes for mass production. Efficient for standard sizes and shapes, ensuring quick production. Good surface finish achievable through post-processing techniques.	Produces rectangular cross-sections that can promote blood flow turbulence, increasing risks of restenosis. Limited customization for specific patient needs; relies on available tube sizes. Rectangular cross-sections might increase restenosis risk by disrupting blood flow dynamics. Tool wear can affect dimensional accuracy; requires careful handling of material properties.
Additive manufacturing	Allows for fully customizable stents tailored to patient-specific anatomies using 3D models. Minimizes waste during production compared to traditional methods like laser cutting. Enables complex geometries, including bifurcated, and auxetic designs, which are challenging for other methods. Eliminates reliance on commercially available tube sizes by enabling variable diameter design. Affordable for rapid prototyping and iterative design development.	Low surface quality of as-built parts, requiring additional finishing processes like chemical etching. Anisotropic mechanical properties may lead to inconsistent performance based on printing orientation. Sensitivity to powder composition and process settings can affect mechanical properties and SE. Requires precise control of process parameters like laser power, scanning speed, and layer thickness, making the process complex. High initial costs due to specialized equipment and materials.

3.6.2 Implications for future stent design

The insights presented in this chapter set the foundation for the next generation of stents that prioritize adaptability, reliability, and patient-specific solutions.

Optimized braided stents demonstrate the potential to meet clinical challenges in tortuous vessels, while laser-cutting and AM techniques offer complementary strengths for scalable, customizable, and patient-specific production. AM, in particular, enables the creation of stents with complex geometries and tailored dimensions, making it ideal for addressing unique anatomical and pathological needs. Future advancements will require a balanced integration of these methods, leveraging the benefits of each to design stents that excel in both mechanical performance and clinical outcomes. By combining innovative manufacturing processes with rigorous optimization techniques, the development of highly customized stents capable of improving patient-specific treatments becomes increasingly feasible.

Chapter 4: Conclusion

This thesis focuses on the application of NiTi in both engineering and medical fields. It begins by discussing the fundamental characteristics of NiTi, particularly its SME and SE properties and highlights their critical roles in enhancing the performance and functionality of actuators and medical devices like stents.

In the domain of actuators, we proposed and developed a novel SMA-metamaterial actuator capable of exhibiting a reversible, global elongation in multiple directions induced by the unidirectional contraction upon heating of a single SMA component. This actuator consists of: (i) an SMA component, (ii) a bias component, and (iii) the metamaterial geometry, each having a distinct function: (i) actuation activation, (ii) reversibility of actuation upon deactivation, and (iii) amplifying and redirecting the unidirectional SMA actuation globally throughout the actuator, respectively. We designed and tested a prototype actuator in various configurations over multiple activation/deactivation cycles to demonstrate the functionality and reusability of this system. Furthermore, we developed and validated a theoretical model predicting the actuation stroke of the system based on the material properties of the SMA and bias components, as well as the geometry of the metamaterial system. The findings of this work demonstrate the considerable potential of SMA-metamaterial actuators for implementation in systems requiring a multi-axial actuation output.

In the realm of biomedical engineering, the thesis details the evolution of stents, their classification, and the critical factors influencing their performance, such as material properties, design geometry, and manufacturing techniques. To provide a comprehensive understanding, this work classifies and examines each manufacturing technique through case studies: starting with the design and optimization of a SX braided stent, followed by the analysis of a laser-cut stent, and concluding with a discussion on stent fabrication using AM, including the challenges and opportunities associated with AM techniques.

We studied the design and optimization of a SX NiTi braided stent using analytical and numerical models. The analytical model was validated by comparing the results with reference data obtained from a literature study using FE. The comparison showed excellent agreement between the analytical model and the reference data in terms of stent length, radial force, and stress parameters. Subsequently, we used MOPSO to improve the stent design by exploring three important design variables: wire diameter, number of coils, and braided angle. The objective of the optimization procedure was to improve the radial stiffness and radial force of the stent while minimizing the length variation of the stent under loading. The optimization effectively identified optimal parameters with substantial improvements over the reference device. In comparison to the reference design, the findings show that the optimized design significantly boosts the stent's mechanical properties by 28% and 40% in terms of average radial force and radial pressure stiffness, respectively. In addition, the length variation of the optimized stent decreased by 4.6%, demonstrating enhanced stent deployment precision. The optimized stent also showed a significant diameter variation with a local strain below 0.5% within the elastic limit of the material, ensuring high fatigue performance. Overall, the analytical and numerical models we described in this study proved effective at predicting stent behavior and designing optimal stent geometry with enhanced mechanical properties.

Continuing with laser-cut stents, the thesis examines the SX NiTi Scitech-Solaris as a case study to demonstrate its design and superelastic behavior. First, we obtained precise dimensional measurements of the stent using microscopic imaging and incorporated them into a CAD model created in SolidWorks, which we later imported into ABAQUS for simulation. Then, the material behavior of the NiTi used in the stent was modelled based on the superelastic properties, employing an iterative trial-and-error process that combined CR experimental data with FEM simulations to adjust the model’s parameters. We successfully simulated the CR test, replicating the experimental conditions with a high degree of accuracy, as evidenced by the close alignment between simulation results and experimental data.

Finally, this thesis explores the potential of AM, particularly laser-based powder bed fusion, as a transformative method for producing patient-specific stents with intricate geometries. We demonstrated that while AM offers significant advantages, such as design flexibility and waste minimization, it also presents challenges, including surface quality and porosity control. We showed that optimizing AM process parameters, along with post-processing techniques like chemical etching, is critical in addressing these challenges.

In conclusion, this thesis contributes to advancing the field of NiTi-based devices through innovative design, rigorous testing, and optimization. By bridging the gap between theoretical understanding and real-world application, this work underscores the transformative potential of NiTi in engineering and medicine.

Chapter 5: References

[1] N. El-Bagoury, M.M. Hessien, Z.I. Zaki, Influence of aging on microstructure, martensitic transformation and mechanical properties of NiTiRe shape memory alloy, Metals and Materials International 20 (2014) 997–1002. https://doi.org/10.1007/s12540-014-5003-0.

[2] S. Hellberg, J. Hummel, P. Krooß, T. Niendorf, S. Böhm, Microstructural and mechanical properties of dissimilar nitinol and stainless steel wire joints produced by micro electron beam welding without filler material, Welding in the World 64 (2020) 2159–2168. https://doi.org/10.1007/s40194-020-00991-3.

[3] E. Augusto, A. Tarquino, Structural fatigue of superelastic NiTi wires, n.d. https://tel.archives-ouvertes.fr/tel-01871232.

[4] S.F. Hoseini, S.A. MirMohammadSadeghi, A. Fathi, H.M. Daniali, Adaptive predictive control of a novel shape memory alloy rod actuator, Proceedings of the Institution of Mechanical Engineers. Part I: Journal of Systems and Control Engineering 235 (2021) 291–301. https://doi.org/10.1177/0959651820974488.

[5] M. Wang, S. Jiang, Y. Zhang, Phase transformation, twinning, and detwinning of NiTi shape-memory alloy subject to a shock wave based on molecular-dynamics simulation, Materials 11 (2018). https://doi.org/10.3390/ma11112334.

[6] E. Kaya, İ. Kaya, Investigation of high speed cutting performance and phase transformation behavior of NiTi shape memory alloys, International Journal of Advanced Manufacturing Technology 119 (2022) 489–502. https://doi.org/10.1007/s00170-021-08254-1.

[7] B. He, X. Dong, R. Nie, Y. Wang, S. Ao, G. Wang, Comprehensive shape memory alloys constitutive models for engineering application, Mater Des 225 (2023) 111563. https://doi.org/10.1016/J.MATDES.2022.111563.

[8] Z. Zainal Abidin, P. Tarisai Mativenga, G. Harrison, Chilled Air System and Size Effect in Micro-milling of Nickel−Titanium Shape Memory Alloys, International Journal of Precision Engineering and Manufacturing - Green Technology 7 (2020) 283–297. https://doi.org/10.1007/s40684-019-00040-5.

[9] S. Alipour, F. Taromian, E.R. Ghomi, M. Zare, S. Singh, S. Ramakrishna, Nitinol: From historical milestones to functional properties and biomedical applications, Proc Inst Mech Eng H 236 (2022) 1595–1612. https://doi.org/10.1177/09544119221123176.

[10] H. Ishii, K.L. Ting, SMA actuated compliant bistable mechanisms, Mechatronics 14 (2004) 421–437. https://doi.org/10.1016/S0957-4158(03)00068-0.

[11] D. Reynaerts, H. Van Brussel, Design aspects of shape memory actuators, Mechatronics 8 (1998) 635–656. https://doi.org/10.1016/S0957-4158(98)00023-3.

[12] A. Nespoli, S. Besseghini, S. Pittaccio, E. Villa, S. Viscuso, The high potential of shape memory alloys in developing miniature mechanical devices: A review on shape memory alloy mini-actuators, Sens Actuators A Phys 158 (2010) 149–160. https://doi.org/10.1016/j.sna.2009.12.020.

[13] A. Spaggiari, G. Scirè Mammano, E. Dragoni, Optimum Mechanical Design of Binary Actuators Based on Shape Memory Alloys, Chapter in “Smart Actuation and Sensing Systems - Recent Advances and Future Challenges” Intech Publisher 1 (2012) 3–34. https://doi.org/10.5772/2760.

[14] S. Alipour, F. Taromian, E.R. Ghomi, M. Zare, S. Singh, S. Ramakrishna, Nitinol: From historical milestones to functional properties and biomedical applications, Proc Inst Mech Eng H 236 (2022) 1595–1612. https://doi.org/10.1177/09544119221123176.

[15] F.E. Wang, W.J. Buehler, S.J. Pickart, Crystal structure and a unique martensitic transition of TiNi, J Appl Phys 36 (1965) 3232–3239.

[16] D.S. Ford, S.R. White, Thermomechanical Behavior of 55Ni45Ti Nitinol, Acta Mater 44 (1996) 2295–2307.

[17] M.J. Mahtabi, N. Shamsaei, M.R. Mitchell, Fatigue of Nitinol: The state-of-the-art and ongoing challenges, J Mech Behav Biomed Mater 50 (2015) 228–254.

[18] S.W. Robertson, A.R. Pelton, R.O. Ritchie, Mechanical fatigue and fracture of Nitinol, International Materials Reviews 57 (2012) 1–37.

[19] A.R. Pelton, Nitinol fatigue: A review of microstructures and mechanisms, J Mater Eng Perform 20 (2011) 613–617.

[20] K. Maleckis, E. Anttila, P. Aylward, W. Poulson, A. Desyatova, J. MacTaggart, A. Kamenskiy, Nitinol Stents in the Femoropopliteal Artery: A Mechanical Perspective on Material, Design, and Performance, Ann Biomed Eng 46 (2018) 684–704. https://doi.org/10.1007/s10439-018-1990-1.

[21] M. Elahinia, N. Shayesteh Moghaddam, M. Taheri Andani, A. Amerinatanzi, B.A. Bimber, R.F. Hamilton, Fabrication of NiTi through additive manufacturing: A review, Prog Mater Sci 83 (2016) 630–663. https://doi.org/10.1016/J.PMATSCI.2016.08.001.

[22] A. Solis Eichler, Mechanical and Material Properties of Nitinol and its Application to Stents, Master’s degree thesis, Florida Institute of Technology, 2020. https://repository.fit.edu/etd.

[23] S.W. Robertson, On the mechanical properties and microstructure of Nitinol for biomedical stent applications, PhD thesis, University of California, Berkeley, 2006.

[24] D. Kapoor, Nitinol for Medical Applications: A Brief Introduction to the Properties and Processing of Nickel Titanium Shape Memory Alloys and their Use in Stents, Johnson Matthey Technology Review 61 (2017) 66–76. https://doi.org/10.1595/205651317X694524.

[25] C. Youyi, Z. Ming, Y. Fengzhi, Orthodontic Application of NiTi Shape-Memory Alloy in China, n.d.

[26] D.C. Lagoudas, Shape Memory Alloys, Springer US, Boston, MA, 2008. https://doi.org/10.1007/978-0-387-47685-8.

[27] J. Mohd Jani, M. Leary, A. Subic, M.A. Gibson, A review of shape memory alloy research, applications and opportunities, Mater Des 56 (2014) 1078–1113. https://doi.org/10.1016/j.matdes.2013.11.084.

[28] L. Sun, W.M. Huang, Z. Ding, Y. Zhao, C.C. Wang, H. Purnawali, C. Tang, Stimulus-responsive shape memory materials: A review, Mater Des 33 (2012) 577–640. https://doi.org/10.1016/j.matdes.2011.04.065.

[29] A. Spaggiari, D. Castagnetti, N. Golinelli, E. Dragoni, G. Scire Mammano, Smart materials: Properties, design and mechatronic applications, Proceedings of the Institution of Mechanical Engineers, Part L: Journal of Materials:

Design and Applications 0 (2016) 1–29. https://doi.org/10.1177/1464420716673671.
[30] L. Mizzi, A. Spaggiari, E. Dragoni, Design-oriented modelling of composite actuators with embedded shape memory alloy, Compos Struct 213 (2019) 37–46. https://doi.org/10.1016/j.compstruct.2019.01.057.
[31] A. Rao, A.R. Srinivasa, J.N. Reddy, Design of Shape Memory Alloy (SMA) Actuators, 2015.
[32] P. Ghosh, A. Rao, A.R. Srinivasa, Design of multi-state and smart-bias components using Shape Memory Alloy and Shape Memory Polymer composites, Mater Des 44 (2013) 164–171. https://doi.org/10.1016/j.matdes.2012.05.063.
[33] A. Spaggiari, E. Dragoni, Analytical and numerical modeling of shape memory alloy Negator springs for constant-force, long-stroke actuators, J Intell Mater Syst Struct 25 (2014) 1139–1148. https://doi.org/10.1177/1045389X13493354.
[34] P. Bettini, M. Riva, G. Sala, L. Di Landro, A. Airoldi, J. Cucco, Carbon fiber reinforced smart laminates with embedded SMA actuators-part I: Embedding techniques and interface analysis, J Mater Eng Perform 18 (2009) 664–671. https://doi.org/10.1007/s11665-009-9384-z.
[35] C. Simoneau, P. Terriault, S. Lacasse, V. Brailovski, Adaptive composite panel with embedded SMA actuators: Modeling and validation, Mechanics Based Design of Structures and Machines 42 (2014) 174–192. https://doi.org/10.1080/15397734.2013.864246.
[36] C. Renata, W.M. Huang, L.W. He, J.J. Yang, Shape change/memory actuators based on shape memory materials, Journal of Mechanical Science and Technology 31 (2017) 4863–4873. https://doi.org/10.1007/s12206-017-0934-2.
[37] S. Pappada, P. Gren, K. Tatar, T. Gustafson, R. Rametta, E. Rossini, A. Maffezzoli, Mechanical and Vibration Characteristics of Laminated Composite Plates Embedding Shape Memory Alloy Superelastic Wires, J Mater Eng Perform 18 (2009) 531–537. https://doi.org/10.1007/s11665-009-9403-0.
[38] G. Scirè Mammano, E. Dragoni, Increasing stroke and output force of linear shape memory actuators by elastic compensation, Mechatronics 21 (2011) 570–580. https://doi.org/10.1016/j.mechatronics.2011.02.005.
[39] N.V. Viet, W. Zaki, Bending model for a laminated composite cantilever beam with multiple embedded shape memory alloy layers presenting tensile compressive asymmetry, Compos Struct 1 (2019) 111410.
[40] M.L. Dezaki, M. Bodaghi, A. Serjouei, S. Afazov, A. Zolfagharian, Adaptive reversibile composite-based shape memory alloy soft actuators, Sens Actuators A Phys 345 (2022) 113779.
[41] M.N. Zadeh, M. Garrad, C. Romero, A. Conn, F. Scarpa, J. Rossiter, RoboHeart: A bi-directional zipping actuator, IEEE Robot Autom Lett 7 (2022) 10352–10358.
[42] S. John, M. Hariri, Effect of shape memory alloy actuation on the dynamic response of polymeric composite plates, Compos Part A Appl Sci Manuf 39 (2008) 769–776.
[43] D. Quade, S. Jana, G. Morscher, M. Kannan, L. McCorkle, The effects of fiber orientation and adhesives on tensile properties of carbon fiber reinforced

polymer matrix composite with embedded nickel-titanium shape memory alloys, Compos Part A Appl Sci Manuf 114 (2018) 269–277.

[44] Z.K. Lu, G.J. Weng, A two-level micromechanical theory for a shape-memory alloy reinforced composite, Int J Plast 16 (2000) 1289–1307.

[45] H.K. Cho, J. Rhee, Nonlinear finite element analysis of shape memory alloy (SMA) wire reinforced hybrid laminate composite shells, Int J Non Linear Mech 47 (2012) 672–678. https://doi.org/10.1016/j.ijnonlinmec.2011.11.002.

[46] V. Birman, Stability of functionally graded shape memory alloy sandwich panels, Smart Mater Struct 6 (1997) 278–286.

[47] A. Ghaznavi, M. Shariyat, Non-linear layerwise dynamic response analysis of sandwich plates with soft auxetic cores and embedded SMA wires experiencing cyclic loadings, Compos Struct 171 (2017) 185–197. https://doi.org/10.1016/j.compstruct.2017.03.012.

[48] S.M.R. Khalili, M.B. Dehkordi, E. Carrera, M. Shariyat, Non-linear dynamic analysis of a sandwich beam with pseudoelastic SMA hybrid composite faces based on higher order finite element theory, Compos Struct 96 (2013) 243–255. https://doi.org/10.1016/j.compstruct.2012.08.020.

[49] L. Mizzi, A. Spaggiari, E. Dragoni, Design of shape memory alloy sandwich actuators: an analytical and numerical modelling approach, Smart Mater Struct 29 (2020) 085027.

[50] M.B. Dehkordi, S.M.R. Khalili, Frequency analysis of sandwich plate with active SMA hybrid composite face-sheets and temperature dependent flexible core, Compos Struct 123 (2015) 408–419. https://doi.org/10.1016/j.compstruct.2014.12.068.

[51] E. Montgomery-Liljeroth, S. Schievano, G. Burriesci, Elastic properties of 2D auxetic honeycomb structures- a review, Appl Mater Today 30 (2023). https://doi.org/10.1016/j.apmt.2022.101722.

[52] J.N. Grima, K.E. Evans, Auxetic behavior from rotating squares, J Mater Sci Lett 19 (2000) 1563–1565.

[53] J.N. Grima, A. Alderson, K.E. Evans, Negative Poisson’s ratios from rotating rectangles, Computational Methods in Science and Technology 10 (2004) 137–145.

[54] J.N. Grima, R. Gatt, A. Alderson, K.E. Evans, On the auxetic properties of ‘rotating rectangles’ with different connectivity, J Physical Soc Japan 74 (2005) 2866–2867.

[55] D. Attard, J.N. Grima, Auxetic Behavior from rotating rhombi, Physica Status Solidi (B) 245 (2008) 2395–2404. https://doi.org/10.1002/pssb.200880269.

[56] D. Attard, E. Manicaro, J.N. Grima, On rotating rigid parallelograms and their potential for exhibiting auxetic Behavior, Physica Status Solidi B 2044 (2009) 2033–2044. https://doi.org/10.1002/pssb.200982034.

[57] L. Mizzi, K.M. Azzopardi, D. Attard, J.N. Grima, R. Gatt, Auxetic metamaterials exhibiting giant negative Poisson’s ratios, Physica Status Solidi - Rapid Research Letters 9 (2015) 425–430. https://doi.org/10.1002/pssr.201510178.

[58] J.N. Grima, K.E. Evans, Auxetic behavior from rotating triangles, J Mater Sci 1 (2006) 3193–3196. https://doi.org/10.1007/s10853-006-6339-8.

[59] J.N. Grima, E. Chetcuti, E. Manicaro, D. Attard, R. Gatt, K.E. Evans, On the auxetic properties of generic rotating rigid triangles On the auxetic properties of generic rotating, (2012). https://doi.org/10.1098/rspa.2011.0273.

[60] D. Attard, J.N. Grima, A three-dimensional rotating rigid units network exhibiting negative Poisson's ratios, Physica Status Solidi (B) 249 (2012) 1330–1338.

[61] X. Ren, J. Shen, A. Ghaedizadeh, H. Tian, Y.M. Xie, Experiments and parametric studies on 3D metallic auxetic metamaterials with tuneable mechanical properties, Smart Mater Struct 24 (2015) 095016. https://doi.org/10.1088/0964-1726/24/9/095016.

[62] B.K. Bertoldi, P.M. Reis, S. Willshaw, T. Mullin, Negative Poisson ' s Ratio Behavior Induced by an Elastic Instability, Adv Funct Mater (2009) 1–6. https://doi.org/10.1002/adma.200901956.

[63] M. Taylor, L. Francesconi, M. Gerendás, A. Shanian, C. Carson, Low Porosity Metallic Periodic Structures with Negative Poisson ' s Ratio, (2013). https://doi.org/10.1002/adma.201304464.

[64] L. Mizzi, R. Gatt, J.N. Grima, Non-porous grooved single-material auxetics, Physica Status Solidi B 252 (2015) 1559–1564. https://doi.org/10.1002/pssb.201552218.

[65] L. Mizzi, E. Salvati, A. Spaggiari, J. Tan, A.M. Korsunsky, 2D auxetic metamaterials with tuneable micro-/nanoscale apertures, Appl Mater Today 20 (2020) 100780. https://doi.org/10.1016/j.apmt.2020.100780.

[66] A.C. Souza, E.N. Mamiya, N. Zouain, Three-dimensional model for solids undergoing stress-induced phase transformations, European Journal of Mechanics, A/Solids 17 (1998) 789–806. https://doi.org/10.1016/S0997-7538(98)80005-3.

[67] F. Auricchio, L. Petrini, Improvements and algorithmical considerations on a recent three-dimensional model describing stress-induced solid phase transformations, Int J Numer Methods Eng 55 (2002) 1255–1284. https://doi.org/10.1002/nme.619.

[68] F. Auricchio, L. Petrini, A three-dimensional model describing stress-temperature induced solid phase transformations: Solution algorithm and boundary value problems, Int J Numer Methods Eng 61 (2004) 807–836. https://doi.org/10.1002/nme.1086.

[69] R. Panciroli, Influence of electric current on the thermo-mechanical static and fatigue properties of shape memory NiTi wires, Smart Mater Struct 29 (2020) 115046.

[70] H. Cho, T. Yamamoto, Y. Takeda, A. Suzuki, T. Sakuma, Exploitation of shape memory alloy actuator using resistance feedback control and its development, Progress in Natural Science: Materials International 20 (2010) 97–103. https://doi.org/10.1016/S1002-0071(12)60013-6.

[71] L. Mizzi, A. Spaggiari, Lightweight mechanical metamaterials designed using hierarchical truss elements, Smart Mater Struct 29 (2020) 105036.

[72] S.Q. Khan, P.F. Ludman, Percutaneous coronary intervention, Medicine (United Kingdom) 50 (2022) 437–444. https://doi.org/10.1016/j.mpmed.2022.04.008.

[73] H. Bjarnason, Venoplasty and Stenting, in: Handbook of Angioplasty and Stenting Procedures, Springer London, 2010: pp. 303–315. https://doi.org/10.1007/978-1-84800-399-6_23.

[74] A. Desyatova, W. Poulson, P. Deegan, C. Lomneth, A. Seas, K. Maleckis, J. MacTaggart, A. Kamenskiy, Limb flexion-induced twist and associated intramural stresses in the human femoropopliteal artery, J R Soc Interface 14 (2017). https://doi.org/10.1098/rsif.2017.0025.

[75] I. Ohkata, Medical applications of superelastic nickel-titanium (Ni–Ti) alloys, Woodhead Publishing Limited, 2011. https://doi.org/10.1533/9780857092625.3.176.

[76] C.T. Dotter, Transluminally-placed coilspring endarterial tube grafts, Invest Radiol 4 (1969) 329–332.

[77] C.T. Dotter, R.W. Buschmann, montgomery K. McKinney, Rösch Josef, Transluminal Expandable Nitinol Coil Stent Grafting: Preliminary Report, Radiology 147 (1983) 259–260.

[78] M.M. Payne, Charles Theodore Dotter - The father of intervention, Historical Perspectives (2001).

[79] F. Ahadi, M. Azadi, M. Biglari, M. Bodaghi, A. Khaleghian, Evaluation of coronary stents: A review of types, materials, processing techniques, design, and problems, Heliyon 9 (2023) e13575. https://doi.org/10.1016/J.HELIYON.2023.E13575.

[80] C. Pan, Y. Han, J. Lu, Structural design of vascular stents: A review, Micromachines (Basel) 12 (2021). https://doi.org/10.3390/mi12070770.

[81] C. McCormick, Overview of cardiovascular stent designs, in: Functionalised Cardiovascular Stents, Elsevier, 2017: pp. 3–26. https://doi.org/10.1016/B978-0-08-100496-8.00001-9.

[82] A. Kapoor, N. Jepson, N.W. Bressloff, P.H. Loh, T. Ray, S. Beier, The road to the ideal stent: A review of stent design optimisation methods, findings, and opportunities, Mater Des 237 (2024) 112556. https://doi.org/10.1016/J.MATDES.2023.112556.

[83] M.S. Lee, G. Banka, In-stent Restenosis, Interv Cardiol Clin 5 (2016) 211–220. https://doi.org/10.1016/J.ICCL.2015.12.006.

[84] S.H. Im, D.H. Im, S.J. Park, Y. Jung, D.H. Kim, S.H. Kim, Current status and future direction of metallic and polymeric materials for advanced vascular stents, Prog Mater Sci 126 (2022). https://doi.org/10.1016/j.pmatsci.2022.100922.

[85] G. Tepe, R. Bantleon, K. Brechtel, J. Schmehl, T. Zeller, C.D. Claussen, F.F. Strobl, Management of peripheral arterial interventions with mono or dual antiplatelet therapy-the MIRROR study: A randomised and double-blinded clinical trial, Eur Radiol 22 (2012) 1998–2006. https://doi.org/10.1007/S00330-012-2441-2/TABLES/5.

[86] P.J. Geraghty, M.W. Mewissen, M.R. Jaff, G.M. Ansel, Three-year results of the VIBRANT trial of VIABAHN endoprosthesis versus bare nitinol stent implantation for complex superficial femoral artery occlusive disease, J Vasc Surg 58 (2013) 386-395.e4. https://doi.org/10.1016/J.JVS.2013.01.050.

[87] K. Miki, K. Fujii, M. Fukunaga, D. Kawasaki, M. Shibuya, T. Imanaka, H. Tamaru, M. Masutani, M. Ohyanagi, T. Masuyama, Impact of Post-Procedural Intravascular Ultrasound Findings on Long-Term Results Following Self-Expanding Nitinol Stenting in Superficial Femoral Artery Lesions, Circulation Journal 77 (2013) 1543–1550. https://doi.org/10.1253/CIRCJ.CJ-12-1182.

[88] F. Pecoraro, E. Dinoto, D. Pakeliani, D. Mirabella, F. Ferlito, G. Bajardi, Efficacy and one-year outcomes of Luminor® paclitaxel-coated drug-eluting balloon in the treatment of popliteal artery atherosclerosis lesions., Ann Vasc Surg 76 (2021) 370–377. https://doi.org/10.1016/J.AVSG.2021.04.015.

[89] D. Scheinert, S. Scheinert, J. Sax, C. Piorkowski, S. Bräunlich, M. Ulrich, G. Biamino, A. Schmidt, Prevalence and clinical impact of stent fractures after

femoropopliteal stenting, J Am Coll Cardiol 45 (2005) 312–315. https://doi.org/10.1016/J.JACC.2004.11.026.
[90] M. Intaglietta, Vasomotion and flowmotion: physiological mechanisms and clinical evidence, Vascular Medicine Review 1 (1990) 101–112.
[91] Y. Sotomi, Y. Onuma, C. Collet, E. Tenekecioglu, R. Virmani, N.S. Kleiman, P.W. Serruys, Bioresorbable Scaffold - The Emerging Reality and Future Directions, Circ Res 120 (2017) 1341–1352. https://doi.org/10.1161/circresaha.117.310275.
[92] A.R. Pelton, V. Schroeder, M.R. Mitchell, X.Y. Gong, M. Barney, S.W. Robertson, Fatigue and durability of Nitinol stents, J Mech Behav Biomed Mater 1 (2008) 153–164. https://doi.org/10.1016/J.JMBBM.2007.08.001.
[93] T.W. Duerig, M. Wholey, A comparison of balloon- and self-expanding stents, Minimally Invasive Therapy and Allied Technologies 11 (2002) 173–178. https://doi.org/10.1080/136457002760273386.
[94] G. Mani, M.D. Feldman, D. Patel, C.M. Agrawal, Coronary stents: A materials perspective, Biomaterials 28 (2007) 1689–1710. https://doi.org/10.1016/J.BIOMATERIALS.2006.11.042.
[95] A. Firoozi, B. Mohebbi, F. Noohi, H. Bassiri, A. Mohebbi, S. Abdi, M. Maleki, O. Shafe, M.M. Peighambari, M.J. Alemzadeh-Ansari, H. Bakhshandeh, Y. Rezaei, N. Sepehrvand, Self-Expanding Versus Balloon-Expandable Stents in Patients With Isthmic Coarctation of the Aorta, Am J Cardiol 122 (2018) 1062–1067. https://doi.org/10.1016/J.AMJCARD.2018.06.005.
[96] R. He, L.G. Zhao, V. V. Silberschmidt, H. Willcock, A computational study of fatigue resistance of nitinol stents subjected to walk-induced femoropopliteal artery motion, J Biomech 118 (2021) 110295. https://doi.org/10.1016/J.JBIOMECH.2021.110295.
[97] I. Avdeev, M. Shams, Vascular stents: Coupling full 3-D with reduced-order structural models, in: IOP Conf Ser Mater Sci Eng, Institute of Physics Publishing, 2014. https://doi.org/10.1088/1757-899X/10/1/012133.
[98] A.R. Saraf, S.P. Yadav, Fundamentals of bare-metal stents, Elsevier Ltd., 2017. https://doi.org/10.1016/B978-0-08-100496-8.00002-0.
[99] T. Hanawa, Materials for metallic stents, Journal of Artificial Organs 12 (2009) 73–79. https://doi.org/10.1007/s10047-008-0456-x.
[100] R.B. Heimann, Materials for medical application, Materials for Medical Application (2020) 1–615. https://doi.org/10.1515/9783110619249.
[101] C. Shanahan, P. Tiernan, S.A.M. Tofail, Looped ends versus open ends braided stent: A comparison of the mechanical Behavior using analytical and numerical methods, J Mech Behav Biomed Mater 75 (2017) 581–591. https://doi.org/10.1016/J.JMBBM.2017.08.025.
[102] S.F. Hoseini, A. Spaggiari, Design and Optimization of a Self-Expandable Niti Braided Stent Using MOPSO Algorithm, X ECCOMAS Thematic Conference on Smart Structures and Materials, SMART 2023 (2023) 454–464. https://doi.org/10.7712/150123.9800.449429.
[103] N. Sabahi, W. Chen, C.H. Wang, J.J. Kruzic, X. Li, A Review on Additive Manufacturing of Shape-Memory Materials for Biomedical Applications, JOM 72 (2020) 1229–1253. https://doi.org/10.1007/S11837-020-04013-X/FIGURES/13.

[104] D. Stoeckel, A. Pelton, T. Duerig, Self-expanding Nitinol stents: Material and design considerations, Eur Radiol 14 (2004) 292–301. https://doi.org/10.1007/s00330-003-2022-5.

[105] A. Tuissi, S. Carr, J. Butler, A.A. Gandhi, L. O'Donoghue, K. McNamara, J.M. Carlson, S. Lavelle, P. Tiernan, C.A. Biffi, P. Bassani, S.A.M. Tofail, Radiopaque Shape Memory Alloys: NiTi–Er with Stable Superelasticity, Shape Memory and Superelasticity 2 (2016) 196–203. https://doi.org/10.1007/s40830-016-0066-z.

[106] B. Lin, K. Gall, H.J. Maier, R. Waldron, Structure and thermomechanical behavior of NiTiPt shape memory alloy wires, Acta Biomater 5 (2009) 257–267. https://doi.org/https://doi.org/10.1016/j.actbio.2008.07.015.

[107] J.-S. Park, K.H. Yim, S. Jeong, D.H. Lee, D.G. Kim, A Novel High-Visibility Radiopaque Tantalum Marker for Biliary Self-Expandable Metal Stents, Gut Liver 13 (2019) 366–372. https://doi.org/10.5009/gnl18330.

[108] A. Bramucci, A. Fontana, C.B. Massoni, E. Vecchiati, A. Freyrie, N. Tusini, Dual- vs single-layer stents for endovascular treatment of symptomatic and asymptomatic internal carotid artery stenosis, Cardiovascular Revascularization Medicine 57 (2023) 34–40. https://doi.org/10.1016/J.CARREV.2023.06.016.

[109] Guidance for Industry and FDA Staff, Non-Clinical Engineering Tests and Recommended Labeling for Intravascular Stents and Associated Delivery Systems, 2010. http://www.fda.gov/MedicalDevices/DeviceRegulationandGuidance/GuidanceDocuments/ucm0.

[110] D.E. Kiousis, A.R. Wulff, G.A. Holzapfel, Experimental studies and numerical analysis of the inflation and interaction of vascular balloon catheter-stent systems, Ann Biomed Eng 37 (2009) 315–330. https://doi.org/10.1007/s10439-008-9606-9.

[111] A.G. Verstandig, A.I. Bloom, T. Sasson, Y.S. Haviv, D. Rubinger, Shortening and migration of Wallstents after stenting of central venous stenoses in hemodialysis patients, Cardiovasc Intervent Radiol 26 (2003) 58–64. https://doi.org/10.1007/S00270-002-1953-6/METRICS.

[112] P.K.M. Prithipaul, M. Kokkolaras, D. Pasini, Assessment of structural and hemodynamic performance of vascular stents modelled as periodic lattices, Med Eng Phys 57 (2018) 11–18. https://doi.org/10.1016/J.MEDENGPHY.2018.04.017.

[113] R. Improta, P. Scarparo, J. Wilschut, Q. Wolff, J. Daemen, W.K. Den Dekker, F. Zijlstra, N.M. Van Mieghem, R. Diletti, Elastic stent recoil in coronary total occlusions: Comparison of durable-polymer zotarolimus eluting stent and ultrathin strut bioabsorbable-polymer sirolimus eluting stent, Catheterization and Cardiovascular Interventions 99 (2022) 88–97. https://doi.org/10.1002/ccd.29739.

[114] N.C. Liu, Robust optimisation of Coronary Stents, PhD thesis, The University of Sydney, 2022.

[115] L. Wiesent, U. Schultheiß, C. Schmid, T. Schratzenstaller, A. Nonn, Experimentally validated simulation of coronary stents considering different dogboning ratios and asymmetric stent positioning, PLoS One 14 (2019). https://doi.org/10.1371/journal.pone.0224026.

[116] M.R. Jedwab, C.O. Clerc, A study of the geometrical and mechanical properties of a self-expanding metallic stent--theory and experiment, Journal

of Applied Biomaterials 4 (1993) 77–85. https://doi.org/10.1002/jab.770040111.

[117] W. Schmidt, C. Brandt-Wunderlich, P. Behrens, C. Kopetsch, K.P. Schmitz, J.R. Andresen, N. Grabow, Revisiting SFA stent technology: an updated overview on mechanical stent performance, Biomedizinische Technik 68 (2023) 523–535. https://doi.org/10.1515/bmt-2022-0412.

[118] K. Maleckis, P. Deegan, W. Poulson, C. Sievers, A. Desyatova, J. MacTaggart, A. Kamenskiy, Comparison of femoropopliteal artery stents under axial and radial compression, axial tension, bending, and torsion deformations, J Mech Behav Biomed Mater 75 (2017) 160–168. https://doi.org/10.1016/j.jmbbm.2017.07.017.

[119] M.T. Vote, J.M. Hendriks, J.H.H. Van Laanen, P.M.T. Pattynama, B.E. Muhs, D. Poldermans, H.J.M. Verhagen, Radial Force Measurements in Carotid Stents: Influence of Stent Design and Length of the Lesion, Journal of Vascular and Interventional Radiology 22 (2011) 661–666. https://doi.org/10.1016/J.JVIR.2011.01.450.

[120] E. Dragoni, D. Castagnetti, A. Spaggiari, Lezioni di Costruzione di Macchine, Società Editrice Esculapio, 2023.

[121] D. Bin Kim, H. Choi, S.M. Joo, H.K. Kim, J.H. Shin, M.H. Hwang, J. Choi, D.G. Kim, K.H. Lee, C.H. Lim, S.K. Yoo, H.M. Lee, K. Sun, A Comparative Reliability and Performance Study of Different Stent Designs in Terms of Mechanical Properties: Foreshortening, Recoil, Radial Force, and Flexibility, Artif Organs 37 (2013) 368–379. https://doi.org/10.1111/aor.12001.

[122] Y. Liu, J. Yang, Y. Zhou, J. Hu, Structure Design of Vascular Stents, in: Multiscale Simulations and Mechanics of Biological Materials, John Wiley and Sons, 2013: pp. 301–317. https://doi.org/10.1002/9781118402955.ch16.

[123] M. Hejazi, F. Sassani, J. Gagnon, Y. Hsiang, A.S. Phani, Deformation mechanics of self-expanding venous stents: Modelling and experiments, J Biomech 120 (2021) 110333. https://doi.org/10.1016/J.JBIOMECH.2021.110333.

[124] C. Kleinstreuer, Z. Li, C.A. Basciano, S. Seelecke, M.A. Farber, Computational mechanics of Nitinol stent grafts, J Biomech 41 (2008) 2370–2378. https://doi.org/10.1016/J.JBIOMECH.2008.05.032.

[125] T.W. Tan, G.R. Douglas, T. Bond, A.S. Phani, Compliance and longitudinal strain of cardiovascular stents: Influence of cell geometry, Journal of Medical Devices, Transactions of the ASME 5 (2011) 1–6. https://doi.org/10.1115/1.4005226.

[126] E.J. Hearn, Mechanics of Materials 1 - An Introduction to the Mechanics of Elastic and Plastic Deformation of Solids and Structural Materials, Butterworth-Heinemann, 1997.

[127] S. Weiß, H. Szymczak, A. Meißner, Fatigue and endurance of coronary stents, Materwiss Werksttech 40 (2009) 61–64. https://doi.org/10.1002/mawe.200800409.

[128] H.Q. Zhao, A. Nikanorov, R. Virmani, R. Jones, E. Pacheco, L.B. Schwartz, Late stent expansion and neointimal proliferation of oversized nitinol stents in peripheral arteries, Cardiovasc Intervent Radiol 32 (2009) 720–726. https://doi.org/10.1007/s00270-009-9601-z.

[129] M. Bernini, M. Colombo, C. Dunlop, R. Hellmuth, C. Chiastra, W. Ronan, T.J. Vaughan, Oversizing of self-expanding Nitinol vascular stents – A biomechanical investigation in the superficial femoral artery, J Mech Behav

Biomed Mater 132 (2022) 105259. https://doi.org/10.1016/J.JMBBM.2022.105259.

[130] J. van Prehn, F.J.V. Schlösser, B.E. Muhs, H.J.M. Verhagen, F.L. Moll, J.A. van Herwaarden, Oversizing of Aortic Stent Grafts for Abdominal Aneurysm Repair: A Systematic Review of the Benefits and Risks, European Journal of Vascular and Endovascular Surgery 38 (2009) 42–53. https://doi.org/10.1016/J.EJVS.2009.03.025.

[131] Y. Qi, C. Weng, D. Yuan, T. Wang, Y. Ma, Y. Yang, J. Zhao, B. Huang, Oversizing Consideration of Proximal Stent Graft in Hemodynamically Stable and Unstable Patients Undergoing Emergent Endovascular Aortic Repair, J Clin Med 12 (2023) 7500. https://doi.org/10.3390/JCM12237500/S1.

[132] M.A.H. Taha, A. Busuttil, R. Bootun, B.A.H. Thabet, A.E.H. Badawy, H.A. Hassan, J. Shalhoub, A.H. Davies, Clinical outcomes and overview of dedicated venous stents for management of chronic iliocaval and femoral deep venous disease, Vascular 30 (2022) 320–330. https://doi.org/10.1177/1708538121989860.

[133] D. Dabir, A. Feisst, D. Thomas, J.A. Luetkens, C. Meyer, A. Kardulovic, M. Menne, U. Steinseifer, H.H. Schild, D.L.R. Kuetting, Physical Properties of Venous Stents: An Experimental Comparison, Cardiovasc Intervent Radiol 41 (2018) 942–950. https://doi.org/10.1007/s00270-018-1916-1.

[134] C. Brandt-Wunderlich, W. Schmidt, N. Grabow, M. Stiehm, S. Siewert, R. Andresen, K.P. Schmitz, Support function of self-expanding nitinol stents - Are radial resistive force and crush resistance comparable?, in: Current Directions in Biomedical Engineering, Walter de Gruyter GmbH, 2019: pp. 465–467. https://doi.org/10.1515/cdbme-2019-0117.

[135] J.C. Palmaz, Intravascular stents: Tissue-stent interactions and design considerations, American Journal of Roentgenology 160 (1993) 613–618. https://doi.org/10.2214/ajr.160.3.8430566.

[136] N.B. Morgan, Medical shape memory alloy applications—the market and its products, Materials Science and Engineering: A 378 (2004) 16–23. https://doi.org/10.1016/J.MSEA.2003.10.326.

[137] H.B. Smouse, A. Nikanorov, D. LaFlash, Biomechanical Forces in the Femoropopliteal Arterial Segment, Endovascular Today (2005) 60–66.

[138] J.N. MacTaggart, N.Y. Phillips, C.S. Lomneth, I.I. Pipinos, R. Bowen, B. Timothy Baxter, J. Johanning, G. Matthew Longo, A.S. Desyatova, M.J. Moulton, Y.A. Dzenis, A. V. Kamenskiy, Three-dimensional bending, torsion and axial compression of the femoropopliteal artery during limb flexion, J Biomech 47 (2014) 2249–2256. https://doi.org/10.1016/J.JBIOMECH.2014.04.053.

[139] E. Dordoni, A. Meoli, W. Wu, G. Dubini, F. Migliavacca, G. Pennati, L. Petrini, Fatigue Behavior of Nitinol peripheral stents: The role of plaque shape studied with computational structural analyses, Med Eng Phys 36 (2014) 842–849. https://doi.org/10.1016/j.medengphy.2014.03.006.

[140] M. Early, D.J. Kelly, The consequences of the mechanical environment of peripheral arteries for nitinol stenting, Med Biol Eng Comput 49 (2011) 1279–1288. https://doi.org/10.1007/s11517-011-0815-2.

[141] H. Cao, M.H. Wu, F. Zhou, R.M. McMeeking, R.O. Ritchie, The influence of mean strain on the high-cycle fatigue of Nitinol with application to medical devices, J Mech Phys Solids 143 (2020) 104057. https://doi.org/https://doi.org/10.1016/j.jmps.2020.104057.

[142] M. Pernot, G. Goudot, Noninvasive ultrafast ultrasound for imaging the coronary vasculature and assessing the arterial wall’s biomechanics, Biomechanics of Coronary Atherosclerotic Plaque: From Model to Patient (2021) 517–528. https://doi.org/10.1016/B978-0-12-817195-0.00022-6.

[143] C. Jenei, E. Balogh, G.T. Szabó, C.A. Dézsi, Z. Kőszegi, Wall shear stress in the development of in-stent restenosis revisited. A critical review of clinical data on shear stress after intracoronary stent implantation, Cardiol J 23 (2016) 365–373. https://doi.org/10.5603/CJ.a2016.0047.

[144] A.M. Malek, S.L. Alper, S. Izumo, Hemodynamic Shear Stress and Its Role in Atherosclerosis, JAMA 282 (1999) 2035–2042. https://doi.org/10.1001/jama.282.21.2035.

[145] A. Cornelissen, F.J. Vogt, The effects of stenting on coronary endothelium from a molecular biological view: Time for improvement?, J Cell Mol Med 23 (2019) 39–46. https://doi.org/10.1111/jcmm.13936.

[146] M. Sanmartín, J. Goicolea, C. García, J. García, A. Crespo, J. Rodríguez, J.M. Goicolea, Influence of Shear Stress on In-Stent Restenosis: In Vivo Study Using 3D Reconstruction and Computational Fluid Dynamics, Revista Española de Cardiología (English Edition) 59 (2006) 20–27. https://doi.org/10.1016/s1885-5857(06)60044-3.

[147] J.F. LaDisa, L.E. Olson, I. Guler, D.A. Hettrick, S.H. Audi, J.R. Kersten, D.C. Warltier, P.S. Pagel, Stent design properties and deployment ratio influence indexes of wall shear stress: a three-dimensional computational fluid dynamics investigation within a normal artery, J Appl Physiol 97 (2004) 424–430. https://doi.org/10.1152/japplphysiol.01329.2003.

[148] F. Gijsen, Y. Katagiri, P. Barlis, C. Bourantas, C. Collet, U. Coskun, J. Daemen, J. Dijkstra, E. Edelman, P. Evans, K. Van Der Heiden, R. Hose, B.K. Koo, R. Krams, A. Marsden, F. Migliavacca, Y. Onuma, A. Ooi, E. Poon, H. Samady, P. Stone, K. Takahashi, D. Tang, V. Thondapu, E. Tenekecioglu, L. Timmins, R. Torii, J. Wentzel, P. Serruys, Expert recommendations on the assessment of wall shear stress in human coronary arteries: existing methodologies, technical considerations, and clinical applications, Eur Heart J 40 (2019) 3421–3433. https://doi.org/10.1093/EURHEARTJ/EHZ551.

[149] J.F. LaDisa, L.E. Olson, D.A. Hettrick, D.C. Warltier, J.R. Kersten, P.S. Pagel, Axial stent strut angle influences wall shear stress after stent implantation: Analysis using 3D computational fluid dynamics models of stent foreshortening, Biomed Eng Online 4 (2005) 1–10. https://doi.org/10.1186/1475-925X-4-59.

[150] A. Sakamoto, H. Jinnouchi, S. Torii, R. Virmani, A. V. Finn, Understanding the Impact of Stent and Scaffold Material and Strut Design on Coronary Artery Thrombosis from the Basic and Clinical Points of View, Bioengineering 2018, Vol. 5, Page 71 5 (2018) 71. https://doi.org/10.3390/BIOENGINEERING5030071.

[151] M.J. Grundeken, M.A.M. Beijk, A Narrative Review of Ultrathin-strut Drug-eluting Stents: The Thinner the Better?, Heart Int 15 (2021). https://doi.org/10.17925/HI.2021.15.2.84.

[152] M.I. Papafaklis, C. V. Bourantas, P.E. Theodorakis, C.S. Katsouras, D.I. Fotiadis, L.K. Michalis, Relationship of shear stress with in-stent restenosis: Bare metal stenting and the effect of brachytherapy, Int J Cardiol 134 (2009) 25–32. https://doi.org/10.1016/J.IJCARD.2008.02.006.

[153] C. Chiastra, S. Morlacchi, D. Gallo, U. Morbiducci, R. Cárdenes, I. Larrabide, F. Migliavacca, Computational fluid dynamic simulations of image-based stented coronary bifurcation models, J R Soc Interface 10 (2013). https://doi.org/10.1098/rsif.2013.0193.

[154] F. Migliavacca, L. Petrini, M. Colombo, F. Auricchio, R. Pietrabissa, Mechanical behavior of coronary stents investigated through the finite element method, J Biomech 35 (2002) 803–811. https://doi.org/10.1016/S0021-9290(02)00033-7.

[155] D. Lim, S.K. Cho, W.P. Park, A. Kristensson, J.Y. Ko, S.T.S. Al-Hassani, H.S. Kim, Suggestion of potential stent design parameters to reduce restenosis risk driven by foreshortening or dogboning due to non-uniform balloon-stent expansion, Ann Biomed Eng 36 (2008) 1118–1129. https://doi.org/10.1007/s10439-008-9504-1.

[156] M. Azaouzi, N. Lebaal, A. Makradi, S. Belouettar, Optimization based simulation of self-expanding Nitinol stent, Mater Des 50 (2013) 917–928. https://doi.org/10.1016/J.MATDES.2013.03.012.

[157] J.F. LaDisa, L.E. Olson, R.C. Molthen, D.A. Hettrick, P.F. Pratt, M.D. Hardel, J.R. Kersten, D.C. Warltier, P.S. Pagel, Alterations in wall shear stress predict sites of neointimal hyperplasia after stent implantation in rabbit iliac arteries, Am J Physiol Heart Circ Physiol 288 (2005) 2465–2475. https://doi.org/10.1152/ajpheart.01107.2004.

[158] T. Schmidt, J.D. Abbott, Coronary stents: History, design, and construction, J Clin Med 7 (2018). https://doi.org/10.3390/jcm7060126.

[159] D. Stoeckel, C. Bonsignore, S. Duda, A survey of stent designs, Minimally Invasive Therapy and Allied Technologies 11 (2002) 137–147. https://doi.org/10.1080/136457002760273340.

[160] A. Brambilla, G. Pennati, L. Petrini, F. Berti, Stents in Congenital Heart Disease: State of the Art and Future Scenarios, Applied Sciences (Switzerland) 13 (2023). https://doi.org/10.3390/app13179692.

[161] E. Tatli, A. Tokatli, M.B. Vatan, M.T. Agac, H. Gunduz, R. Akdemir, H. Kilic, Comparison of closed-cell and hybrid-cell stent designs in Carotid artery stenting: Clinical and procedural outcomes, Postepy w Kardiologii Interwencyjnej 13 (2017) 135–141. https://doi.org/10.5114/pwki.2017.67994.

[162] E.E. de Vries, A.J.A. Meershoek, E.J. Vonken, H.M. den Ruijter, J.C. van den Berg, G.J. de Borst, K. Bijuklic, J. Schofer, L. Bonati, M. Bosiers, J. Wauters, G. de Donato, E. Chisci, C. Setacci, D. Doig, R.L. Featherstone, J. Dobson, M.M. Brown, M.K. Eskandari, J. Giri, I.Q. Grunwald, A.L. Kühn, D.K. Han, P.L. Faries, F. Hernandez-Fernandez, G. Parrilla, M. Hornung, H. Sievert, K. Kono, P. Latacz, J. Ledwoch, H. Mudra, G. Maleux, R. Nolz, T. Ohki, M. Piazza, P. Pieniazek, L. Tekieli, D. Radak, S. Tanaskovic, M. Rasiova, G. Simonte, B. Fiorucci, M.W.K. Tietke, G. Ventoruzzo, A meta-analysis of the effect of stent design on clinical and radiologic outcomes of carotid artery stenting, J Vasc Surg 69 (2019) 1952-1961.e1. https://doi.org/10.1016/J.JVS.2018.11.017.

[163] Medtronic - Cristallo Ideale - The 5F HYBRID Stent Deliverable and Secure, (2012). https://kategorizacia.mzsr.sk/Pomocky/Download/RequestAttachment/47242 (accessed May 17, 2024).

[164] F. Auricchio, M. Conti, M. Ferraro, A. Reali, Evaluation of carotid stent scaffolding through patient-specific finite element analysis, Int J Numer

Method Biomed Eng 28 (2012) 1043–1055. https://doi.org/https://doi.org/10.1002/cnm.2509.

[165] D.S. Pierce, E.B. Rosero, J.G. Modrall, B. Adams-Huet, R.J. Valentine, G.P. Clagett, C.H. Timaran, Open-cell versus closed-cell stent design differences in blood flow velocities after carotid stenting, J Vasc Surg 49 (2009) 602–606. https://doi.org/10.1016/J.JVS.2008.10.016.

[166] L. Wei, Q. Chen, Z. Li, Study on the impact of straight stents on arteries with different curvatures, J Mech Med Biol 16 (2016) 1–13. https://doi.org/10.1142/S0219519416500937.

[167] M. Conti, D. Van Loo, F. Auricchio, M. De Beule, G. De Santis, B. Verhegghe, S. Pirrelli, A. Odero, Impact of Carotid Stent Cell Design on Vessel Scaffolding: A Case Study Comparing Experimental Investigation and Numerical Simulations, Journal of Endovascular Therapy 18 (2011) 397–406. https://doi.org/10.1583/10-3338.1.

[168] sinus-XL Stent | Duomed, (2024). https://www.duomed.com/en-BE/products/sinus-xl-stent (accessed May 17, 2024).

[169] Biotronik Pulsar-18 brochure, (2024). https://www.biotronik.com/en-us/products/vi/peripheral/pulsar-18 (accessed May 17, 2024).

[170] B.Y.M. Werner, Factors Affecting Reduction in SFA Stent Fracture Rates, Endovascular Today 13 (2014) 93–95.

[171] C. Briguori, C. Sarais, P. Pagnotta, F. Liistro, M. Montorfano, A. Chieffo, F. Sgura, N. Corvaja, R. Albiero, G. Stankovic, C. Toutoutzas, E. Bonizzoni, C. Di Mario, A. Colombo, In-stent restenosis in small coronary arteries: Impact of strut thickness, J Am Coll Cardiol 40 (2002) 403–409. https://doi.org/10.1016/S0735-1097(02)01989-7.

[172] A. Kastrati, J. Mehilli, J. Dirschinger, F. Dotzer, H. Schühlen, F.-J. Neumann, M. Fleckenstein, C. Pfafferott, M. Seyfarth, A. Schömig, Intracoronary Stenting and Angiographic Results, Circulation 103 (2001) 2816–2821. https://doi.org/10.1161/01.CIR.103.23.2816.

[173] N. Foin, R.D. Lee, R. Torii, J.L. Guitierrez-Chico, A. Mattesini, S. Nijjer, S. Sen, R. Petraco, J.E. Davies, C. Di Mario, M. Joner, R. Virmani, P. Wong, Impact of stent strut design in metallic stents and biodegradable scaffolds, Int J Cardiol 177 (2014) 800–808. https://doi.org/10.1016/J.IJCARD.2014.09.143.

[174] M.M. Torki, S. Hassanajili, M.M. Jalisi, Design optimizations of PLA stent structure by FEM and investigating its function in a simulated plaque artery, Math Comput Simul 169 (2020) 103–116. https://doi.org/10.1016/J.MATCOM.2019.09.011.

[175] H.M. Hsiao, Y.P. Wang, C.Y. Ko, Y.H. Cheng, H.Y. Lee, A novel nitinol spherical occlusion device for liver cancer, Materials 9 (2016). https://doi.org/10.3390/ma9010019.

[176] C. Bonsignore, Open Stent Design, 2011. https://doi.org/10.6084/M9.FIGSHARE.95614.

[177] E. Masoumi Khalil Abad, D. Pasini, R. Cecere, Shape optimization of stress concentration-free lattice for self-expandable Nitinol stent-grafts, J Biomech 45 (2012) 1028–1035. https://doi.org/10.1016/J.JBIOMECH.2012.01.002.

[178] S. Barati, N. Fatouraee, M. Nabaei, F. Berti, L. Petrini, F. Migliavacca, J.F. Rodriguez Matas, A computational optimization study of a self-expandable transcatheter aortic valve, Comput Biol Med 139 (2021) 104942. https://doi.org/10.1016/J.COMPBIOMED.2021.104942.

[179] S. Lilburn, P.K. Norton, M. Zupkofska, L. Bedard, G.D. Harding, Atraumatic stent and method and apparatus for making the same, 2009. http://www.patentbuddy.com/Patent/8151682.

[180] S. Salamaga, H. Stępak, M. Żołyński, J. Kaczmarek, M. Błaszyk, M.G. Stanišić, Z. Krasiński, Three-Year Real-World Outcomes of Interwoven Nitinol Supera Stent Implantation in Long and Complex Femoropopliteal Lesions, J Clin Med 12 (2023). https://doi.org/10.3390/jcm12144869.

[181] A. Cremonesi, F. Castriota, G.G. Secco, S. Macdonald, M. Roffi, Carotid artery stenting: An update, Eur Heart J 36 (2015) 13–21. https://doi.org/10.1093/eurheartj/ehu446.

[182] G. Song, H.Q. Zhao, Q. Liu, Z. Fan, Bioactive Materials A review on biodegradable biliary stents : materials and future trends, Bioact Mater 17 (2022) 488–495. https://doi.org/10.1016/j.bioactmat.2022.01.017.

[183] R. Mehrabi, M.T. Andani, M. Elahinia, M. Kadkhodaei, Anisotropic behavior of superelastic NiTi shape memory alloys; an experimental investigation and constitutive modeling, Mechanics of Materials 77 (2014) 110–124. https://doi.org/10.1016/j.mechmat.2014.07.006.

[184] R. Madhkour, A. Wahl, F. Praz, B. Meier, Amplatzer patent foramen ovale occluder: safety and efficacy, Expert Rev Med Devices 16 (2019) 173–182. https://doi.org/10.1080/17434440.2019.1581060.

[185] K. Bishu, E.J. Armstrong, Supera self-expanding stents for endovascular treatment of femoropopliteal disease: A review of the clinical evidence, Vasc Health Risk Manag 11 (2015) 387–395. https://doi.org/10.2147/VHRM.S70229.

[186] K. Subramaniam, A. Ibarra, M.L. Boisen, Echocardiographic Guidance of AMPLATZER Amulet Left Atrial Appendage Occlusion Device Placement, Semin Cardiothorac Vasc Anesth 23 (2019) 248–255. https://doi.org/10.1177/1089253218758463.

[187] M.E. Seigerman, A. Nathan, S. Anwaruddin, The Lotus Valve System: an In-depth Review of the Technology, Curr Cardiol Rep 21 (2019) 1–9. https://doi.org/10.1007/s11886-019-1234-5.

[188] R. Ubachs, O. van der Sluis, S. Smith, J. Mertens, Computational modeling of braided venous stents — Effect of design features and device-tissue interaction on stent performance, J Mech Behav Biomed Mater 142 (2023) 105857. https://doi.org/10.1016/j.jmbbm.2023.105857.

[189] Q. Zheng, P. Dong, Z. Li, X. Han, C. Zhou, M. An, L. Gu, Mechanical characterizations of braided composite stents made of helical polyethylene terephthalate strips and NiTi wires, Nanotechnol Rev 8 (2019) 168–174. https://doi.org/10.1515/ntrev-2019-0016.

[190] K. Maleckis, P. Deegan, W. Poulson, C. Sievers, A. Desyatova, J. MacTaggart, A. Kamenskiy, Comparison of femoropopliteal artery stents under axial and radial compression, axial tension, bending, and torsion deformations, J Mech Behav Biomed Mater 75 (2017) 160–168. https://doi.org/10.1016/j.jmbbm.2017.07.017.

[191] G. Maleux, P. Gillardin, S. Fieuws, S. Heye, J. Vaninbroukx, K. Nackaerts, Large-bore nitinol stents for malignant superior vena cava syndrome: Factors influencing outcome, American Journal of Roentgenology 201 (2013) 667–674. https://doi.org/10.2214/AJR.12.9582.

[192] A.G. Verstandig, A.I. Bloom, T. Sasson, Y.S. Haviv, D. Rubinger, Shortening and migration of Wallstents after stenting of central venous stenoses in

hemodialysis patients, Cardiovasc Intervent Radiol 26 (2003) 58–64. https://doi.org/10.1007/s00270-002-1953-6.

[193] M.A.H. Taha, A. Busuttil, R. Bootun, B.A.H. Thabet, A.E.H. Badawy, H.A. Hassan, J. Shalhoub, A.H. Davies, Clinical outcomes and overview of dedicated venous stents for management of chronic iliocaval and femoral deep venous disease, Vascular 30 (2022) 320–330. https://doi.org/10.1177/1708538121989860.

[194] M.R. Jedwab, C.O. Clerc, A study of the geometrical and mechanical properties of a self-expanding metallic stent--theory and experiment., J Appl Biomater 4 (1993) 77–85. https://doi.org/10.1002/jab.770040111.

[195] C. Shanahan, P. Tiernan, S.A.M. Tofail, Looped ends versus open ends braided stent: A comparison of the mechanical Behavior using analytical and numerical methods, J Mech Behav Biomed Mater 75 (2017) 581–591. https://doi.org/10.1016/j.jmbbm.2017.08.025.

[196] M. Azaouzi, N. Lebaal, A. Makradi, S. Belouettar, Optimization based simulation of self-expanding Nitinol stent, Mater Des 50 (2013) 917–928. https://doi.org/10.1016/j.matdes.2013.03.012.

[197] C. Chen, J. Chen, W. Wu, Y. Shi, L. Jin, L. Petrini, L. Shen, G. Yuan, W. Ding, J. Ge, E.R. Edelman, F. Migliavacca, In vivo and in vitro evaluation of a biodegradable magnesium vascular stent designed by shape optimization strategy, Biomaterials 221 (2019). https://doi.org/10.1016/j.biomaterials.2019.119414.

[198] S. Barati, N. Fatouraee, M. Nabaei, F. Berti, L. Petrini, F. Migliavacca, J.F. Rodriguez Matas, A computational optimization study of a self-expandable transcatheter aortic valve, Comput Biol Med 139 (2021) 104942. https://doi.org/10.1016/j.compbiomed.2021.104942.

[199] S. Barati, N. Fatouraee, M. Nabaei, L. Petrini, F. Migliavacca, G. Luraghi, J.F.R. Matas, Patient-specific multi-scale design optimization of transcatheter aortic valve stents, Comput Methods Programs Biomed 221 (2022) 106912. https://doi.org/10.1016/j.cmpb.2022.106912.

[200] S. Tammareddi, G. Sun, Q. Li, Multiobjective robust optimization of coronary stents, Mater Des 90 (2016) 682–692. https://doi.org/10.1016/j.matdes.2015.10.153.

[201] J.C. Bansal, Particle swarm optimization, Studies in Computational Intelligence 779 (2019) 11–23. https://doi.org/10.1007/978-3-319-91341-4_2.

[202] C. Shanahan, Viscoelastic Braided Stent : Finite Element Analysis and Validation of Crimping Behavior, PhD Thesis, University of Limerick, IE, 2017. https://hdl.handle.net/10344/6111.

[203] A. Zaccaria, G. Pennati, L. Petrini, Analytical methods for braided stents design and comparison with FEA, J Mech Behav Biomed Mater 119 (2021) 104560. https://doi.org/10.1016/j.jmbbm.2021.104560.

[204] M. Liu, Y. Tian, J. Cheng, Y. Zhang, G. Zhao, Z. Ni, Journal of the Mechanical Behavior of Biomedical Materials Mixed-braided stent : An effective way to improve comprehensive mechanical properties of poly (L-lactic acid) self-expandable braided stent, J Mech Behav Biomed Mater 128 (2022) 105123. https://doi.org/10.1016/j.jmbbm.2022.105123.

[205] D. Stoeckel, C. Bonsignore, S. Duda, A survey of stent designs, Minimally Invasive Therapy and Allied Technologies 11 (2002) 137–147. https://doi.org/10.1080/136457002760273340.

[206] Z. Shang, J. Ma, Bending stiffness characterization of braided stent using spring-based theoretical formula, Archive of Applied Mechanics 93 (2023) 947–960. https://doi.org/10.1007/s00419-022-02307-x.

[207] N. Sulatchaneenopdon, A. Khantachawana, Effect of experimental design parameters on mechanical properties of braided stentriever made from shape memory alloy, 102 (2017) 444–448. https://doi.org/10.2991/icmmse-17.2017.74.

[208] X. Liu, H. Tao, C. Li, J. Lin, G. Guan, F. Wang, L. Wang, Effect of NiTi parameters on the mechanical properties of integrated braided stents, Textile Research Journal 93 (2023) 701–712. https://doi.org/10.1177/00405175221122608.

[209] C.G. McKenna, T.J. Vaughan, An experimental evaluation of the mechanics of bare and polymer-covered self-expanding wire braided stents, J Mech Behav Biomed Mater 103 (2020) 103549. https://doi.org/10.1016/j.jmbbm.2019.103549.

[210] H. Yu, L. Zheng, J. Qiu, J. Wang, Y. Xu, B. Fan, R. Li, J. Liu, C. Wang, Y. Fan, Mechanical property analysis and design parameter optimization of a novel nitinol nasal stent based on numerical simulation, Front Bioeng Biotechnol 10 (2022) 1–14. https://doi.org/10.3389/fbioe.2022.1064605.

[211] M. De Beule, M. Conti, P. Mortier, P. Verdonck, P. Segers, F. Auricchio, B. Verhegghe, Finite element analysis of self expanding braided wire stents, Second African Conference on Computational Mechanics –AfriCOMP11 (2011).

[212] A.R. Pelton, B.T. Berg, P. Saffari, A.P. Stebner, A.N. Bucsek, Pre-strain and Mean Strain Effects on the Fatigue Behavior of Superelastic Nitinol Medical Devices, Shape Memory and Superelasticity 8 (2022) 64–84. https://doi.org/10.1007/s40830-022-00377-y.

[213] A.R. Pelton, V. Schroeder, M.R. Mitchell, X. Gong, M. Barney, S.W. Robertson, Fatigue and durability of Nitinol stents, 1 (2008) 153–164. https://doi.org/10.1016/j.jmbbm.2007.08.001.

[214] M.H. (Martin H. Sadd, Elasticity : theory, applications, and numerics, Elsevier, 2021.

[215] A.G. Demir, B. Previtali, Lasers in the manufacturing of cardiovascular metallic stents: Subtractive and additive processes with a digital tool, in: Procedia Comput Sci, Elsevier B.V., 2022: pp. 604–613. https://doi.org/10.1016/j.procs.2022.12.256.

[216] L. Yan, S.L. Soh, N. Wang, Q. Ma, W.F. Lu, S.T. Dheen, A.S. Kumar, J.Y.H. Fuh, Evaluation and characterization of nitinol stents produced by selective laser melting with various process parameters, Progress in Additive Manufacturing 7 (2022) 1141–1153. https://doi.org/10.1007/s40964-022-00289-4.

[217] V. Finazzi, F. Berti, L. Petrini, B. Previtali, A.G. Demir, Additive manufacturing and post-processing of superelastic NiTi micro struts as building blocks for cardiovascular stents, Addit Manuf 70 (2023) 103561. https://doi.org/10.1016/J.ADDMA.2023.103561.

[218] StarCut Tube - CNC Laser Cutting Machine | Coherent, (2024). https://www.coherent.com/machines-systems/laser-cutting-drilling/starcut-tube (accessed May 17, 2024).

[219] Innovasc, Solaris-Self-expanding-peripharial solution, n.d. https://innovasc.es/en/peripheral-solutions/ (accessed December 13, 2024).

[220] F. Auricchio"’", R.L. Taylorb, Computer methods In applied mechanics and englnserlng Shape-memory alloys: modelling and numerical simulations of the finite-strain superelastic behavior, 1997.

[221] M.S. Cabrera, C.W.J. Oomens, F.P.T. Baaijens, Understanding the requirements of self-expandable stents for heart valve replacement: Radial force, hoop force and equilibrium, J Mech Behav Biomed Mater 68 (2017) 252–264. https://doi.org/10.1016/j.jmbbm.2017.02.006.

[222] Y. Li, Y. Shi, Y. Lu, X. Li, J. Zhou, A.A. Zadpoor, L. Wang, Additive manufacturing of vascular stents, Acta Biomater 167 (2023) 16–37. https://doi.org/10.1016/J.ACTBIO.2023.06.014.

[223] K. Safaei, M. Nematollahi, P. Bayati, H. Dabbaghi, O. Benafan, M. Elahinia, Torsional behavior and microstructure characterization of additively manufactured NiTi shape memory alloy tubes, Eng Struct 226 (2021) 111383. https://doi.org/10.1016/j.engstruct.2020.111383.

[224] 3D Printed Nitinol Opens New Possibilities for Arterial Stents | Additive Manufacturing, (2020). https://www.additivemanufacturing.media/articles/3d-printed-nitinol-opens-new-possibilities-for-arterial-stents (accessed May 2, 2024).

[225] A.F.C.M.F.B.B.D.M.G.M. M. Gragnanini, Studio sperimentale ed analitico delle condizioni di stampa di una lega NiTi ottenuta mediante tecnica SLM, in: Convegno nazionale AIM , Napoli, 2024. https://doi.org/10.3384/lic.diva-160888.

[226] H. Meier, C. Haberland, J. Frenzel, Structural and functional properties of NiTi shape memory alloys produced by Selective Laser Melting, in: 2011. https://doi.org/https://doi.org/10.1201/B11341-47.

[227] V. Finazzi, F. Berti, R.J. Guillory, L. Petrini, B. Previtali, A.G. Demir, Patient-specific cardiovascular superelastic NiTi stents produced by laser powder bed fusion, in: Procedia CIRP, Elsevier B.V., 2022: pp. 244–248. https://doi.org/10.1016/j.procir.2022.06.044.

[228] O.M. McGee, S. Geraghty, C. Hughes, P. Jamshidi, D.P. Kenny, M.M. Attallah, C. Lally, An investigation into patient-specific 3D printed titanium stents and the use of etching to overcome Selective Laser Melting design constraints, J Mech Behav Biomed Mater 134 (2022) 105388. https://doi.org/10.1016/J.JMBBM.2022.105388.

[229] P. Jamshidi, C. Panwisawas, E. Langi, S.C. Cox, J. Feng, L. Zhao, M.M. Attallah, Development, characterisation, and modelling of processability of nitinol stents using laser powder bed fusion, J Alloys Compd 909 (2022) 164681. https://doi.org/10.1016/J.JALLCOM.2022.164681.

[230] M.A. Obeidi, A.R. Al-Hamaoy, A. Cholkar, N. Agarwal, D. Brabazon, Comparing the surface characteristics of additively manufactured nitinol parts polished by femto-second and CO2 laser, Applied Surface Science Advances (2024) 100637. https://doi.org/https://doi.org/10.1016/j.apsadv.2024.100637.

[231] J. Dong, M. Pacella, Y. Liu, L. Zhao, Surface engineering and the application of laser-based processes to stents - A review of the latest development, Bioact Mater 10 (2022) 159–184. https://doi.org/10.1016/J.BIOACTMAT.2021.08.023.

[232] A. Lantada, C. Vega, R. Martínez, M. Rendón, M. Li, Ó. Contreras-Almengor, J. Ordoño, W. Solórzano-Requejo, M. Vasic, J. Munoz-Guijosa, J. Molina-Aldareguia, Additive Manufacturing of Nitinol for Smart Personalized

Medical Devices: Current Capabilities and Challenges, in: Scitepress, 2024: pp. 123–134. https://doi.org/10.5220/0012363900003657.
[233] A.M. Sousa, A.M. Amaro, A.P. Piedade, 3D Printing of Polymeric Bioresorbable Stents: A Strategy to Improve Both Cellular Compatibility and Mechanical Properties, Polymers (Basel) 2022 (2022) 1099. https://doi.org/10.3390/polym.
[234] M. Somireddy, A. Czekanski, Anisotropic material behavior of 3D printed composite structures – Material extrusion additive manufacturing, Mater Des 195 (2020) 108953. https://doi.org/10.1016/J.MATDES.2020.108953.
[235] S. Dadbakhsh, B. Vrancken, J.P. Kruth, J. Luyten, J. Van Humbeeck, Texture and anisotropy in selective laser melting of NiTi alloy, Materials Science and Engineering: A 650 (2016) 225–232. https://doi.org/10.1016/J.MSEA.2015.10.032.
[236] V. Finazzi, A.G. Demir, C.A. Biffi, C. Chiastra, F. Migliavacca, L. Petrini, B. Previtali, Design Rules for Producing Cardiovascular Stents by Selective Laser Melting: Geometrical Constraints and Opportunities, Procedia Structural Integrity 15 (2019) 16–23. https://doi.org/10.1016/J.PROSTR.2019.07.004.
[237] A. Guerra, A. Roca, J. de Ciurana, A novel 3D additive manufacturing machine to biodegradable stents, Procedia Manuf 13 (2017) 718–723. https://doi.org/10.1016/J.PROMFG.2017.09.118.
[238] P.P. Selvakumar, M.S. Rafuse, R. Johnson, W. Tan, Applying Principles of Regenerative Medicine to Vascular Stent Development, Front Bioeng Biotechnol 10 (2022). https://www.frontiersin.org/articles/10.3389/fbioe.2022.826807.
[239] S. Choudhury, S. Asthana, S. Homer-Vanniasinkam, K. Chatterjee, Emerging trends in biliary stents: a materials and manufacturing perspective, Biomater Sci 10 (2022) 3716–3729. https://doi.org/10.1039/D2BM00234E.
[240] K. Nakamura, J.H. Keating, E.R. Edelman, Pathology of Endovascular Stents, Interv Cardiol Clin 5 (2016) 391–403. https://doi.org/10.1016/J.ICCL.2016.02.006.
[241] B. Kumar, R. Rakesh Ram, N. Dahiya, A.A. Gawalkar, Real-World Clinical Outcomes of Indigenous Biodegradable Polymer Drug-Eluting Stents, Cureus 13 (2021). https://doi.org/10.7759/cureus.17886.
[242] T.R. Yeazel, M.L. Becker, Advancing Toward 3D Printing of Bioresorbable Shape Memory Polymer Stents, Biomacromolecules 21 (2020) 3957–3965. https://doi.org/10.1021/acs.biomac.0c01082.
[243] J. Lai, C. Wang, M. Wang, 3D printing in biomedical engineering: Processes, materials, and applications, Appl Phys Rev 8 (2021) 021322. https://doi.org/10.1063/5.0024177.
[244] M. Ullah, A. Bibi, A. Wahab, S. Hamayun, M.U. Rehman, S.U. Khan, U.A. Awan, N. ul ain Riaz, M. Naeem, S. Saeed, T. Hussain, Shaping the Future of Cardiovascular Disease by 3D Printing Applications in Stent Technology and its Clinical Outcomes, Curr Probl Cardiol 49 (2024) 102039. https://doi.org/10.1016/J.CPCARDIOL.2023.102039.
[245] M.H. Mobarak, M.A. Islam, N. Hossain, M.Z. Al Mahmud, M.T. Rayhan, N.J. Nishi, M.A. Chowdhury, Recent advances of additive manufacturing in implant fabrication – A review, Applied Surface Science Advances 18 (2023) 100462. https://doi.org/10.1016/J.APSADV.2023.100462.
[246] F. Garcia-Villen, F. López-Zárraga, C. Viseras, S. Ruiz-Alonso, F. Al-Hakim, I. Diez-Aldama, L. Saenz-del-Burgo, D. Scaini, J.L. Pedraz, Three-

dimensional printing as a cutting-edge, versatile and personalizable vascular stent manufacturing procedure: Toward tailor-made medical devices, Int J Bioprint 9 (2022) 219–255. https://doi.org/10.18063/IJB.V9I2.664.

[247] C. Aravena, T.R. Gildea, Patient-specific airway stent using three-dimensional printing: a review, Ann Transl Med 11 (2023) 360–360. https://doi.org/10.21037/atm-22-2878.

[248] F. Tang, C. Hu, S. Huang, W. Long, Q. Wang, G. Xu, S. Liu, B. Wang, L. Zhang, L. Li, An Innovative Customized Stent Graft Manufacture System Assisted by Three-Dimensional Printing Technology, Ann Thorac Surg 112 (2021) 308–314. https://doi.org/10.1016/J.ATHORACSUR.2020.07.013.

[249] M.-K. HONG, J.-M. SHIM, Y.-J. YOUN, K.-H. LEE, J.-S. KIM, Y.-G. KO, S.-H. LEE, D. CHOI, J. YOON, Y. JANG, A New Stent Design for the Treatment of True Bifurcation Lesions: H-Side Branch Stents, J Interv Cardiol 23 (2010) 54–59. https://doi.org/https://doi.org/10.1111/j.1540-8183.2009.00519.x.

[250] H. Xue, Z. Luo, T. Brown, S. Beier, Design of Self-Expanding Auxetic Stents Using Topology Optimization, Front Bioeng Biotechnol 8 (2020). https://www.frontiersin.org/articles/10.3389/fbioe.2020.00736.

[251] M.N. Ali, J.J.C. Busfield, I.U. Rehman, Auxetic oesophageal stents: structure and mechanical properties, J Mater Sci Mater Med 25 (2014) 527–553. https://doi.org/10.1007/s10856-013-5067-2.

[252] X.L. Ruan, J.J. Li, X.K. Song, H.J. Zhou, W.X. Yuan, W.W. Wu, R. Xia, Mechanical Design of Antichiral-Reentrant Hybrid Intravascular Stent, Int J Appl Mech 10 (2018) 1850105. https://doi.org/10.1142/S1758825118501053.

[253] G. Alaimo, F. Auricchio, M. Conti, M. Zingales, Multi-objective optimization of nitinol stent design, Med Eng Phys 47 (2017) 13–24. https://doi.org/10.1016/J.MEDENGPHY.2017.06.026.

[254] D. Carbonaro, F. Mezzadri, N. Ferro, G. De Nisco, A.L. Audenino, D. Gallo, C. Chiastra, U. Morbiducci, S. Perotto, Design of innovative self-expandable femoral stents using inverse homogenization topology optimization, Comput Methods Appl Mech Eng 416 (2023) 116288. https://doi.org/10.1016/J.CMA.2023.116288.

Appendices

Appendix A

OPEN ACCESS
IOP Publishing
Smart Materials and Structures
Smart Mater. Struct. 32 (2023) 035027 (14pp)
https://doi.org/10.1088/1361-665X/acb749

Development and prototyping of SMA-metamaterial biaxial composite actuators

Luke Mizzi*, **Seyedeh Farzaneh Hoseini, Marco Formighieri and Andrea Spaggiari**

Dipartimento di Scienze e Metodi dell'Ingegneria, Università di Modena e Reggio Emilia, Reggio Emilia, Italy

E-mail: luke.mizzi@unimore.it

Received 7 December 2022, revised 18 January 2023
Accepted for publication 30 January 2023
Published 10 February 2023

Abstract

Shape memory alloys (SMA) are excellent candidates for implementation in actuator systems due to their ability to recover their original shape after high-strain loading through a thermally-induced phase transition. In this work, we propose and develop a novel SMA-metamaterial actuator which is capable of exhibiting a reversible, global elongation in multiple directions induced by the unidirectional contraction upon heating of a single SMA component. This actuator consists of (a) an SMA component, (b) a bias component and (c) the metamaterial geometry, with each component having a distinct function: (a) actuation activation, (b) reversibility of actuation upon deactivation and (c) amplifying and re-directing the uni-directional SMA actuation globally throughout the actuator, respectively. A prototype actuator was designed and tested in various configurations over multiple activation/deactivation cycles in order to demonstrate the functionality and reusability of this system. Furthermore, a theoretical model which predicts the actuation stroke of the system on the basis of the material properties of the SMA and bias components as well as the geometry of the metamaterial system was developed and validated. The findings of this work demonstrate the considerable potential of SMA-metamaterial actuators for implementation in systems requiring a multi-axial actuation output.

Keywords: shape memory alloys, mechanical metamaterials, actuators, auxetic, composites

SI-2023ECCOMAS

Journal of
Intelligent Material
Systems and Structures

Journal of Intelligent Material Systems and Structures
1–11

DOI: 10.1177/1045389X241293851
journals.sagepub.com/home/jim
Sage

Multi objective design optimization of self-expandable nitinol braided stents

Seyedeh Farzaneh Hoseini and Andrea Spaggiari

Abstract

Cardiovascular stents are indispensable medical devices used to treat vessel-related issues such as atherosclerotic plaque. In the past, stents were mainly made of materials like stainless steel or cobalt-chromium alloy. However, over the last two decades, research has focused on the use of Nitinol (NiTi) due to its superior properties such as super-elasticity, biocompatibility, and strength. The aim of this paper is to optimize the design of an open-ended braided stent, subjected to radial compression, with enhanced performance. The optimization process uses Multi-Objective Particle Swarm Optimization (MOPSO), which explores three design variables, namely wire diameter, number of coils, and braided angle, to determine the optimal shape that maximizes radial pressure stiffness and radial force exerted on the vessel walls while minimizing foreshortening. The analytical model developed is compared against literature findings, and the optimization results are implemented in a finite element analysis solver and compared with existing references. The results show that the optimized design using MOPSO enhances the stent's average radial force and radial pressure stiffness by 28% and 40% respectively, while decreasing foreshortening by nearly 5%. The results demonstrate the feasibility of MOPSO for optimizing braided NiTi stents and the use of FEM for validating optimized designs.

Keywords

Self-expanding braided stent, NiTi, multi-objective optimization, MOPSO algorithm, finite element method

Materials Today Communications 41 (2024) 111042

Contents lists available at ScienceDirect

Materials Today Communications

journal homepage: www.elsevier.com/locate/mtcomm

Self-expanding Nitinol stents for endovascular peripheral applications: A review

Farzaneh Hoseini[a], Alberto Bellelli[a], Luke Mizzi[a], Felice Pecoraro[b,c], Andrea Spaggiari[a,*]

[a] *Department of Science and Methods for Engineering, University of Modena and Reggio Emilia, Reggio Emilia, Italy*
[b] *Vascular Surgery Unit - AOUP Policlinico 'P. Giaccone', Palermo, Italy*
[c] *Department of Precision Medicine in Medical, Surgical, and Critical Care (Me. Pre.C.C.) – University of Palermo, Italy*

ARTICLE INFO

Keywords:
Peripheral stent
Nitinol
Self-expanding stent
Arterial and venous stent
Biomedical engineering

ABSTRACT

Peripheral arterial diseases affect a significant portion of the global population, fostering research to find innovative and effective solutions to improve people's life. A primary focus for researchers and manufacturers is the continuous improvement of the most important, non-surgical treatment for this pathology, the endovascular stent. This device is the main feature enabling a lifesaving technique: the percutaneous vascular interventions. Stents are vital for restoring blood flow and enhancing long-term vessel patency, they are available in various materials, shapes and typologies. Recent advancements in stent design, particularly through additive manufacturing, create new opportunities for optimizing the device performance and possibly opening new areas of intervention. This review provides a detailed quantitative analysis on the most widely used category of devices: self-expanding stents made of Nitinol, a nickel-titanium alloy that shows a superelastic behavior. A set of figures of merit related to stent design are described and analyzed, with a focus on the influence of geometry on mechanical performance. Additionally, a comprehensive comparative analysis of the commercial stents evaluates the geometry and performance of many commercial solutions, including both arterial and venous types. This analysis offers quantitative tools to assist surgeons and designers in selecting the most important features of a stent with respect to its main application. To conclude this work, an overview of future manufacturing possibilities is provided mainly focusing on the additive manufacturing technology. The freedom of shape given by this method opens up new paths in terms of global shapes, strut geometry and sizes, revealing new avenues which point strongly towards ad-hoc and specifically patient-customized stent design.